THE UNIVERSITY OF QUEENSLAND

AUSTRALIA

A study of rock cutting with point attack picks

Wen Shao

Bachelor of Engineering

A thesis submitted for the degree of Doctor of Philosophy at

The University of Queensland in 2016

School of Mechanical and Mining Engineering

Abstract

Hard rock mining is currently carried out by drill-and-blast. With the increasing demand for automated, selective and remote mining, the industry hopes to replace conventional drill-and-blast with mechanical excavation. Modern mining machines have sufficient power for cutting hard rocks. The 'bottleneck' which limits the use of mechanical excavation for hard rock mining is the cutting tool wear. Rock cutting tools usually use tungsten carbide (WC) tipped picks. The WC tipped picks are effective and adequate for cutting relatively soft rocks, but unsuitable for hard rocks. To address this issue, CSIRO has developed Super Material Abrasive Resistant Tool (SMART*CUT), aiming at providing an effective cutting tool for hard rock mining. The key feature of the SMART*CUT technology is replacing the conventional WC with thermally stable diamond composite (TSDC) as the cutting tip of the pick. The main advantages of the TSDC tipped picks include (a) good thermal stability, (b) high wear resistance and (c) the ability to mine relatively hard deposits in comparison with the WC tipped picks. The disadvantage of the TSDC tipped picks is their low fracture toughness. To optimise the application of the TSDC tipped picks, this work aimed to improve the understanding of the rock cutting process and mechanisms, in particular to gain a better insight into the interaction between tools and rocks through systematic experimental and numerical studies. The rock cutting processes with the TSDC and WC tipped point attack picks were comprehensively investigated in terms of cutting force, specific energy, tool tip temperature and cutting chips.

A study of rock cutting was systematically carried out using the Taguchi method to determine the effects of the cutting parameters on the performance of the TSDC tipped picks. The signal-to-noise (S/N) ratios and the analysis of variance (ANOVA) were applied to investigate the effects of the depth of cut, attack angle, spacing and cutting speed on the mean cutting, normal and bending forces involved in the rock cutting process. The statistical significance of process factors was determined and the optimum parametric combinations were successfully identified. Furthermore, the multiple linear regression (MLR) and artificial neural network (ANN) techniques were adopted to develop the empirical models for predicting the mean cutting and normal forces with the TSDC tipped picks. The established empirical force models showed good predictive capabilities with acceptable accuracy. The ANN models offered better accuracy and less deviation than the MLR models.

The pick cutting temperature involved in rock cutting was measured using thermal infrared imaging and embedded thermocouple techniques. The temperature distribution in the cutting area was acquired by using a thermal infrared camera with high speed imaging rates. The results showed that

the TSDC tipped picks generated much lower thermal energy and much fewer sparks than the WC tipped picks. The temperature at the pick tip in the contact area with the rock was measured using a special thermocouple configuration. It was found that the pick tip temperature increased significantly with the increased depth of cut and cutting speed. The effect of spacing on the pick tip temperature was smaller than that of the depth of cut and cutting speed, particularly when the spacing was greater than that required to change from unrelieved to relieved cutting.

A series of rock cutting tests was also conducted to investigate the effects of cutting parameters on the coarseness index for the TSDC tipped picks. It was found that depth of cut, cutting speed and spacing had relatively great contributions to the coarseness index. These key parameters were then chosen to examine their effects on the rock chip size distribution and specific energy. The results showed that the dust proportion decreased with the increased depth of cut and decreased cutting speed, while the fraction of large chips increased with the increased depth of cut and decreased cutting speed. The effect of the spacing on the proportion of dust and the formation of large chips was insignificant. The specific energy increased with the increased cutting speed and spacing, while it decreased and then approached a saturated value with increasing depth of cut.

Three dimensional numerical models were developed to simulate the rock cutting process using an explicit finite element code LS-DYNA. Using these numerical models, the cutting forces and specific energies under different cutting conditions were obtained and then compared with the results obtained experimentally and analytically. The simulated forces and specific energies were in good agreement with the experimental data, which validated the numerical models. The simulated cutting forces were, in general, consistent with those predicted by the analytical models of Evans and Goktan. However, discrepancy existed because the Evans's model is independent of attack angle and cutting speed, and Goktan's model does not include the effect of cutting speed.

Declaration by author

This thesis is composed of my original work, and contains no material previously published or written by another person except where due reference has been made in the text. I have clearly stated the contribution by others to jointly-authored works that I have included in my thesis.

I have clearly stated the contribution of others to my thesis as a whole, including statistical assistance, survey design, data analysis, significant technical procedures, professional editorial advice, and any other original research work used or reported in my thesis. The content of my thesis is the result of work I have carried out since the commencement of my research higher degree candidature and does not include a substantial part of work that has been submitted to qualify for the award of any other degree or diploma in any university or other tertiary institution. I have clearly stated which parts of my thesis, if any, have been submitted to qualify for another award.

I acknowledge that an electronic copy of my thesis must be lodged with the University Library and, subject to the policy and procedures of The University of Queensland, the thesis be made available for research and study in accordance with the Copyright Act 1968 unless a period of embargo has been approved by the Dean of the Graduate School.

I acknowledge that copyright of all material contained in my thesis resides with the copyright holder(s) of that material. Where appropriate I have obtained copyright permission from the copyright holder to reproduce material in this thesis.

Publications during candidature

1. **Shao, W**., Li, X.S., Sun, Y., Huang, H., 2014. Laboratory Comparison of SMART*CUT Picks With WC Picks. Advanced Materials Research. 1017, 323-328.

2. **Shao, W**., Li, X.S., Sun, Y., Huang, H., 2014. Linear Rock Cutting with SMART* CUT Picks. Applied Mechanics and Materials. 477, 1378-1384.

3. Sun, Y., Li, X.S., **Shao, W**., 2012. Influence of Cutting Parameters and Interactions on the Depth of Cut in Continuous Mining Operation. Advanced Materials Reaearch. 538-541, 1422-1428.

Publications included in this thesis

1. **Shao, W**., Li, X.S., Sun, Y., Huang, H., 2014. Laboratory Comparison of SMART*CUT Picks With WC Picks. Advanced Materials Research. 1017, 323-328. – incorporated as part of Chapter 5.

Contributor	Statement of contribution
Author Shao, W. (Candidate)	Conception and design (80%) Experiments and analysis (75%) Wrote the paper (70%)
Author Li, X.S.	Conception and design (20%) Experiments and analysis (15%) Wrote and edited paper (10%)
Author Sun, Y.	Experiments and analysis (10%) Reviewed the paper
Author Huang, H.	Wrote and edited paper (20%)

Contributions by others to the thesis

No contributions by others.

Statement of parts of the thesis submitted to qualify for the award of another degree

None

Acknowledgements

Having struggled and been perseverant. The long and laborious journey would not be finalised without the assistance of a number of people.

First and foremost I would like to express my sincere gratitude to Prof. Han Huang, my principle supervisor, and Dr. Xingsheng Li, my associate supervisor for their patience, invaluable guidance, useful insights, helpful advice and continuous support throughout the doctoral study. Great appreciation must also go to Dr. Yong Sun and Dr. Jim Boland for their constructive suggestions and enlightening discussions.

I would also like to thank A/Prof. Kazuhiro Nogita and Dr. Zhiqiang Guan, my milestone review committee members, for their informative advice and supports about the scope and direction of my research.

Technical support from Peter Clark and Craig Harbers of CSIRO (the Commonwealth Scientific and Industrial Research Organisation) Energy Flagship are gratefully acknowledged.

Acknowledge is also extended to the colleagues and friends at the Energy Flagship Division of CSIRO for the encouragement and support during my stay there. I specially mention Mrs Deirdre Tribe, Dr. Marc Elmouttie, Mr. Greg Krahenbuhl, Mr. George Poropat, Mrs Cindy Ballard, Mr. Yi Duan, Dr. Yonggang Jin, Ms. Linda Dixon, Dr. Qingdong Qu, Dr. Johnny Qin, Dr. Rao Balusu, Dr. Hua Guo, Dr. Shi Su, Dr. Yucang Wang and Mr. Xin Yu. I am grateful for the help from the co-workers in Prof. Han Huang's group, and also the assistance from the School administrative staffs.

I would like to express appreciation to the China Scholarship Council, the University of Queensland and CSIRO for the financial support of this project.

Deepest gratitude is expressed to my parents and girlfriend for their selfless love, understanding and support.

Keywords

Rock cutting, point attack pick, SMART*CUT pick, TSDC, WC pick, cutting forces, force prediction, temperature measurement, rock chips, specific energy, finite element modelling.

Australian and New Zealand Standard Research Classifications (ANZSRC)

ANZSRC code: 091399, Mechanical Engineering not elsewhere classified, 40%
ANZSRC code: 091307, Numerical modelling and Mechanical Characterisation, 25%
ANZSRC code: 091405, Mining Engineering, 35%

Fields of Research (FoR) Classification

FoR code: 0913, Mechanical Engineering, 65%
FoR code: 0914, Resources Engineering and Extractive Metallurgy, 35%

Table of Contents

List of Figures

List of Tables

List of Abbreviations

CSIRO	Commonwealth Scientific and Industrial Research Organization
WC	Tungsten carbide
SMART*CUT	Super Material Abrasive Resistant Tool
TSDC	Thermally Stable Diamond Composite
UCS	Uniaxial compressive strength
BTS	Brazilian tensile strength
SE	Specific energy
TBM	Tunnel boring machine
MRDE	Mining and Research and Development Establishment of National Coal Board
EMI	Earth Mechanics Institute
CSM	Colorado School of Mines
HPWJA	High pressure water jet assistance
2D	Two dimensional
3D	Three dimensional
FEM	Finite element method
FDM	Finite difference method
DEM	Discrete element method
BEM	Boundary element method
DDM	Displacement discontinuity method
FLAC	Fast Lagrangian analysis of continuum
PFC	Particle flow codes
PDC	Polycrystalline diamond compact
EDM	Electric Discharge Machine
CI	Coarseness Index
SiC	Silicon carbide
DOC	Depth of cut
OA	Orthogonal arrays
MCF	Mean cutting force
MNF	Mean normal force
S/N	Signal-to-noise
ANOVA	Analysis of variance

PCR	Percent contribution ratio
MLR	Multiple linear regression
ANN	Artificial neural network
VIF	Variance inflation factor
PVD	Physically vapor deposited
ICR	Instantaneous cutting rate
CSCM	Continuous Surface Cap Model

List of Symbols

A, B, C, D_1	Softening parameters
d	Depth of cut
$d_{\max}$	Maximum damage allowed to accumulate
D	Diameter of the core sample
E	Young's modulus of the rock
E_1	Secant elasticity modulus of the rock
F_b	Bending force
F_c, F_n, F_s	Cutting, normal and sideway forces
F_c'	Hardening cap surface
Fc	Peak cutting force
F_f	Shear failure surface
G_s	Strain energy release rate of the rock
$\bar{H}$	Corresponding "hardness" through the indentation tests
I_1	First invariant of the stress tensor
J_2, J_3	Second and third invariant of the stress tensor
k	Geometric factor of the pick independent of rock properties
K_{IC}	Toughness of the rock
l	Cutting length
L	Length of the core sample
m	Mass of chips
MS_d, MS_e	Mean squared deviation due to each design parameters and errors
MS	Mean square deviation
n	Stress distribution factor
$P_{\max}$	Maximum load
s	Spacing
SS_d, SS_e	Sum of squared deviations due to each design parameters and errors (in Chapter 4)
SS_T	Total sum of squared deviations

S_s	Shear strength
S_y^2	Variation of the observed data
v	Cutting speed
W	Chisel pick width
α	Rake angle of tool
$\alpha_1, \lambda, \beta_1, \theta_1$	Shear surface term (in Chapter 7)
δ	Friction angle between tool and rock
$\varepsilon_{\max}$	Maximum principal strain
$\eta_{LTB}, \eta_{NTB}, \eta_{STB}$	S/N ratios for the large-the-better, nominal-the-best, and smaller-the-better
θ	Half tip angle of the point attack pick
θ_a	Attack angle
θ_s	Shear angle between shear plane and cutting direction
κ	Cap hardening parameter
μ_i	Mean response for ith experiment
μ_m	Overall mean of the response
ρ	Density of rock
σ_c	Uniaxial compressive strength of the rock
$\sigma_{ij}, \varepsilon_{ij}$	Stress and strain tensors
σ_n	Normal stress at the failure plane
σ_t	Tensile strength of the coal/rock
τ_c, τ_t	Strain energy terms
τ_s	Shear stress at the failure plane
φ	Internal friction angle
ω	Geometric factor dependent on the pick geometry
$\Re$	Rubin scale function

1

Introduction

1.1 Background

In the mining industry there is a growing demand for rapid and often large scale excavation to access and develop new ore bodies. This has led to extensive research leading to the increased application of mechanical excavation machines in the past few decades. These machines offer many advantages such as high productivity, better reliability, ease of automation as well as being environmentally friendly. Additionally they allow for continuous and selective mining, controllability of the chip sizes and safer operations in comparison with the conventional drill & blast technique [1-5]. Open pit and underground coal mining are now carried out by mechanical excavation machinery such as surface miners, longwall shearers (Figure 1.1) and continuous miners (Figure 1.2). These mechanical excavation machines usually cut rock/coal with an array of picks installed at specific intervals, spacing and attack angles on a rotating drum or cutterhead [2].

Figure 1.1 Longwall shearer

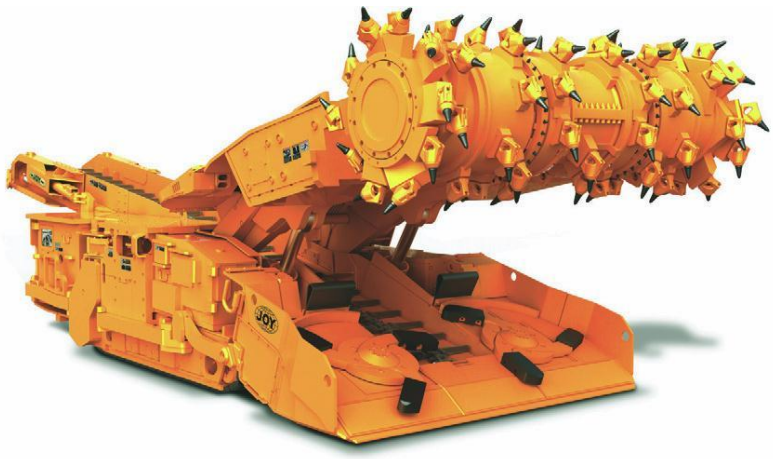

Figure 1.2 Continuous miner

There are two main categories of drag bits employed on underground mining machines (Figure 1.3), radial and point attack/conical picks. Radial picks, also termed wedge or chisel picks are designed with the axis of pick shank normally parallel to the radial line of cutterhead or drum. It is well established that new radial picks are the most efficient cutting tools. However, they are very susceptible to wear when cutting high strength and abrasive rocks. While point attack picks with conical shape inserts are more durable and have a self-sharpening property due to their free rotation in tool holders, and hence wear evenly which prolongs tool life. But their free rotation in the tool holders is not always the case due to operational and design reasons [1, 5-7].

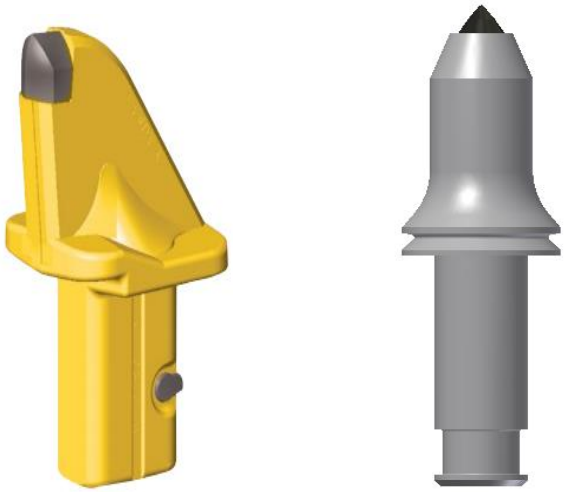

Figure 1.3 Radial (left) and point-attack (right) picks

Underground coal mining has shifted away from cyclic to continuous mining, achieving high rates of excavation and high productivity through the employment of mechanised excavation methods. Underground no-explosive hard rock mining is, however, limited by machines and cutting tool technology. It is understood that cutter cost is one of the most important factors against the mechanical machinery such as roadheader, continuous miners and longwall shearers, from becoming a commercial reality in hard rock mines. Therefore, cutting tool technology and its development will determine the future of hard rock mechanical excavation. Any extension of cutter life would have significant impact upon the economical feasibility of such machines.

1.2 Significance and motivation

Over the past several decades, drag tools employed on mechanical machinery have dominantly been implemented by using cemented tungsten carbides (WC) tipped picks. They have proven effective and adequate in most coal measures and soft rocks, but are less successful and suitable as the rock

hardness and especially abrasiveness increase [8]. It can be seen from Figure 1.4 that the performance of a surface miner drops dramatically as rock uniaxial compressive strength (UCS) increases. The upper UCS limit of this surface miner equipped with WC tipped picks is 80 MPa.

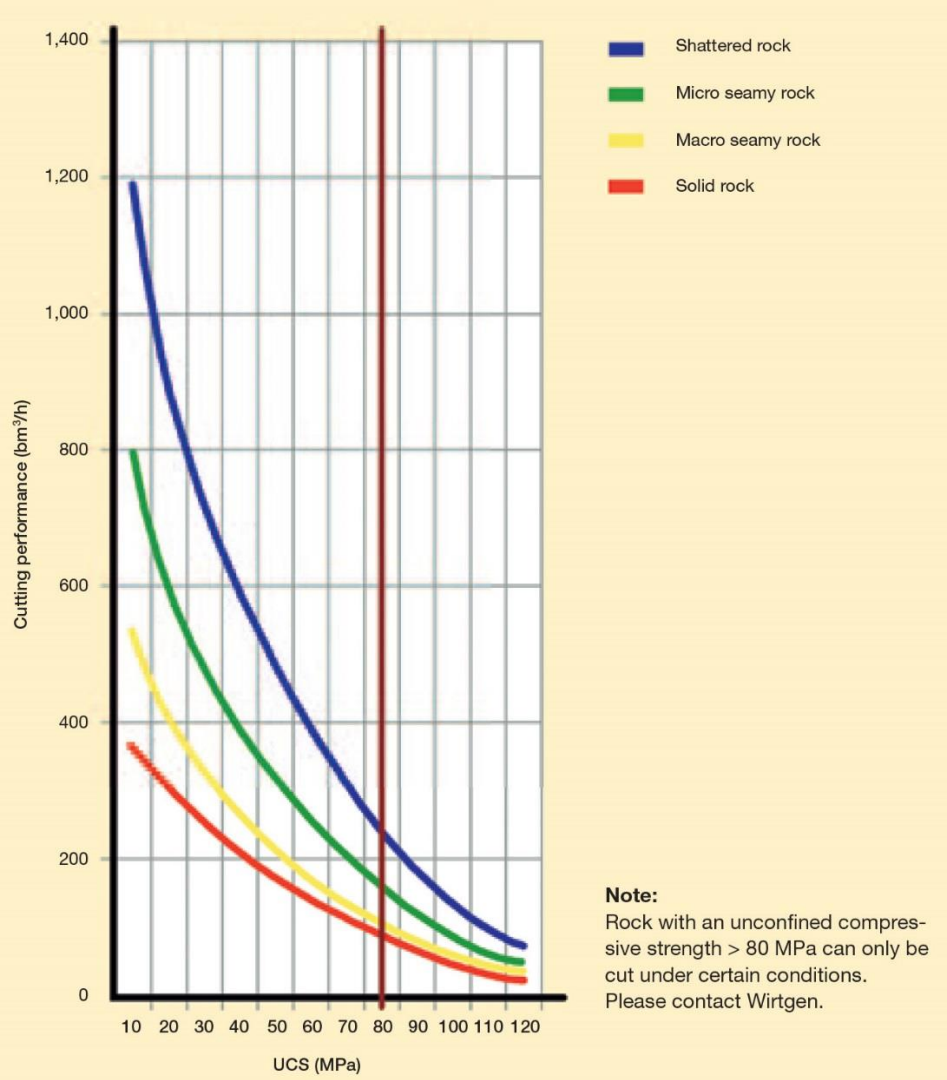

Figure 1.4 Performance chart for the surface miner 2005SM [9]

Many attempts have been made, so far unsuccessfully, to develop mechanical excavation systems for hard rock mines. The real "bottleneck" is the severe abrasive wear of the cutting tools which will result in short life of cutting tools, thereby increasing the machine downtime and cutter cost. Furthermore, respirable dust, which is a thread to miners' life, arises from the inefficient cutting when using worn picks [10, 11].

Another hazardous situation, caused by using worn picks in high strength rock cutting processes is the considerable frictional heat generated between WC tipped picks and rock. A number of mining disasters have been caused by frictional ignition in Australia and overseas. Most cases of frictional

ignition in Australia were caused by worn cutter picks striking a high silica material (conglomerate roof, sandstone roof or material associated with geological structures) in gassy conditions.

To address these issues, Super Material Abrasive Resistant Tool (SMART*CUT) technology has been developed by CSIRO (Commonwealth Scientific and Industrial Research Organisation) which employs thermally stable diamond composite (TSDC) rather than WC as a cutting tip in the tool and uses CSIRO's worldwide patented bonding technology to attach the TSDC tip to the steel tool body [12-14]. A comparison of wear characteristics of solid, moulded TSDC and WC cutting elements has been investigated previously [15-17]. A series of abrasive wear tests have been undertaken on a range of TSDC and WC cutting elements samples using a vitrified bonded alumina grinding wheel of standard manufacture in CSIRO [16]. It was identified that the wear rate of TSDC elements was significantly less than that of cemented WC [16].

Although the wear resistance of TSDC is considerably greater than that of WC, its fracture toughness is less than that of WC. Nevertheless, the life of a TSDC tipped pick could be significantly higher than that of a WC pick if it is used properly, catastrophic failure could occur for TSDC tipped picks if the picks are used improperly. Therefore, it is important to understand the cutting mechanism and performance of TSDC tipped picks.

Although rock cutting using mechanical tools has been extensively studied, most of the previous research has focused on either a single or a limited number of the principal parameters. No analytical or numerical model to date has been able to accurately predict the cutting performance of point attack picks due to the major simplifications and the complex nature of rock formations. Few studies have been conducted on the analysis of thermal effects and cutting chips in rock cutting although they are crucial and are indicators of the frictional heat, cutting efficiency and dust generation in a rock cutting operation. In this research, an extensive theoretical and experimental analysis of rock cutting with point attack picks including TSDC and WC tipped picks will be conducted to develop reliable performance prediction models in cutting high strength rocks and get a better insight into the interaction between cutting tools and rock. Pick cutting temperature that is a good indicator of the thermal energy generated at the interface between pick tip and rock will be investigated. The main cutting parameters that have relatively greater contribution on the coarseness index will be chosen to analyse rock chips sizes, chip size distribution, and specific energy. An explicit finite element code LS-DYNA is employed to further simulate the rock cutting process.

1.3 Research objectives and thesis structure

The specific objectives of this study are to:

- Find out the critical parameters that influence the rock cutting process and develop pick force estimation algorithms based on the linear rock cutting test program for TSDC tipped picks;
- Undertake theoretical and experimental studies on the thermal response during the rock cutting process and to investigate the effects of the cutting parameters on pick cutting temperature using an embedded thermocouple technique and infra-red technology;
- Identify and quantify the effect of different cutting parameters on rock chips sizes, chip size distribution, and specific energy;
- Develop explicit finite element models to numerically simulate the rock cutting process and its associated fragmentation as observed in laboratory rock cutting tests

To fulfil the aims above, the remaining thesis is structured as follows:

- Chapter 2 is a comprehensive literature review of the subjects covered in this research study including the rock cutting mechanism, the forces on drag bits and specific energy estimation methods, temperature measurements during rock cutting, as well as numerical methods in rock cutting and fragmentation process;
- Chapter 3 introduces the experimental equipment and techniques used in the current work;
- Chapter 4 describes the optimisation of the rock cutting processes using Taguchi method. Multiple linear regression and neural network techniques are adopted to predict the cutting forces on TSDC tipped picks;
- Chapter 5 presents the development of a temperature measurement system to record the temperature developed between the rock and pick tip via an embedded thermocouple technique and infra-red technology. The influences of the cutting parameters on pick cutting temperature are analysed in this chapter;
- Chapter 6 presents the analysis of rock chips sizes and distribution. The cutting specific energy under various cutting conditions is also investigated using “weigh chips method”;
- Chapter 7 includes the details of explicit FEM model that is used to simulate the rock cutting process. A comparison among the numerical, experimental and analytical results is also presented;
- Chapter 8 summarises the major conclusion in this study. The limitations of this study, along with the potential future applications, will also be presented.

2

Literature review

2.1 Introduction

In the middle of last century the continuous miner, drum shearer, along with the coal plough were invented in US, UK and Germany. Soon afterwards, the concept of roadheaders came into being and became increasingly popular in the 1960s. All these mechanical machines utilise drag bits as cutting tools. An early successful full face tunnel boring machine (TBM) was developed by the Robbins Company after the introduction of disc cutter in 1952. It was used to build an 8 m diameter tunnel at Oahe Dam in South Dakota [18].

Over the past several decades, mechanical excavation machines have been widely used in mining and civil industries as they have many advantages such as increased productivity, reliability, environmentally friendly operations, ease of automation, continuous and selective mining, controllability of the chip size and much safer in comparison with the conventional drill & blast techniques [1-5, 7, 19]. However, the major challenges that limit the use of mechanical machinery in hard rock mining are: (a) excessive abrasive wear of traditional refractory carbides based cutting element, (b) the considerable respirable dust generation and (c) the occurrence of frictional ignition [2, 8, 15, 16, 20-26]. A large number of researchers have begun to address these issues and to extend the capability of the mechanical excavation machines for high strength rock.

2.2 Rock cutting mechanism

The basic operation of all rock excavation machines consists of forcing the cutting tools into the rock and causing it to break. Different excavation machines employ different tools such as drag bits, disc cutters, roller cutters and button cutters for various purposes. Among these cutting tools, drag bits and disc cutters are the most common cutting tools which are mounted in a set pattern on the drum or cutterhead of the machines [27]. The distinction between these two tool categories lies in their cutting actions. Specifically, as can be seen from Figure 2.1, a drag bit attacks the rock along a direction approximately parallel to the rock surface while a disc cutter generates rock breakage by pressing normally to the rock surface [2, 28].

Drag bits are the most efficient and common cutting tools used in the mining industry. These can be classified into radial and point attack/conical picks. These tools are installed at certain intervals and attack angles on a rotating and moving cylindrical or, conical cutterhead on the cutting machines. Drag bits have proven effective and adequate in most coal measures and soft rocks, but are less

successful and suitable when the rock hardness, and especially the abrasiveness, increase because of the high wear rate of these picks [8]. Despite their limitation of high tool wear rate in cutting hard and abrasive rocks, drag picks have a promising and potentially useful future through the development of abrasive resistant tip materials and optimised bits design. These advantages can be coupled with water jet assisted cutting thus enhancing their cutting capacity to higher strength rocks [7].

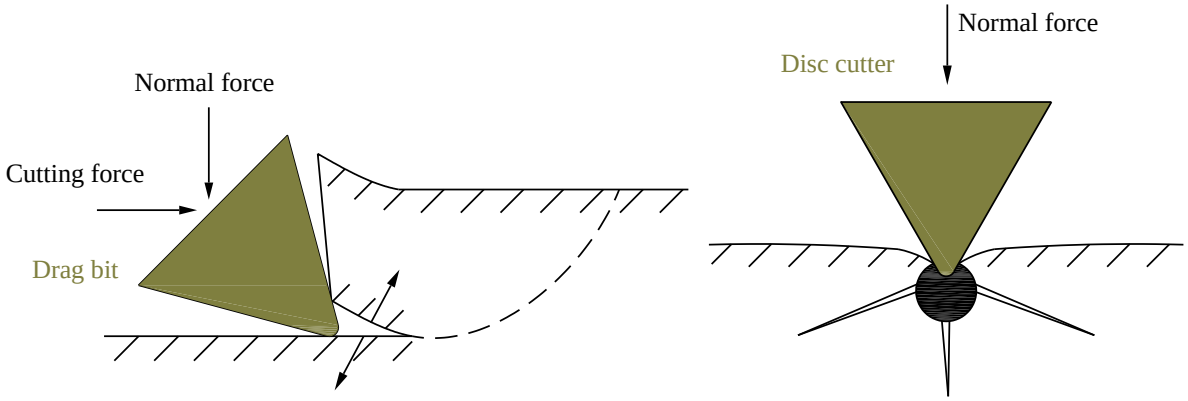

Figure 2.1 Cutting actions of drag bits and disc cutters

Rock failure with drag bits/picks is a brittle fracture process. Rapid oscillations of pick forces as a result of discontinuous formation of rock chips are always observed in a rock cutting process. The rock failure phenomenon with a drag bit has been illustrated by many researchers [29-37]. Four stages are involved in the cycle of cutting process:

1. Generation of primary crushed zone at the edge of drag bit
2. Removal of the primary chip
3. Generation of second crushed zone
4. Profiling of the groove with continued chipping

This process is cyclical and the cutting force will increase again as the pick penetrates forward along the rock surface, leading to a typical saw-tooth shape of the force-time diagram for a pick. When a pick cuts across a rock surface, a groove is created which is much wider than the pick width and the depth of the groove is sometimes deeper than the set depth of cut. The production of excess rock breakage beneath the pick depends mainly on the geometric characteristics of the pick and the direction of cutting relative to bedding and jointing in the rock mass [38].

2.3 Research on cutting forces

The resultant force acting at the tip of a pick consists of three orthogonal components. Cutting force or drag force, which acts along a direction parallel to the cutting direction, is the main force generating the failure crack and forming the rock/coal chip. The normal force corresponds to the force required to keep the pick at the desired depth of cut and acts normal to the rock surface. The sideway or lateral force acts perpendicular to the plane of cutting and normal forces (Figure 2.2); its magnitude is always negligible compared with cutting and normal forces.

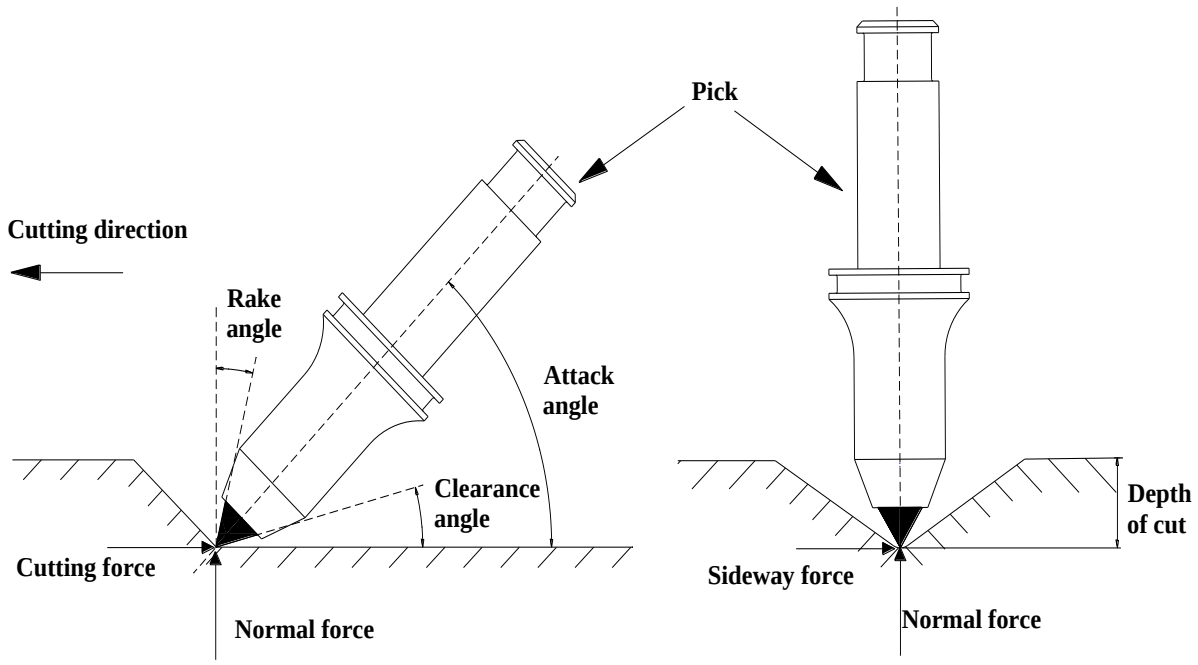

Figure 2.2 Forces on the pick in linear rock cutting

One aspect that limits the current excavation of hard rock is the capacity of cutting tools to bear the high forces [4]. Prediction of the magnitude of cutting forces applied to cutting tools under different cutting scenarios is of paramount importance in bit and machine design, as it can be used to estimate the cutterhead torque and cutter motor power for a given set of geological formation, cutterhead design, and operational conditions of the machine [7, 39]. Therefore, it is vitally important to develop accurate pick force estimation models and to understand the basic rock cutting mechanism, they provide a better insight into the interaction between cutting tools and rock. Estimation of tool forces from full-scale laboratory rock cutting test is the most widely accepted, reliable and precise method [7, 40-42]. Although the full-scale cutting test is usually a very complicated, costly and a time consuming process, and there are only a few of such laboratories

around the world, the cutting forces measured from the laboratory can be directly input into cutterhead design software to determine the capability and efficiency of the selected cutterhead and excavation machines [2, 7, 28, 41-43]. Analytical, semi-empirical and empirical models can be employed as an alternative way to estimate the pick forces when the standard rock cutting rig is not available.

2.3.1 Available theoretical models

In spite of the rather complex nature of rock fragmentation process, to date, a number of theoretical studies have been proposed to investigate the mechanics of rock cutting by making some simplifications and assumptions. Among these researches, Evans' theories for point attack and chisel picks and Nishimatsu's theory for chisel pick are the most recognised ones which have been widely used on efficient cutterhead design of the longwall shearers, surface miners, and roadheaders [4].

2.3.1.1 Modified Ernst-Merchant model (1944)

The foundation of metal cutting research was carried out by Merchant [44-46], who first proposed a model for the metal cutting process by analysing the mechanism of chip formation. Potts and Shuttleworth [47], in 1958, applied and modified this theory for rock cutting by a discontinuous process of shear failure. It is assumed in this theory that the failure criterion on the shear failure plane is satisfied by the Mohr-Coulomb's equation, which is expressed as:

$$\tau_s = S_s + \sigma_n \tan\varphi \tag{2.1}$$

where τ_s, σ_n are the shear and normal stresses at the failure plane, S_s is the shear strength and φ is the angle of internal friction.

The chip is treated as a "separate" body, considering the force and stress equilibrium on it by using least work assumption. The cutting force acting on chisel pick can be given by:

$$Fc = \frac{2 S_s d W \cos(\delta - \alpha)}{\sin\theta_s \cos(\theta_s + \delta - \alpha)} \tag{2.2}$$

where Fc is the peak cutting force, d is the depth of cut, W is chisel pick width, δ is the friction angle between tool and rock, α is the rake angle of tool and θ_s is the shear angle between shear plane and cutting direction. Although this model was originally based on Ernst-Merchant model for

metal cutting, Potts and Shuttleworth, Roxborough and Rispin [47, 48] reported that the calculated value from this model generally coincides with the test results for some kinds of coal and wet chalk.

2.3.1.2 Evans model for chisel picks (1962)

Evans [49] developed a theory to estimate the force involved for breakage of coal by a sharp wedge shaped tool. Two years later, he presented a modified theory by considering the effect of blunting [50]. The following assumptions are made in Evans' model (Figure 2.3):

1. The breakage of coal is caused by tensile stress along a circular curve ab.
2. The failure crack originates from the wedge tip along a direction of horizontal tangent at point a.
3. No friction exists between the wedge and coal, the force F acting on the failure chip is perpendicular to the wedge surface ae.
4. The wedge tears away and rotates the chip about the point b, and this force acts through point b.

Taking moments about point b, considering equilibrium of the chip and using minimum work hypothesis, Evans determined the force Fc required to form the chip is:

$$Fc = \frac{2\sigma_t dW \sin\left[(90^0 - \alpha)/2\right]}{1 - \sin\left[(90^0 - \alpha)/2\right]} \tag{2.3}$$

where σ_t is the tensile strength of the coal, and other notations have been defined in Eq. (2.2). The basic principles of this model were also employed by Roxborough in cutting characteristics of soft rocks like sandstone, limestone and chalk, the experimental results agree well with the theoretical forces predicted from this formula [48, 51].

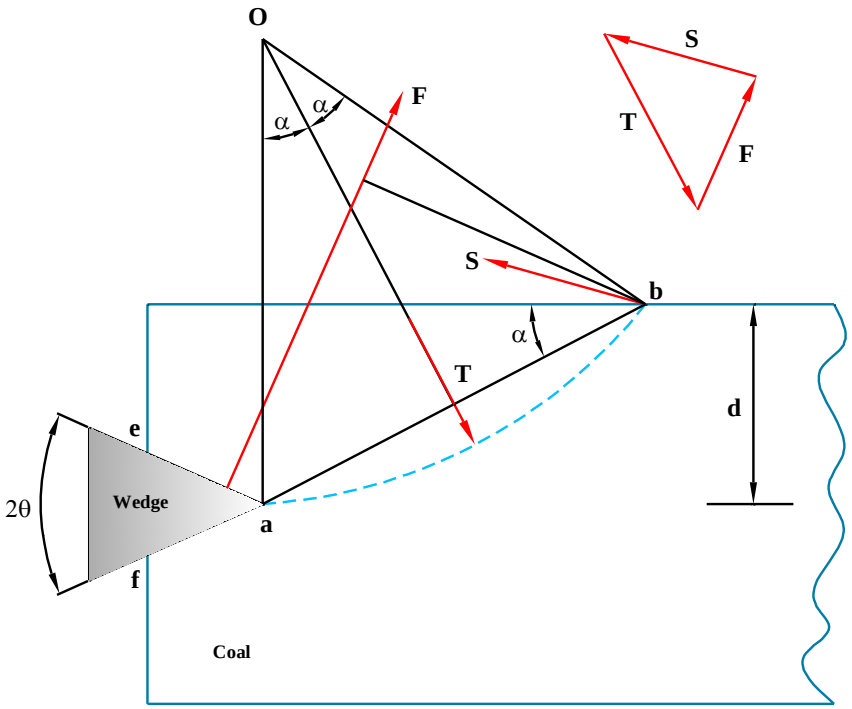

Figure 2.3 Schematic of tensile breakage theory by Evans [49]

2.3.1.3 Nishimatsu model (1972)

Nishimatsu [34], in 1972, postulated a theory for rock cutting on the basis of the observation of the failure process in rock cutting and some simplified assumptions. There is a quite basic similarity between this theory and Merchant's well-known theory in metal cutting. In this theory, he first assumed that the stress distribution along the failure plane (line ab in Figure 2.4) decreases from the tool edge point a to the surface point b because of the severe stress concentration around the tip of the cutting tool. The stress acting on an arbitrary point on the failure plane ab is proportional to the n^{th} power of the distance from this point to the surface point b. It is also assumed that the initiation and extension of the crack satisfies Mohr-Coulomb's failure criterion. Based on the equilibrium of resultant force F and the integration of the resultant stress P, the cutting force is finally defined by:

$$Fc = \frac{2S_s dW \cos\varphi \cos(\delta - \alpha)}{(n+1)(1-\sin(\delta - \alpha + \varphi)} \tag{2.4}$$

The additional notation, n, is the stress distribution factor, which can be empirically estimated as:

$$n = 11.3 - 0.18\alpha \tag{2.5}$$

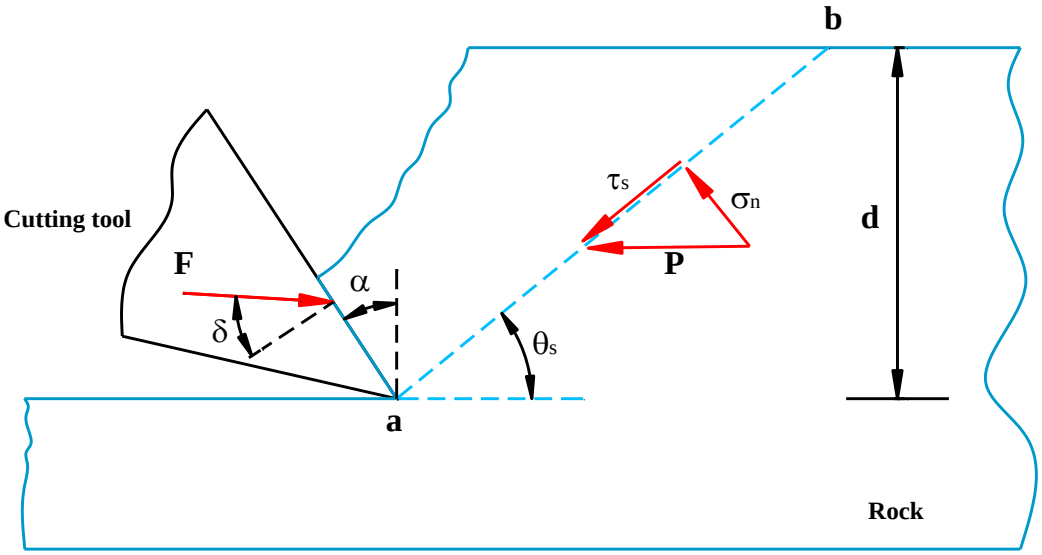

Figure 2.4 The stress distribution and forces according to Nishimatsu [34]

In general, the trends predicted by the above three models for simple chisel picks agree with measured forces [51].

2.3.1.4 Original and modified Evans models for point attack picks

Rock cutting by chisel or wedge picks can be reasonably treated as a two-dimensional idealisation and the required cutting force can be calculated approximately. However, the cutting behaviour of point attack or conical picks is essentially a three-dimensional process, and it is difficult to simplify and estimate the cutting forces under these conditions [5, 52, 53]. Therefore, only a few analytical propositions exist in the literature [5, 39, 52, 54-56].

It was not until 1984 that, Evans [52] put forward the first theory of the cutting force for point attack picks. It is assumed in his model that tensile hoop stresses and radial compressive stresses are produced in the rock by the penetration of a point attack pick as shown in Figure 2.5. When the stress in the rock exceeds its tensile strength, tensile cracking occurs and a V-shaped chip which is symmetric about the central vertical plane is formed.

The forces acting on the half-segment of the potential chip include:

i. The resultant tensile force T acting normal to surface OC, which can be calculated as $\sigma_t d / \cos\phi$ if the radius of the hole a is much less than the penetration depth d, where σ_t is the tensile strength of the rock.
ii. The integration of the elementary forces along the arc CD is the radial bursting force R, which can be determined:

$$R = \int_{-\phi/2}^{\phi/2} qa\cos\beta d\beta = 2qa\sin(\phi/2)$$

where q is the radial compressive stress.

iii. The tensile force acting normal to the vertical radius AB , which can be neglected compared to other forces according to Hurt and Evans [57].

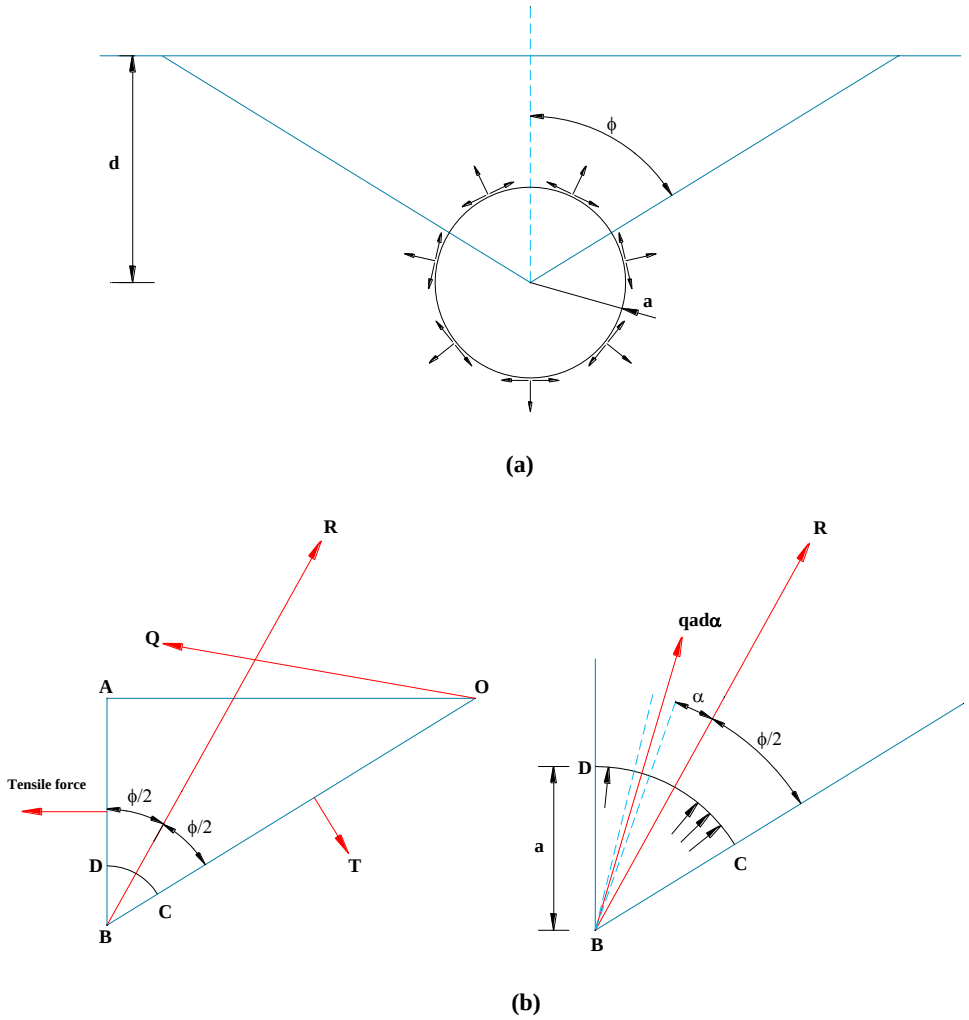

Figure 2.5 (a) Hole under internal pressure (b) Forces acting on the half segment [52]

A fourth force Q is produced by the half-segment levering itself on the shoulder of rock. The following equation presents the equilibrium of moments for the half-segment about point O:

$$R\frac{d}{\cos\phi}\sin(\phi/2) = \sigma_t \frac{d}{\cos\phi}\frac{1}{2}\frac{d}{\cos\phi}$$

Giving

$$q = \frac{\sigma_t}{4}\frac{d}{a}\frac{1}{\cos\phi \sin^2 \phi/2} \tag{2.6}$$

The energy at failure which is proportional to $\sigma_c^{\,2}$ is minimum when

$$2q\frac{dq}{d\phi} = 0 \tag{2.7}$$

Giving $\phi = 60^0$, then the compressive stress q at breakage is:

$$q = 2\sigma_t \frac{d}{a} \tag{2.8}$$

In the second stage of this theory, the conical pick is treated as a cone rather than a circular hole when looking from the side (Figure 2.6). A thin slice of the cone is considered, the elementary area of this thin slice is $2\pi r\delta l$, δl is the increment of length along OD, r is the radius of the thin slice. The value of the depth of point D along the direction of compressive stress is $d/\cos\theta$, where θ is the semi-angle of the cone. The horizontal component δP of the elementary force δR acting on the thin slice can be resolved as:

$$\delta P = \delta R\sin\theta = q\delta A\sin\theta = 2\sigma_t \frac{d}{\cos\theta}\frac{1}{r}2\pi r\delta l\sin\theta = 4\pi\sigma_t \frac{d}{\cos\theta}\delta r \tag{2.9}$$

Thus the total horizontal thrust force for the conical surface is:

$$F_c = \int \mathrm{d}P = 4\pi\sigma_t \frac{d}{\cos\theta}\int_0^a \delta r = \frac{4\pi\sigma_t da}{\cos\theta} \tag{2.10}$$

The force F_c has to overcome the compressive strength of the rock around the cone, can be written as:

$$Fc = \pi a^2\sigma_c \tag{2.11}$$

where σ_c is the uniaxial compressive strength of the rock, eliminate a from Eqs. (2.10) and (2.11), finally F_c is determined

$$Fc = \frac{16\pi\sigma_t^{\,2}d^2}{\sigma_c\cos^2\theta} \tag{2.12}$$

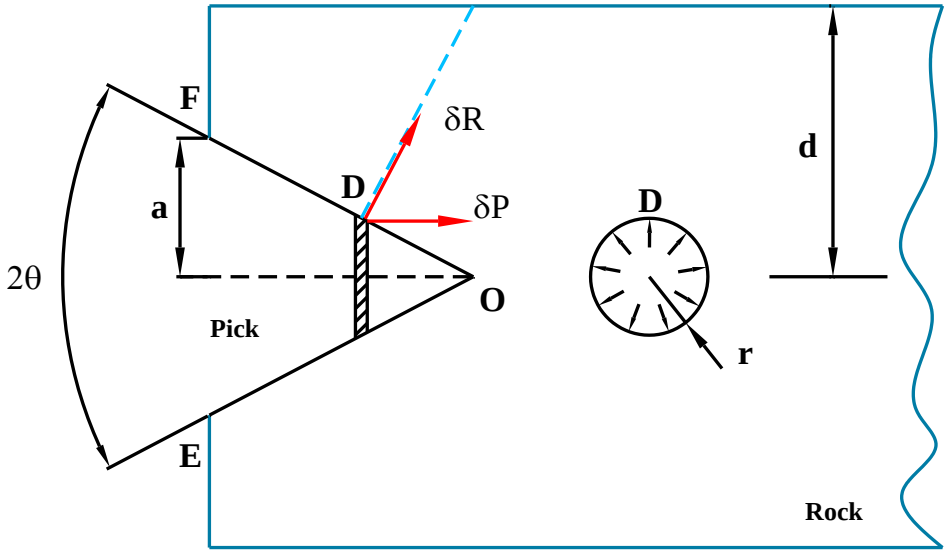

Figure 2.6 Forces acting on a conical hole

The above theory for point attack pick makes it possible to calculate the peak cutting force from rock properties, pick geometry and depth of cut. However, Roxborough and Liu [54], Goktan [55], Goktan and Gunes [39], Bilgin et al. [4] and Bao et al. [5] became aware that the predicted results from the theory often differ from measured results because of their major assumptions, simplifications and approximations. It is pointed out that the discordance might be partly due to the neglect of friction between cutting tool and rock and cutting hole radius. By taking into account the effects of friction and radius of the hole, Roxborough and Liu [54] obtained:

$$Fc = \frac{16\pi {\sigma_t}^2 \sigma_c d^2}{\left[2\sigma_t + \sigma_c \cos\theta/(1+\tan\delta/\tan\theta)\right]^2} \tag{2.13}$$

Goktan also proposed a modified equation for point attack pick based on Evans' theory. As indicated in Eq. (2.14), the peak cutting force is a function of tensile strength of rock, depth of cut, semi tip angle and friction angle between tool and rock. In this equation, one of the deficiencies of the original Evans' theory (that peak cutting force dose not drop to zero when semi pick tip angle θ is zero) is eliminated. Further, the problematic effect of the presence of the uniaxial compressive stress which has an inverse effect on the cutting force disappears.

$$Fc = \frac{4\pi\sigma_t d^2 \sin^2(\theta+\delta)}{\cos(\theta+\delta)} \tag{2.14}$$

It has been claimed that the predicted values from this equation are in good agreement with the published experimental results and could have practical value if validated by further studies.

Despite those modifications and refinements of the original Evans' model, further full scale linear rock cutting experimental data revealed that the cutting force was still significantly underestimated [5, 39]. It is postulated that this could be a result of the rock breakage under symmetrical attack assumption, which is not the case in a practical cutting process. Therefore, Goktan and Gunes [39] modified his previous Eq. (2.14) by considering the asymmetrical cutting condition. The rake angle α (as shown in Figure 2.2) which is defined as the angle between the front face of the pick gauge and the line that is perpendicular to the plane parallel to the direction of cutting under the pick is introduced in this semi-empirical formula.

$$Fc = \frac{12\pi\sigma_t d^2 \sin^2\left[\left(90-\alpha\right)/2+\theta+\delta\right]}{\cos\left[\left(90-\alpha\right)/2+\theta+\delta\right]} \tag{2.15}$$

2.3.1.5 Bao model

Several attempts have been made to analyse the chipping force for brittle materials through edge chipping tests [58-61]. Bao [5] and Yao [62] postulated that if the loading direction in edge chipping is regarded as the direction of cutting in rock cutting and the side face in edge chipping tests is treated as the cutting surface, the edge chipping is similar to the linear rock cutting tests in mining to some extent and might be used to estimate the peak cutting force as shown in Figure 2.7.

Yao [62] made an experimental investigation in which a conical tipped pick has been compared with a pyramidal tipped pick in laboratory edge chipping tests. It was found that the generated rock chips have the similar shape and the chipping energy is proportional to the $9/4^{th}$ power of the depth of cut.

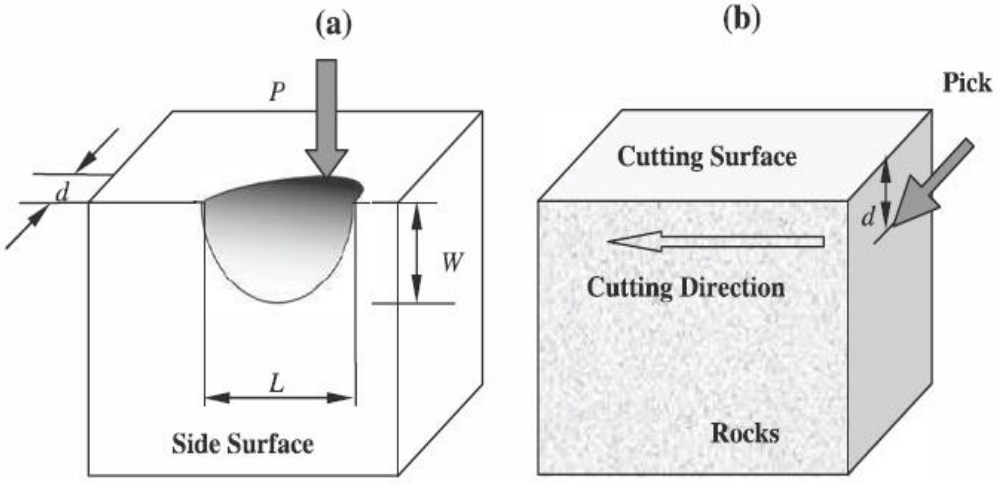

Figure 2.7 (a) Edge chipping of brittle materials and (b) linear rock cutting [5]

In 2011, Bao and Zhang [5] further constructed a model, based on edge chipping experiments results on four kinds of sandstone, to estimate the peak indentation force of point-attack picks by using: (a) fracture mechanics and, (b) geometric similarity of rock chips. In his model, the peak indentation force is derived as:

$$Pc = \left(\bar{H}\right)^{1/3} \left(6\frac{\omega}{k} G_s\right)^{2/3} d^{4/3} \qquad (2.16)$$

where:

$G_s = \frac{K^2_{IC}}{E}$

$\bar{H}$ = the corresponding "hardness" through the indentation tests

ω = geometric factor dependent on the pick geometry

k = geometric factor of the pick independent of rock properties

G_s = strain energy release rate of the rock

K_{IC} = toughness of the rock

E = young's modulus of the rock

d = depth of cut

It has been shown that predicted peak indentation force correlated well with the measured force. However, it needs to be pointed out that using edge chipping tests to simulate the rock cutting process may suffer from the disadvantages of the quasi-static process of edge chipping tests. The effect of attack angle has not been taken into account in this model, which might result in inaccurate predictions for the practical rock cutting forces.

2.3.1.6 Other theoretical studies on cutting forces

By analysing the chip geometry and the variation of cutting forces, Ranman [63] observed that the largest chips produced during one single cut had the same shape and the variation of the distance between force peaks met the Poisson distribution. A simplified energy model has been created to calculate mean and peak forces from the input energy per unit length of cut.

$$E_e = L_t \frac{Fc}{2} \tag{2.17}$$

$$F_m = \frac{Fc}{3} \tag{2.18}$$

where E_e is the input energy, L_t is the total cutting length and F_m is the mean cutting force.

Cherepanov [64, 65] established a mathematical model for the maximum cutting resistance force by theoretical analysis of oscillations during cutting of rocks using fracture mechanics. In 1992, linear elastic fracture mechanics and DDM (displacement discontinuity method) were used by Guo and co-workers to study the rock crack behaviour involved in rock cutting process due to drag bit cutting [66]. It was reported that fracture mechanics gave a greater insight into the cutting mechanism in terms of: (a) crack propagation path, (b) the corresponding load requirements and (c) the stability of the crack propagation when compared with the traditional rock mechanics methods such as the well known Mohr-Coulomb criterion.

2.3.2 Empirical studies

Although the above theoretical studies led to a better insight into the coal or rock cutting process, as pointed out by Bilgin [4] and Bao [5], the cutting force estimation from these models remains very different from the cutting force in actual three dimension situations due to the major simplifications of this problem as well as the complex petrographic, mineralogical, heterogeneous and anisotropic nature of rocks. Semi-empirical or empirical models may serve as a better substitution since they are based on the analysis of the measured test data. A number of empirical equations for cutting force have been proposed for the last 50 years. However, most of them have considered either a single or some of the important factors. In 1995, Goktan [56] developed a semi-empirical equation to estimate the cutting forces of chisel picks based on the experiment data of previous researchers. The rock uniaxial compressive strength in the experiment data ranges from 80 to 180 *MPa* .

$$Fc = \frac{(0.8 - 0.01(\sigma_c / \sigma_t))\sigma_c dW}{\sin(90^o - \alpha) + \cos(90^o - \alpha)} \tag{2.19}$$

Nowadays, statistical methods such as multiple linear and nonlinear regressions, the fuzzy logic and artificial neural networks have become a powerful tool for the development of predictive models in mining and tunnelling applications [7, 67-79]. Yilmaz and co-workers [7] presented an empirical equation to predict the cutting force on chisel picks by using multiple linear regression analysis. Stepwise regression procedures are employed to choose the significant variables. Six independent

variables including shear strength of rock S_s, depth of cut d, angle of sliding friction between rock and the pick δ, pick width W, rake angle α and uniaxial compressive strength σ_c are included in the following predictor equation:

$$Fc = -24.504 + 0.513S_s + 1.873d + 0.249\delta + 0.227W - 0.154\alpha - 0.047\sigma_c \qquad (2.20)$$

The coefficient of determination (also called R-squared) value, the standard error of the estimate and probability value ($p-$value) are used to check the validity and statistical significance of the derived model.

Bilgin et al. [4] conducted a wide range of full scale linear rock cutting tests on different types of rock specimens which have uniaxial compressive strength ranging from 6 to 174 MPa. The statistical relationship between cutter forces and rock properties was investigated. It was found that the measured force values were best correlated with uniaxial compressive strength and tensile strength. However, cutting performance was also dominantly affected by other rock properties such as Schmidt hammer rebound values, static and dynamic elasticity modulus. The comparison between theoretical cutting force values and experimental cutting force values indicated that theories in rock cutting mechanics definitely need to be improved. Based on the rock cutting data set from a full scale rock cutting program by Balci and Bilgin [19], Tiryaki [79] built six different empirical predictor equations of the mean cutting force for point attack pick. Rock properties and operational variables such as spacing and depth of cut were incorporated in his models.

2.4 Specific energy

Specific energy which is defined as the work done per unit volume of rock cut is of paramount importance to determine the efficiency of mechanical excavators and the cuttability of rock materials [4, 78, 80]. Hughes [80] and Mellor [81] theoretically correlated the specific energy with compressive strength σ_c and secant elasticity modulus E_1 of the rock, and derived the specific energy as:

$$SE = \frac{\sigma_c^{\,2}}{2E_1} \qquad (2.21)$$

However, detailed experimental studies reveal that other rock properties also are important factors that influence specific energy. Rock properties such as cone indenter index, cementation coefficient,

Schmidt hammer rebound value and compressive strength were correlated with specific energy by Fowell [82] and Mcfeat-Smith [83]. By analysing the available chisel pick cutting experimental data, Goktan [84] found out that there is no reliable relationship between the brittleness related to compressive and tensile strength and specific energy.

Copur et al. [3, 85] developed a predictor equation of the optimal specific energy obtained from full scale linear rock cutting tests as a function of the uniaxial compressive strength and Brazilian tensile strength values of rocks. They also correlated cutting performance including cutting force, normal force and specific energy with the brittleness index.

Bilgin and Balci [4, 19, 41] established an extensive rock cutting program with uniaxial compressive strength of rocks ranging from 6 to 174 MPa. From these full scale linear rock cutting data, statistical relations between optimal specific energy and different rock properties such as compressive strength, tensile strength, and static and dynamic elasticity module were obtained. It was concluded that uniaxial compressive strength and tensile strength are the best predictors for estimating optimal specific energy.

A number of researchers found that specific energy was also close related to operational cutting parameters such as attack angle, depth of cut and the spacing between adjacent cuts. Pick attack angle which is defined as the angle between the pick axis and the plane parallel to the cutting direction under the pick (Figure 2.2) is the significant angle affecting the pick performance. Studies in MRDE (Mining and Research and Development Establishment of National Coal Board)) and EMI (Earth Mechanics Institute) of CSM (Colorado School of Mines) revealed that pick forces and specific energy decrease rapidly as the attack angle increases from 40 ° to 50 °. After that any increase in the attack angle resulted in increases in both parameters [57, 86]. This change in pick forces may be caused by the change of the area of contact between the pick and the coal surface, and hence the generation of high stress concentrations by the pick on the coal. Lower pick forces are required to break the coal because of the lower contact area coupled with higher stress concentrations at higher attack angles up to about 50 °. The smaller attack angle will not only have a larger area of contact, but it will also require a larger normal force to maintain the penetration into the coal. Attack angles after 50 ° result in higher contact areas between the pick and the coal face, generating higher pick forces and specific energy. It has been found that specific energy decreases dramatically to a certain level with increasing depth of cut [48, 87-89]. This indicates that cutting efficiency of the pick improves as the depth of cut increases.

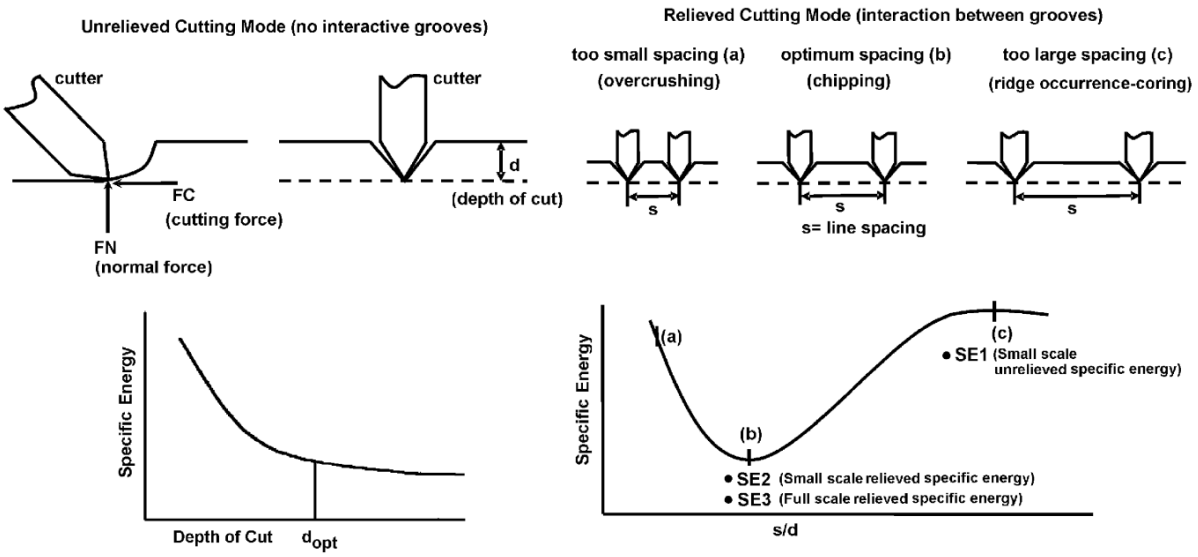

Figure 2.8 General effect of spacing between adjacent cuts on specific energy [4]

The effect of spacing on specific energy is illustrated in Figure 2.8. As can be seen from the figure, cutting efficiency increases significantly as the line spacing varies from a small to an optimal value; this results in a minimum in the specific energy. When the line spacing is too small the rock is over-crushed. After this optimal spacing, the cutting efficiency drops rapidly with increasing line spacing due to the formation of a ridge. Under these conditions groove-deepening occurs.

2.5 Tool chip interface temperature

The considerable frictional heating between WC tipped picks and the rock in high strength rock cutting processes is a significant hazard to underground mining safety, and has been the cause of a number of mining disasters in Australia and overseas [90-92]. Most cases of frictional ignition in Australia were caused by worn cutter picks striking a high silica material (conglomerate roof, sandstone roof or material associated with geological structures) in gassy conditions [92]. The frictional heat generated is also responsible for the temperature rise at the pick-rock interface, which has a significant effect on the wear rate of cutting tool [90, 93]. A number of researchers realised that severe reduction in drag bit performance and significant thermal stress in the cutting tool as well as the rock might be caused by the high temperatures encountered at the pick-rock interface [94-100]. Thus temperature measurement at the pick-rock interface is extremely important in determining the performance and economy of drag bits as well as providing a good indicator of the thermal energy generated in the rock cutting process which can be used to assess the risk of frictional ignition during pick cutting.

There are a number of direct or indirect temperature measurement techniques including tool-work (dynamic) thermocouple, embedded thermocouple, resistance thermometry, infrared sensors, metallographic techniques and thin film sensors in metal machining process. Some of these methods can be used to measure the average temperature in a certain area, while others can determine the cutting temperature distribution.

Thermocouple techniques (e.g., dynamic, embedded and thin film thermocouples) are based on the principle that an electromotive force (emf) is produced when there is a temperature gradient between the hot and cold junctions formed when two dissimilar metals are joined together at these junctions. Thermocouple techniques have been widely used in various machining process such as turning [101, 102], grinding [103, 104], milling [105] and drilling [106] to directly measure the average temperature in a specific area near the cutting edge. However, this method is limited as it cannot indicate any temperature distribution or high local temperature which only appears for short periods. Thus, radiation techniques such as infrared radiation and infrared cameras have been used to determine the distribution of temperature at the tool-chip interface [107-110]. Other non-invasive measurements through metallographic evaluation of the microstructure and/or the microhardness changes, thin film sensors have also been developed [111, 112].

Direct temperature measurements by embedding thermocouple in metal machining have also been exploited in rock cutting with minor modification [99, 113]. A special thermocouple configuration was developed by Cools [99] to measure the temperature on the chisel surface during rock cutting. The operational temperature of the thermocouples ranged from 0 ^{o}C to 1100 ^{o}C, the maximum temperature that can be measured is about 1400 ^{o}C. The arrangement of thermocouples on the chisel pick surface was shown in Figure 2.9. Two rock types namely Felser sandstone and Euville limestone, with the uniaxial compressive strength of 19.5 MPa and 25.2 MPa respectively, were used in these tests. It was found that the maximum temperatures on the cutting surface of chisel pick for sandstone and limestone blocks were approximately 550 ^{o}C and 800 ^{o}C respectively. Temperature was over 3 times lower at a distance of 0.5 mm from the cutting surface. Apart from abrasive wear, the occurrence of plastic deformation was also observed during the tests.

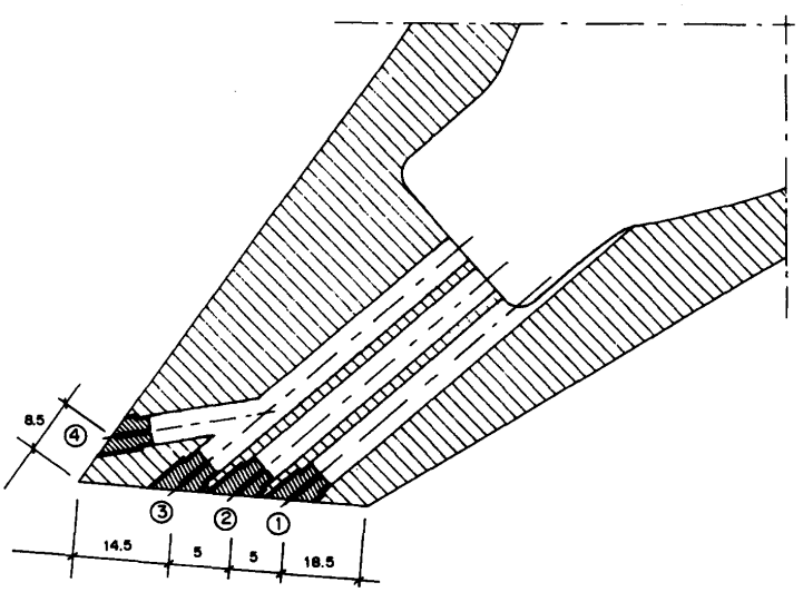

Figure 2.9 Arrangement of thermocouples [113]

Martin and Fowell [8] investigated the factors influencing the onset of severe drag tool wear in rock cutting. Each chisel pick was fitted with a K-type thermocouple, which was located inside of a tungsten carbide insert near the pick tip. A Calex Ranger infrared-red gun specially calibrated for tungsten carbide was mounted at the back of the pick to measure the temperature over the pointed tip region of the tungsten carbide insert at the end of each cut. High pressure water jet assistance (HPWJA), with a water pressure of 27.6 MPa, was employed in part of the tests. The results of this study indicated:

- A correlation existed between tool tip temperature and normal force when cutting speed was constant.
- The tool life was extended when high pressure water jet assistance was employed, which could be of importance in the application of WC tipped picks in rock with high strength.
- The heat generated at the tip-rock interface which is a determining factor accounting for severe tool wear might be quantified.
- New materials need to be exploited that can retain high values of physical properties like indentation hardness thus have better wear performance.
- An elementary mathematical model, which can be used to estimate the heat generation and its influence on tool wear and hence tool life, was developed. Tool normal force and cutting speed that will induce the onset of severe wear rate of cutting tool due to the thermal weakening of cutting material are involved in this model.

In 2005, Loui [93] proposed a 2D transient heat transfer model to analyse the temperature rise at tool chip interface using a finite element method. Laboratory scale micro-picks for rotary drag cutting were used to simulate the practical cutting action. Temperature measurement in this study was made by inserting a copper-constantan thermocouple into a 1-mm diameter hole drilled at a distance of 2 mm from the free surface. It has been shown in the heat transfer model that the temperature rose steeply at the outset of the cutting and stabilised after a few minutes continuous cutting. The temperature contour profile from finite element analysis is shown in Figure 2.10. The trend of the temperature agreed well with the experimental observation despite the over estimation of the magnitude of the temperature which might be due to the assumption that all the frictional heat generated at the flank face of the pick was converted into frictional heat . However, further modifications and developments to the model are needed to enable: (a) closer correlation to the practical cutting action and (b) a more detailed three dimensional simulation that produces more realistic temperature values.

Despite these few studies, there still exist numerous difficulties and limitations to the temperature measurement during rock cutting process [114]. For instance, due to the different physical properties of the cutting tools and workpieces, tool-work thermocouple and metallographic techniques could not be used in rock cutting process. Temperature measurements through infrared methods are significantly affected by chip obstruction [102, 115].

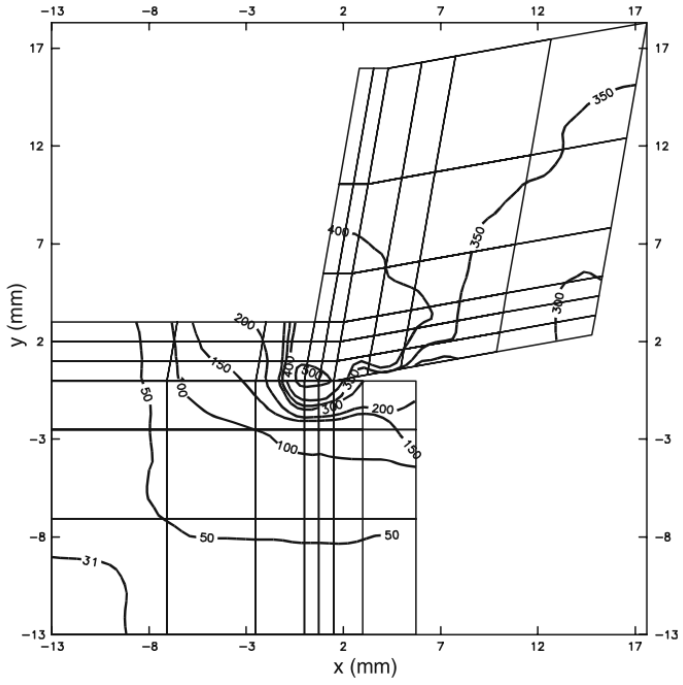

Figure 2.10 Temperature contour according to Loui [93]

2.6 Numerical modelling of cutter-rock interaction

The modelling and simulation of mechanical cutting have proved to be extremely difficult due to the involvement of various physical phenomena including large elastic-plastic deformation, complicated contact or friction conditions, thermo-mechanical coupling, crack propagation and chip formation and separation mechanisms [116]. Similar difficulties are met in rock cutting processes. The discontinuous, anisotropic, inhomogeneous and non-elastic nature of rock makes it even more difficult to model this simulation the rock cutting processes. During the past few years, numerical methods including the finite element method (FEM), the finite difference method (FDM), discrete element method (DEM) and boundary element method (BEM) have been widely used in the analysis of rock cutting process.

The displacement discontinuity method (DDM), as originally developed by Crouch [117], is an efficient indirect BEM in simulating rock crack or fracture problems as the cracks can be represented by single fracture elements. Compared with FEM, the solution time of the system is much shorter because only the boundary needs to be discretised. Guo [66, 118] conducted an analysis on the rock crack propagation due to drag bit using a DDM. The crack tip stress singularity was achieved using a special crack tip element. The stress intensity factors were determined through the displacement correlation method [119]. The crack propagation path was predicted based on the Griffith-Erwin and the maximum tensile stress theories [120]. Tan et al. [121] conducted a study on cracks and chips by use of indentation tools and a DDM coupled with an energy release rate criterion. It was found that multiple mechanisms of either tension or shear or their combinations caused the formation of chips. However, BEM was limited to the analysis of the initial crack growth and it could not be applied to analyse the dynamic chipping process.

FDM, unlike the conventional finite element method, does not need to solve global stiffness matrix equation systems. Perhaps the fast Lagrangian analysis of continuum (FLAC) code is the most well-known finite difference code used in geo-mechanical problems now. The 2D FDM code FLAC^{2D} was successfully employed by Huang [122] to investigate the influence of lateral confinement on the formation of tensile cracks. The results revealed that the lateral confining stress of the rock had a significant influence on the crack initiation. By the incorporation of the local degradation model into FLAC, Fang and Harrison [123] developed a numerical methodology to predict the non-linear macroscopic behaviour involved in the brittle rock fracture process. The results indicated that the local degradation model was a powerful method to the simulation of a wide range of phenomena in relating the macroscopic fracture behaviour to the microscopic material behaviour. More recently, Tulu and co-workers [124-128] from West Virginia University adopted the commercial 3D FDM

code FLAC^{3D} to analyse the interaction between drill cutter and rock, as shown in Figure 2.11. Elements are treated as a "null" material or removed from the model when approaching failure. The removal of "chips" was modelled by the failure of the element zones which satisfies the strain softening Mohr-Coulomb Criterion. The major problems that limit the use of FLAC in rock cutting are: (a) the lack of robust material constitutive models and (b) the non-connectivity of failed elements.

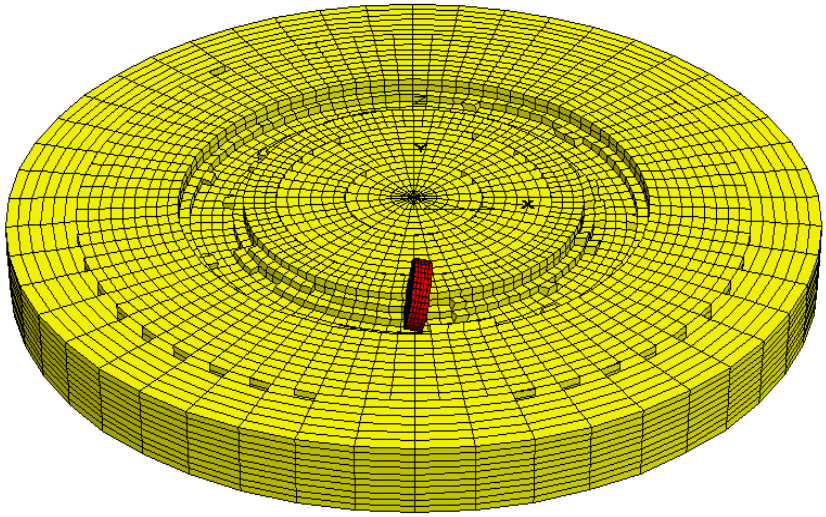

Figure 2.11 The interaction of the rock sample and a single cutter [128]

The DEM (discrete element method or distinct element method) is a numerical method to simulate the motion of a large number of small, discrete particles. It has been widely recognized as an effective approach in a wide range of engineering applications, including granular flows, powder mechanics, and rock mechanics. Particle flow codes such as PFC-2D and PFC-3D are the most widely used codes for modelling rock cutting problems. In 1999, a 2D rock cutting simulation was first conducted by Huang using a commercial DEM code PFC^{2D} [129]. Two failure modes, including ductile at small depth of cut and brittle at large depth of cut were reproduced in this study. Inspired by Huang's work, an investigation of the correlation between cutting morphologies and low bore hole conditions was performed by Block and Jin using a two-dimensional Discrete Element Method [130]. The significant difference between their method and the previous works is the determination of the energy dissipation rate within the rock volume during the entire cutting process, which was determined from the spatially averaged grain level forces. Their results showed that a predominant relationship existed between the downhole conditions and the transition of rock failure modes in terms of cuttings morphologies (chip-like to ribbon-like). The brittle and ductile failure modes with a single polycrystalline diamond compact (PDC) cutter were shown in Figure 2.12(a), and Figure 2.12(b).

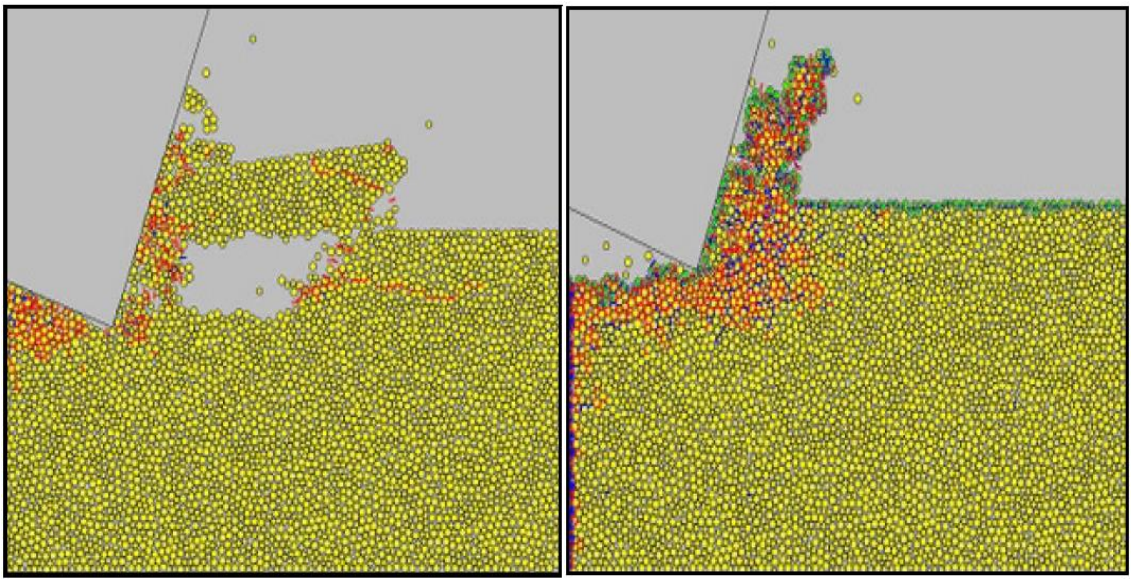

(a) (b)

Figure 2.12 2D DEM simulation of linear slab cutting with a PDC cutter (a) brittle failure mode (b) ductile failure mode [130]

More recently, Su and Akcin [42] adopted PFC^{3D} to simulate rock cutting processes. A comparison was made between the cutting forces obtained from the simulations and those calculated from theoretical models and those observed in laboratory cutting tests. Although accurate quantitative tool forces were not achieved, it was observed that reasonable agreements and strong correlations existed between the modelling and the theoretical predicted forces. Recently, both 2D and 3D models were established by Rojek [131]. The simulation of the rock cutting process with point attack picks on a roadheader is shown in Figure 2.13. Rojek considered that more comprehensive testing including triaxial compression, direct shear and fracture mechanics tests could be conducted to calibrate the model. Improvement to the accuracy of the analysis of rock cutting would be obtained if these parameters were included in the modelling.

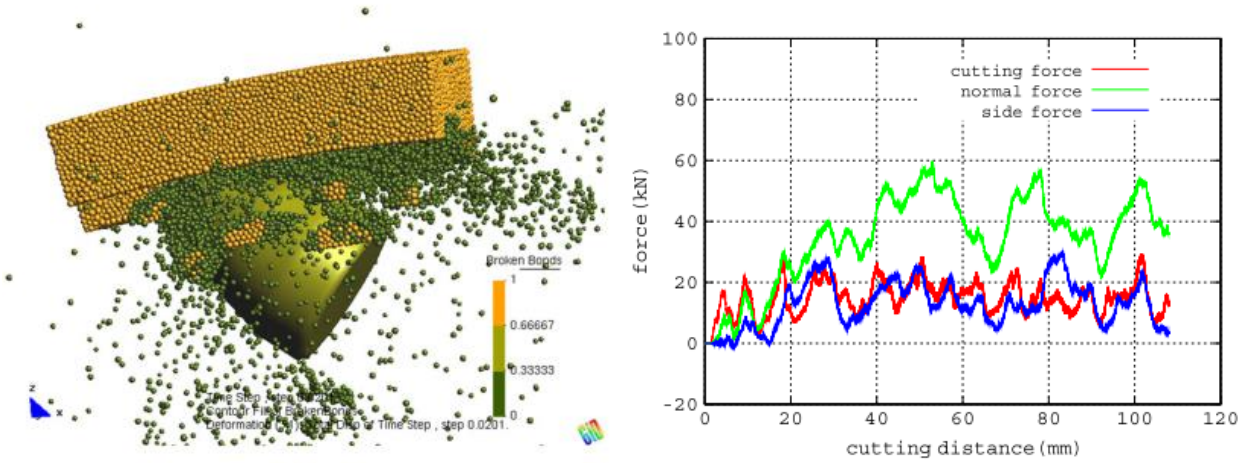

Figure 2.13 Discrete element simulation of the laboratory rock cutting tests [131]

Using the Finite Element Method (FEM) to model the rock cutting problem is challenging as it requires (a) fine element sizes, (b) complex definitions of contact between the cutter and the rock as well as the contact between new surfaces, (c) continuous re-meshing with the advance of the cutter, and (d) complicated crack initiation and propagation process.

The Rock Tool Interaction code (R-T^{2D}) was developed by Liu based on the Rock Failure Process Analysis (RFPA) model and the finite element analysis method to simulate the progressive rock fragmentation process in rock cutting (Figure 2.14) [132-138]. The heterogeneity of the rock was simulated on the basis of statistical approaches and the main physical-mechanical properties of rock. A double elliptic strength criterion rather than Mohr-Coulomb strength criterion was incorporated to describe the rock failure process. A special 'smeared crack' approach was used in these codes. In this approach, a rock element failed when the stress or strain of the element reached the failure threshold, it remains a continuum of the whole domain but loses its load carrying capacity (stiffness and/or strength) in certain directions. As shown in Figure 2.14, the 'smeared crack' is characterized in darker colour, which did not represent an explicit or dynamic cracking process. Thus, this technique was limited to the initial stage of contact.

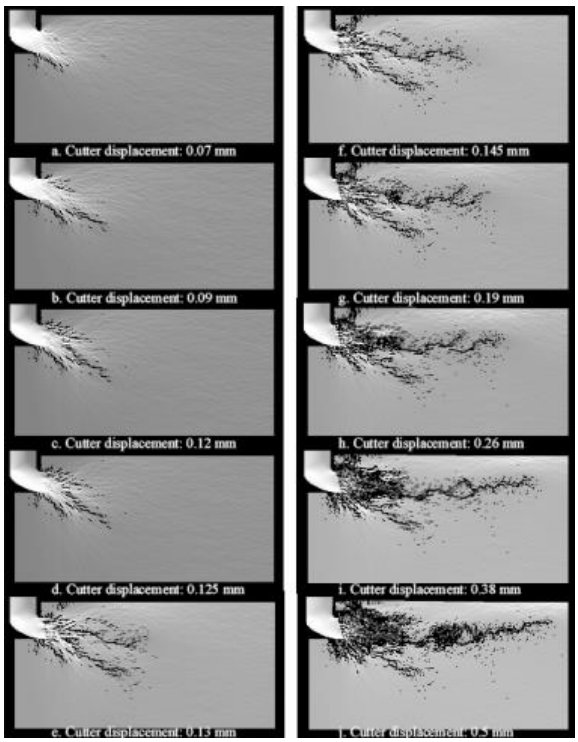

Figure 2.14 Rock cutting simulated with R-T^{2D} [134]

In 2005, Yu [139] modelled the rotary cutting process of a laboratory-scale cutting drum by using a dynamic finite element method (Figure 2.15). An "element erosion" algorithm was incorporated in the model. However, neither the cracks in the rock nor a robust constitutive material model were considered in this model.

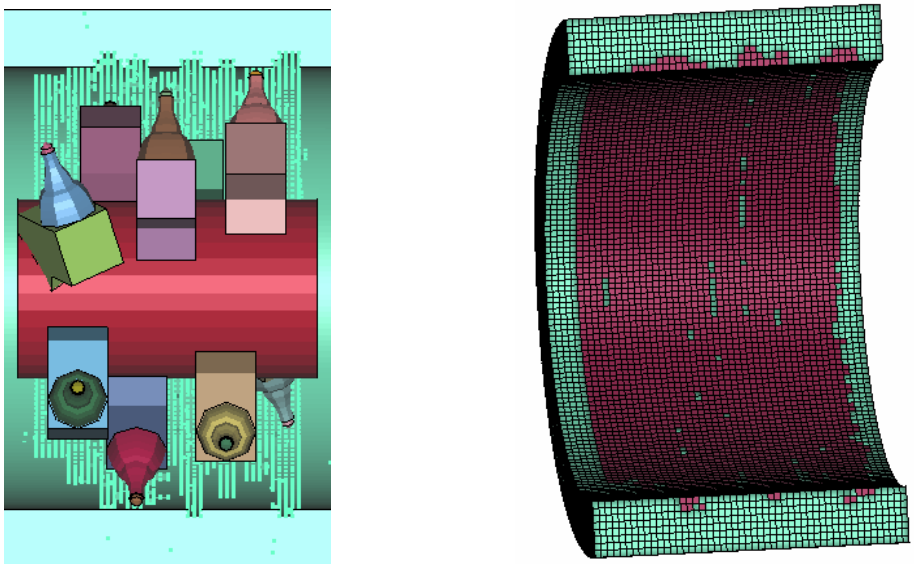

Figure 2.15 Simulation of the rotary rock cutting process of a laboratory-scale drum [139]

Jaime et al. [140] used the explicit 3D FEM code LS-DYNA to reproduce the two failure modes (ductile for shallow cuts, brittle for deep cuts) in scratching tests. They analysed the suitability of various approaches including the Eulerian, ALE (Arbitrary Lagrangian Eulerian) formulation, and

the Lagrange formulation for the modelling of rock cutting and found that only the later was appropriate. A visco-elastic-plastic damage model was incorporated as the material model in their study. The results of the basic Lagrangian rock cutting model gave them reasonable matches of both the fracture modes and the cutting forces magnitudes to the laboratory tests. However, most of their works was limited to the small scale problems. When simulating three dimensional groove cutting, the force values were found to be inconsistent with laboratory results, especially at deep cuts.

Fontoura et al. [141] adopted the commercial code ABAQUS to simulate 2D slab cutting and 3D circular groove cutting, as shown in Figure 2.16. A model of contact with an erosion criterion was also used in this study. Their results indicated that the pattern and magnitude of the predicted forces were quite sensitive to the mesh size and confining pressure. This study was limited to the ductile regime.

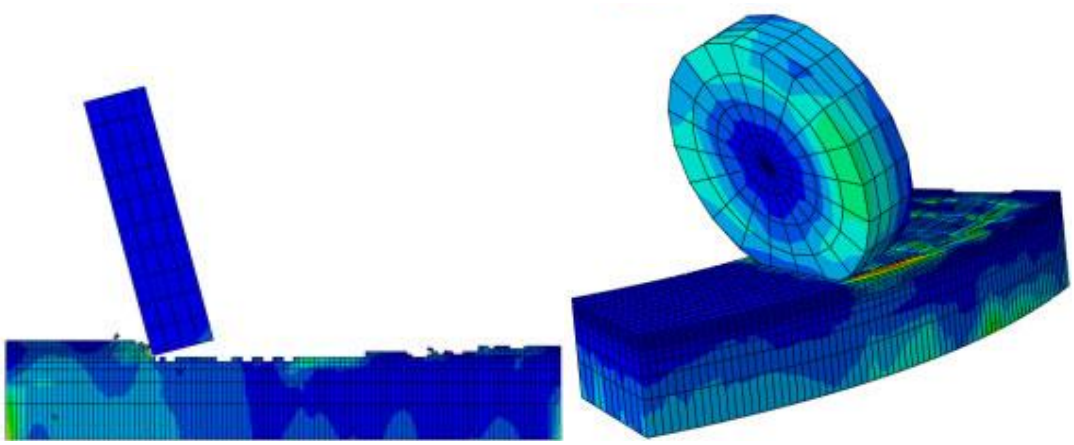

Figure 2.16 Simulation of 2D linear cutting and 3D circular groove cutting [141]

2.7 Concluding remarks

A comprehensive literature survey of rock cutting with point attack or chisel picks is presented in this chapter. An introduction of the cutting tools and rock cutting mechanism was given, followed by the description of the analytical and empirical force estimation models. It has been shown that several theoretical studies have been proposed to investigate the mechanics of rock cutting by point attack or chisel picks, but the cutting performance estimated from those studies remains very different from that in actual three dimension situations due to the major simplifications and the complex nature of rock formations. Semi-empirical or empirical models may serve as a better substitution since they are based on the analysis of the measured test data. However, the vast majority of the previous research has focused on either a single or a limited number of the principal parameters. Few studies have been conducted on the rock cutting by diamond composite picks.

Little work has been done in the analysis of cutting temperature and rock chips although they are crucial and are indicators of the frictional heat or thermal energy, cutting efficiency and dust generation in a rock cutting operation.

Various numerical approaches for modelling the tool-rock interaction problems were examined, it was revealed that the DEM and FEM are the most popular methods. The discrete element model is capable of providing valuable information of the key phenomena in a rock cutting process. The micro level and discrete nature of the particles in DEM are the major disadvantages that limit it in rock cutting. As for the FEM technique, the 'smeared crack' based FEM is not able to model the dynamic fragmentation process. The explicit FEM code LS-DYNA, on the other hand, is capable of capturing the crack initiation, crack propagation and dynamic interactions might be suitable in this study.

To address these limitations and optimise the application of TSDC tipped picks, this thesis aimed to improve the understanding of the rock cutting process and mechanisms, in particular to gain a better insight into the interaction between tools and rocks through systematic experimental and numerical studies. Specifically, an extensive theoretical and experimental analysis of rock cutting with point attack picks including TSDC and WC tipped picks will be conducted to develop reliable performance prediction models in cutting high strength rocks and get a better insight into the interaction between cutting tools and rock. Pick cutting temperature that is a good indicator of the thermal energy generated at the interface between pick tip and rock will be investigated. The main cutting parameters that have relatively greater contribution on the coarseness index will be chosen to analyse rock chips sizes, chip size distribution, and specific energy. An explicit finite element code LS-DYNA is employed to further simulate the rock cutting process.

3

Experimental equipment and rock properties

3.1 Introduction

The experimental equipment and instrumentation that were used throughout the research program are introduced in this chapter. Some auxiliary facilities for the determination of the rock properties and sample preparation are also presented.

3.2 Linear rock cutting planer

Rock cutting tests were performed on a linear rock cutting planer in CSIRO's Rock Cutting Laboratory. Figure 3.1 shows a schematic view of the planer. It consisted of a solid stationary main frame, a crosshead, a tri-axial force dynamometer and a cutting table. The rock sample was mounted on the cutting table, and moved against the stationary cutting tool during the experiments.

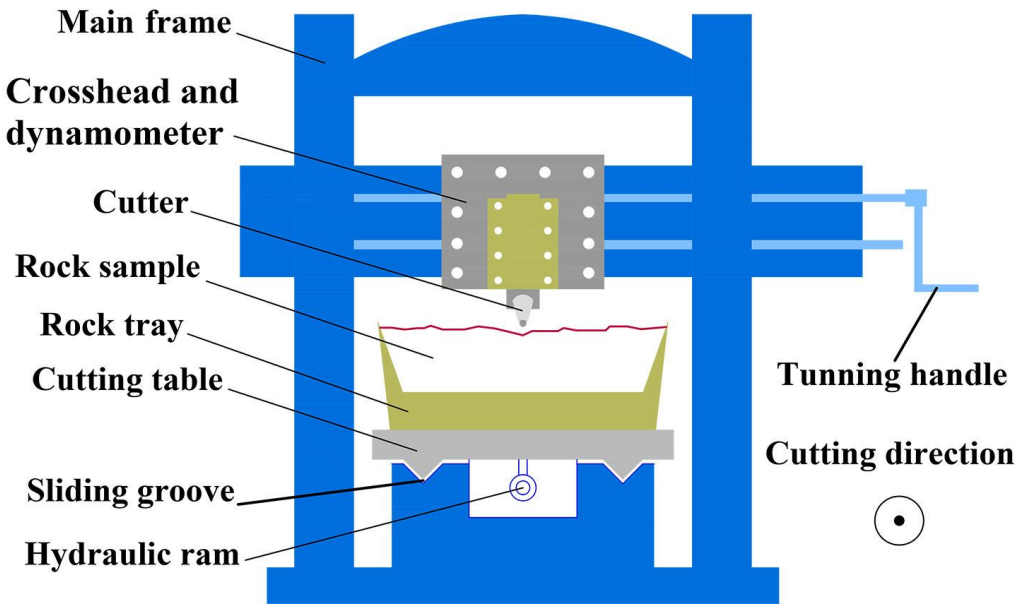

Figure 3.1 Schematic view of linear rock cutting planer

The cutting table and rock are driven horizontally by a hydraulic ram. The travelling stroke of the table is 3 meters and its speed could be controlled from 0.1 to 3.0 m/s.

The cutting tool can be adjusted both laterally and vertically, which allows the cutting tool to be set to its required position relatively to the rock sample. The setting of the cutting tool is manually driven by turning a handle (gears and screw system). Once the desired depth of cut (penetration) is

achieved, the tool is secured into position using large locking screws. An accuracy of 0.05 mm of penetration can be achieved using a laser displacement sensor attached to the cutter assembly.

The rock sample was embedded in concrete in a steel rock tray which was rigidly secured to the cutting table. Both sides of the rock sample were also clamped to prevent from splitting when the cutting groove was near the edges of the rock sample (Figure 3.2). The initial dimensions of the rock sample were of 450 mm x 450 mm x 1800 mm.

A tri-axial dynamometer and data acquisition system were bolted to the crosshead to record the cutter forces. The linear rock cutting planer was controlled out by a PC equipped with LabVIEW software and a National Instruments A/D card. Several limit switches and controls were incorporated into the linear rock cutting planer. These included safety stop switches, relays and timing controls for automatic trimming of the rock surface at some test settings.

Figure 3.2 Rock sample on the linear rock cutting planer

3.3 Dynamometer

The forces on the cutter during the cutting tests can be resolved into three orthogonal components. The cutting force or drag force F_c acting parallel to the cutting direction is the main force

generating the failure crack and forming the rock chips. The normal force F_n acts normal to the rock surface being cut and the sideway force F_s acts perpendicular to the plane of cutting and normal forces (see Figure 2.3). These force components were measured as changes of voltages across strain gauge bridges mounted on the aluminium plate triaxial dynamometer.

The dynamometer was machined out of a solid plate of aluminium alloy to give essentially a central plate on which the cutting tool is mounted. The material of the dynamometer is aluminium alloy as its sensitivity is suitable for transmitting the forces acting of the cutting tool to the strain gauges. The properties of the alloy are listed in Table 3.1. All rock cutting tests were performed within the safety envelope of the dynamometer.

Table 3.1 Properties of the dynamometer material (alloy 4365)

Properties	Unit	
Yield strength	MPa	405
Young's modulus	MPa	67560
Density	kg/m^3	2800
Thermal expansion	$1/^oC$	2.4×10^{-5}

3.4 Thermocouple configuration

The temperature at the interface of pick tip and rock sample was measured by a special thermocouple configuration. Type K chromel-alumel thermocouple with a sensitivity of 41 $\mu V / ^oC$ was used. The upper limit of the temperature to be measured by this type of thermocouple is about 1350 ^oC.

As shown in Figure 3.3, a hole was drilled into the WC pick using a Herless Electric Discharge Machine (EDM) operating at 4 volts and 1 amp with a 1.5 mm diameter copper wire. Two half plugs made of WC were specially designed, each half plug having a diameter of 3 mm and length of approximately 4 mm. In each half plug, two grooves were drilled with diameters of 0.5 mm and 0.5 mm in between. Two insulated thermocouple wires were glued into the grooves on one half of the plug and the end of each wire stops at the surface of the plug. The two halves were joined together to make a cylindrical insert which was then inserted into the picks. The end of the cylindrical insert

was machined to have a minimal disturbance to the profile of the pick. A photograph of the instrumented pick is shown in Figure 3.4.

The thermocouple wires and WC plugs were pushed in a direction opposite to the cutting direction. The glue and the insulation around the thermocouple wires most likely melted due to the high frictional heat generated during the rock cutting. Thus the thermocouple wires would be forced into contact and hence form the hot junction required to make the temperature measurements at the cutting interface between the rock and the WC cutting element.

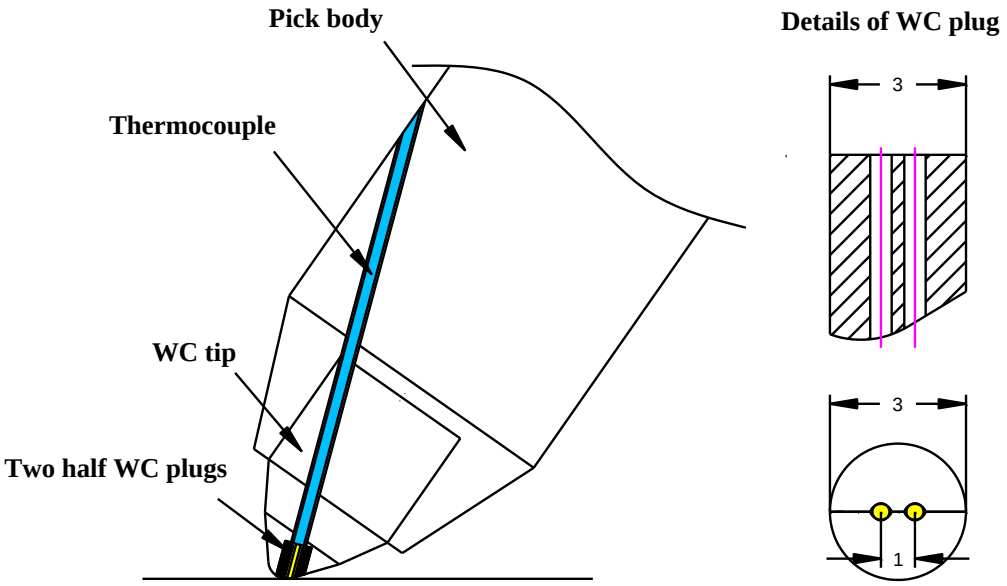

Figure 3.3 Configuration of thermocouple

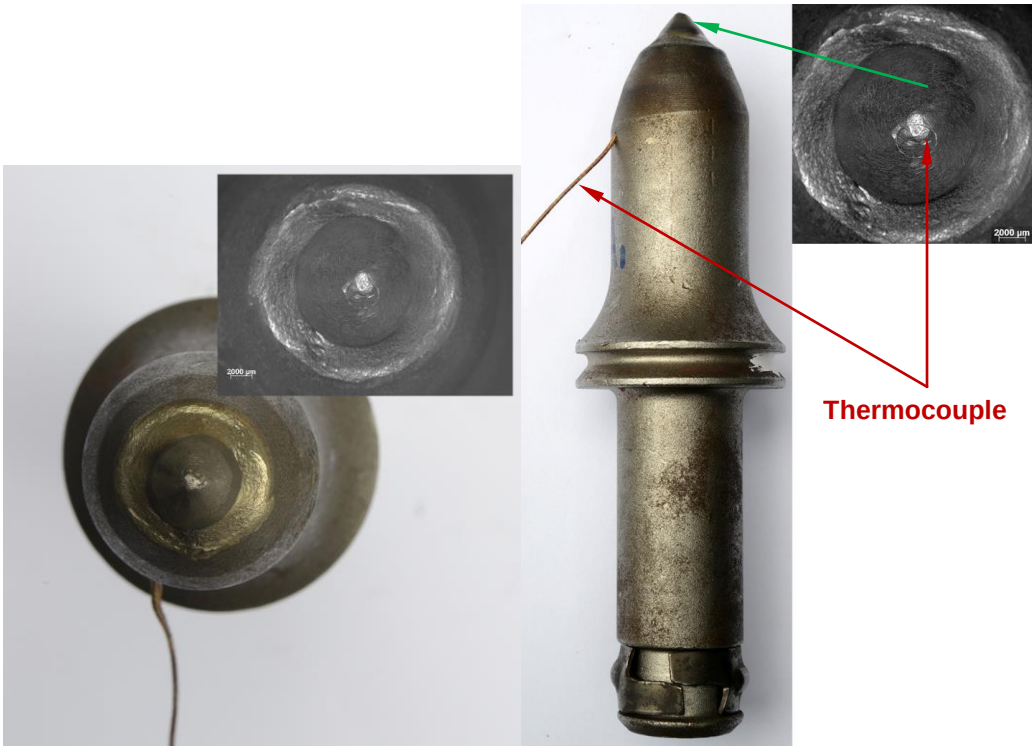

Figure 3.4 Instrumented WC pick

3.5 Infrared camera

Infra-red camera with high speed capture was also applied to measure the pick cutting temperature during the experimental runs. The thermal infrared camera used was FLIR SC7600M (Figure 3.5) and the recorded data were processed by the Altair Software. The camera is equipped with an InSb sensor which has 1.5 to 5.1 μm band pass arranged on 640×512 pixel array. A 50 mm lens was used and the infrared camera was positioned at a working distance of 71 cm. The integration (exposure) time was set up at 1 ms in order to grab the peak of the cutting temperature. Thermal resolution of this camera can be as high as 20 mK.

Figure 3.5 Set-up of infrared camera

3.6 Data acquisition and analysis system

A strain amplifier, a National Instruments (NI) PCI-6259 data acquisition (DAQ) board, a NI SCXI 1314 and a NI SCXI 1303 terminal block, a NI SCXI 1102 analog input module, a NI 9232 dynamic signal acquisition module, a NI SCXI 1000 chassis, a NI Compact DAQ Ethernet chassis, a Dell personal computer and software – LabVIEW 2013 for windows were involved in the data acquisition system. Eight channels were used to record the following parameters during an experimental run: three force components, three acceleration signals, table position of the planer and temperature signal from the K type chromel-alumel thermocouple. A data acquisition rate of 3200 readings per second per channel was used. The data were analysed by using MATLAB.

The three force signals from the dynamometer were amplified by a strain gauge amplifier system. The analogue signals from a displacement sensor, a dynamometer amplifier, three accelerometers and a thermocouple were transmitted into PC through NI data acquisition system after being converted to digital signals. Specific LabVIEW programs were developed for both control and data acquisition program. The cutting speed, sampling rate and table position can be easily controlled by this program. The system was able to handle large volumes of data rapidly and efficiently. The data acquisition and analysis system are shown schematically in Figure 3.6.

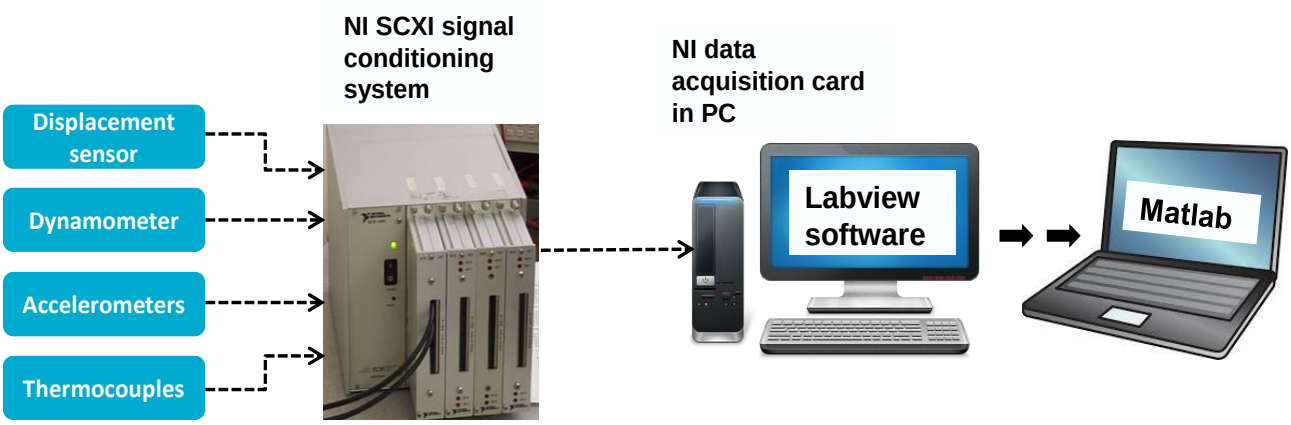

Figure 3.6 Data acquisition and analysis system

3.7 Rock chip size distribution analysis

Rock chip size is an important parameter to determine the rock cutting efficiency in rock cutting. The rock debris and chips were carefully collected in rock cutting experiments. The measured rock chip mass can be used to calculate the chip size distribution, specific energy and yield of rock fragmentation. According to Roxborough and Rispin [48], Coarseness Index (CI) which is defined as the sum of the cumulative weight percentages of rock debris retained in each sieve is a convenient technique for analysing the debris size.

As shown in Figure 3.7, five classes of sieves with different mesh sizes have been used in this study: 22.4 mm, 16mm, 8 mm, 4 mm and 1 mm. After each test, the collected rock chips were passed through these sieves and assembled into six size classes, the mass retained in each sieve was measured and the cumulative percentage mass retained from coarsest to finest mesh was obtained. The summation of the cumulative percentage values represented the Coarseness Index of the rock chips.

Figure 3.7 Sieves used for the rock chip analysis

3.8 Cutting tool

Two types of picks were used in these experiments; (a) TSDC tipped SMART*CUT picks and (b) WC point attack picks.

Figure 3.8 shows the TSDC tipped picks developed by CSIRO, used as the cutting tool in the first experimental program. A series of linear rock cutting tests was implemented to optimise the rock cutting process and develop force prediction algorithms for TSDC tipped picks. The two key elements of SMART*CUT technology are replacing conventional tungsten carbide with thermally stable diamond composite (TSDC) as the cutting tip of the tool and using CSIRO worldwide patented bonding technology to attach the TSDC tip to the steel tool body. These picks had a gauge of 70 mm, flange diameter of 50 mm, shank diameter of 30 mm and tip diameter of 16 mm.

WC picks instrumented with thermocouples (Figure 3.4) were used in the second experimental program to investigate the influence of different cutting variables on pick cutting temperature. The WC picks with the similar geometry to TSDC tipped picks were manufactured by Sandvik. It also had a gauge of 70 mm, flange diameter of 51 mm, shank diameter of 30 mm, tip diameter of 16 mm and primary tip angle of 78^{o}.

Five tool holders were designed and manufactured to vary the attack angle of cutting picks from 45^{o} to 70^{o} (Figure 3.9). The cutting tool was attached to dynamometer through one of these tool holders to achieve the attack angle specified.

Figure 3.8 TSDC tipped SMART*CUT picks

Figure 3.9 Tool holders with different attack angles (45, 50, 55, 60 and 65 degree respectively)

3.9 Rock sample and its properties

The rock sample used for the experiments was Helidon sandstone with a moderate strength. It was collected from a quarry in Queensland, Australia. A number of core samples were prepared to measure the elastic properties, uniaxial compressive strength (UCS) and Brazilian tensile strength (BTS) of the rock.

3.9.1 Uniaxial compressive strength (UCS)

The UCS tests were carried out in accordance with the ISRM and ASTM standards. The core samples were cut and ground with a length to diameter ratio of 2.5. Both the bottom and top ends of the core samples were examined for parallelism and assessed to ensure that they were perpendicular the core axis.

The tests were performed on an Instron's Series 1342 testing machine, which is a servo hydraulic controlled unit installed at the Rock Mechanics Laboratory of CSIRO (Figure 3.10). An add-on package, Precision Data Acquisition program with a LabVIEW interface platform, was used to record the loading data. The uniaxial compressive strength σ_c of the rock could be calculated by the following formula:

$$\sigma_c = \frac{4P_{\max}}{\pi D^2} \tag{3.1}$$

where $P_{\max}$ is the maximum load recorded and D is the diameter of the core sample.

Figure 3.10 Experimental set-up for UCS tests

Four core samples were prepared for the UCS tests and the results were shown in Table 3.2. As can be seen from Figure 3.11, the UCS values of the collected rock samples were consistent with an average UCS of 57 MPa.

Table 3.2 UCS testing results of Helidon sandstone

Core No	Diameter (mm)	Length (mm)	Maximum Load (kN)	UCS (MPa)
1	58.51	154.1	155.4	57.8
2	58.5	152.7	155.2	57.8
3	58.46	152.8	145.6	54.3
4	58.45	153.3	154.5	57.6
Average				57
SD				1.7

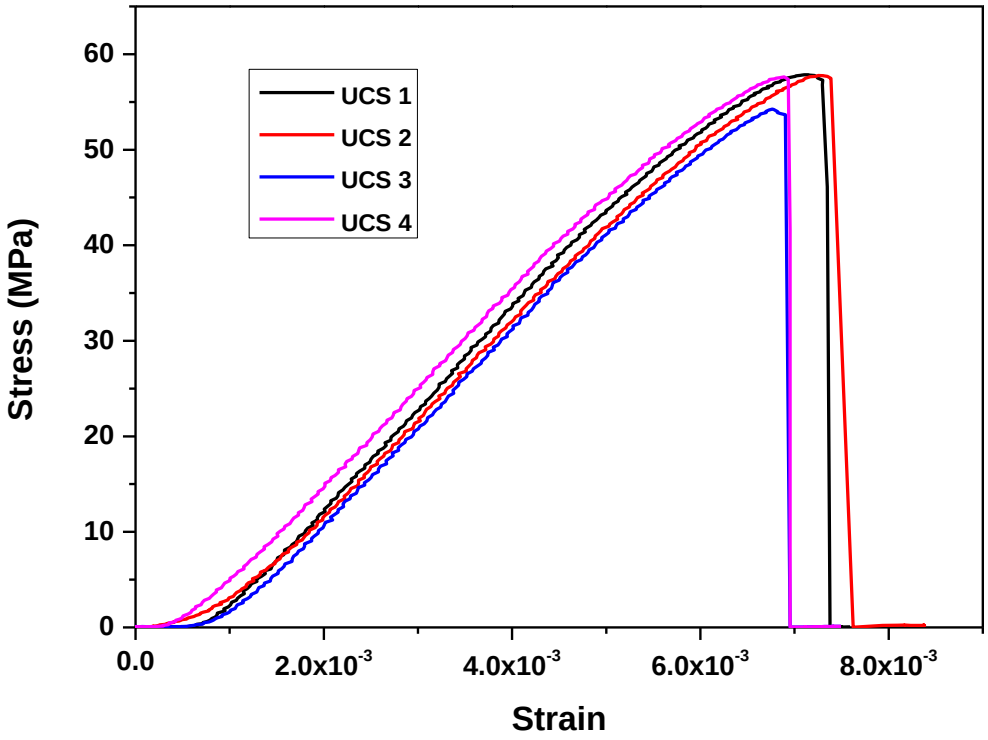

Figure 3.11 Stress-strain curves of the UCS tests of Helidon sandstone

3.9.2 Brazilian tensile strength (BTS)

BTS test, which is one of the most common used geotechnical testing methods, was used for indirect measurement of tensile strength of the target Helidon sandstone. Following the ASTM standard procedure, the core samples were prepared with an approximate 0.5 length to diameter ratio. BTS tests were also conducted on Instron's 1342 testing machine. Cylindrical rock specimen was placed between the loading platens and loaded continuously at a constant increasing rate until a diametrical split failure occurred. The tests details of the four rock specimens are shown in Figure 3.12. The BTS σ_t of the rock was then calculated as follows:

$$\sigma_t = \frac{2P_{\max}}{\pi DL} \tag{3.2}$$

where $P_{\max}$ is the applied load at failure, D *and* L are the diameter and length of the core sample.

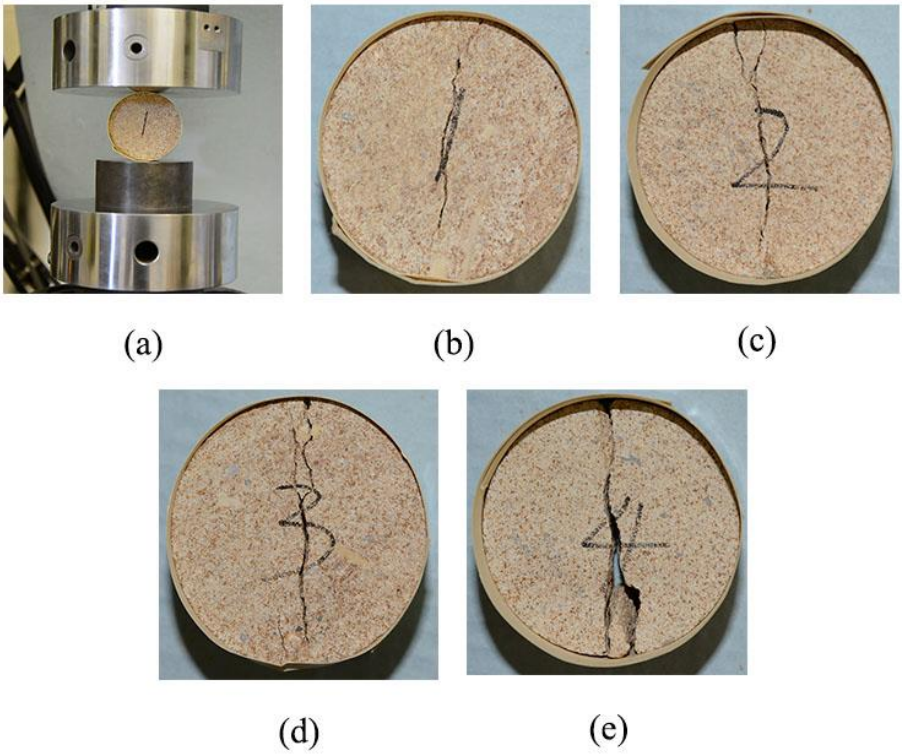

Figure 3.12 Set-up of BTS tests (a) and four rock specimens of Helidon sandstone after BTS tests (b-e)

BTS testing results of Helidon sandstone are given in Table 3.3. The average value of BTS is around 5.8 MPa

Table 3.3 BTS testing results of Helidon sandstone

Core No	Diameter (mm)	Length (mm)	l/d	Failure load (kN)	BTS (MPa)
1	58.5	29.8	0.5	16.4	6.00
2	58.4	29.9	0.5	16.3	5.95
3	58.5	29.4	0.5	15.3	5.66
4	58.5	29.4	0.5	15.5	5.74
Average					5.8
SD					0.14

3.9.3 Elastic properties and density

Determination of elastic properties of Helidon sandstone was carried out on Instron's Series 1342 testing machine as well. The rock core samples were prepared to satisfy the recommendation of ISRM and ASTM standards. Each core had a diameter of 58.5 mm and a length to diameter ratio around 2.5. Linear Variable Differential Transformer (LVDT) transducers were used to measure the axial and radial displacement (Figure 3.13). The analogue voltage outputs from the LVDTS were recorded and converted to corresponding displacements or strains, allowing the determination of Young's modulus and Poisson's ratio of the rock sample. Figure 3.14 shows typical stress-strain curves for the elastic properties tests.

The same trimmed core samples were also used to determine the density of the rock. The volume of each core can be calculated from the length and diameter measurements of the sample, the weight of each core was determined using a digital balance. Hence the density of each sample was determined from the ratio of specimen mass to specimen volume.

The elastic properties and density of Helidon sandstone are given in Table 3.4.

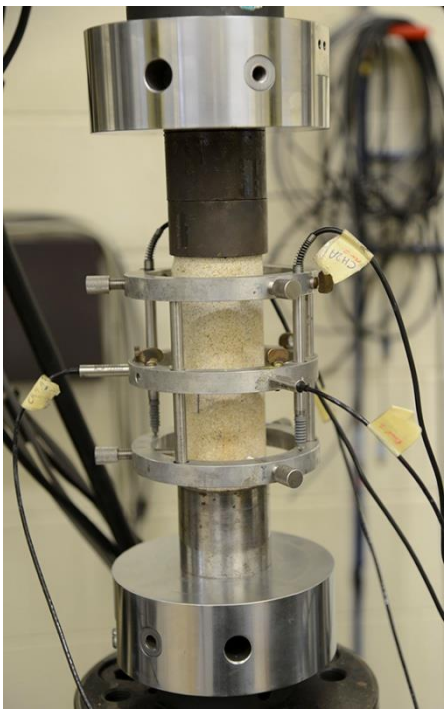

Figure 3.13 Experimental set-up for elastic properties measurement

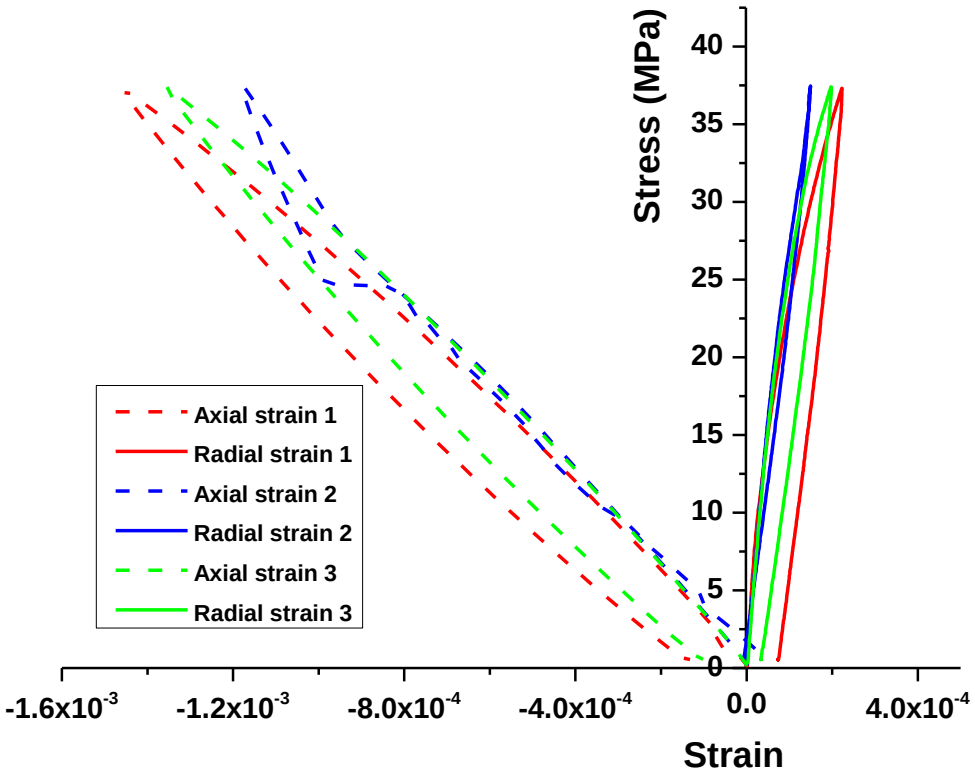

Figure 3.14 Typical stress-strain curves of the three core samples investigated

Table 3.4 Elastic properties and density of the core samples

Core No	**Diameter (mm)**	**Length (mm)**	**Mass (g)**	**Density (g/cm^3)**	**Young's modulus (GPa)**	**Poisson's ratio**
1	58.5	152.7	933.9	2.28	24	0.16
2	58.46	152.8	932.9	2.27	25.8	0.14
3	58.45	153.3	936.6	2.28	26.8	0.14
Average				2.28	25.5	0.15
SD				0.01	1.4	0.012

4

Rock cutting force estimation of TSDC tipped picks

4.1 Introduction

As discussed and reviewed in the first two chapters, excessive abrasive wear of traditional refractory carbides, diamond impregnated metal matrix composites (DIMMC) or polycrystalline diamond compact (PDC) cutting elements has hindered the use of mechanical excavators as the temperature at the tool-rock interface could exceed 1300^{o}C when cutting hard rock [8, 15, 16]. Hence, by changing the binder material from metallic cobalt to ceramic-based silicon carbide (SiC) during the sintering process, CSIRO has explored a new diamond composite called thermally stable diamond composite (TSDC). The use of SiC as the binder material is beneficial to the mechanical stability of TSDC at high temperatures as it does not act as a catalyst for the decomposition of diamond to graphite even up to a high temperature of 1350^{o}C. CSIRO developed the SMART*CUT (Super Material Abrasive Resistance Tool) rock cutting pick that has a TSDC cutting element bonded into the steel body of the pick using CSIRO's worldwide patented bonding technology. The successful development of the SMART*CUT technology, indicates a great promise for the employment of these cutting tools in hard rock mines. The main advantages of TSDC - tipped SMART*CUT picks are (a) good thermal stability, (b) high wear resistance and (c) the ability to mine harder deposits compared with point attack picks using tungsten carbide (WC) inserts [13, 16, 142, 143]. The previous research at CSIRO focused on the investigation of the wear characteristics of the solid, moulded TSDC cutting elements [15-17, 144]. It is evident that the wear resistance of TSDC elements was over one thousand times greater than that of cemented WC [16]. However, like other high wear resistance materials, the fracture toughness of TSDC is much less than that of WC. Therefore, the SMART*CUT picks may not be applicable to the current cutterheads on mechanical mining machinery as they are all based on WC point attack picks that have different material properties and geometries compared with such parameters required for TSDC-based picks [16].

Before the employment of SMART*CUT picks on a rock excavation machine, it is important to estimate the magnitude of cutting forces applied to the picks under different cutting scenarios, in order to calculate the cutterhead torque and cutter motor power for any given set of geological formations, cutterhead design, and operational conditions of the machine [7, 39]. Full-scale laboratory rock cutting tests are the most accepted, reliable and precise method that is needed to determine the cutting forces acting on an individual pick; the forces measured in these tests can be used as direct input into cutterhead design software to determine the capability and efficiency of the selected cutterhead and excavation machines [2, 7, 41-43, 79, 85]. Moreover, excessive forces on the picks may result in premature fracture damage of the TSDC elements, damage the machine

components and exceed the machine's torque and thrust capacities [4]. Therefore, it is crucial to select the cutting parameters to minimise the cutting forces.

In this chapter, the Taguchi method is initially employed to find out the critical cutting parameters that influence the rock cutting process. Then, multiple linear regression and neural network techniques are adopted to develop empirical models of the cutting forces on SMART*CUT picks as a function of depth of cut (DOC), attack angle, spacing and cutting speed. The performances of these models are also discussed.

4.2 Experiment

4.2.1 Experiment setup

As illustrated in section 3.2, the rock cutting tests were conducted on the CSIRO's linear rock cutting planer. In these tests, a block of Helidon sandstone, collected from a local mining quarry near Brisbane Australia was used as the test sample. The properties of this rock are summarised in Table 4.1. The cutting tools used in the experiment were TSDC tipped SMART*CUT picks (Figure 3.8). The cutting forces were recorded by a tri-axial dynamometer. In this study, only the orthogonal force components F_c and F_n (cutting and normal forces) were used for the cutting performance analyses because the magnitude of the sideway force F_s was normally negligible compared to that of cutting and normal forces (Figure 4.1).

Table 4.1 Properties of the Helidon sandstone

Density (g/cm^3)	Uniaxial compressive strength (MPa)	Brazilian tensile strength (MPa)	Young's modulus (GPa)	Poisson's ratio
2.28	57	5.8	25.5	0.15

Compared with WC, TSDC has higher wear resistance. On the other hand, it has lower fracture toughness. This means that SMART*CUT picks lack capability of bearing high bending forces. Therefore, the bending force F_b which is perpendicular to the pick axis (Figure 4.1) is another key factor affecting the cutting performance of SMART*CUT picks. In this study, the bending force F_b was also selected as a response parameter. It was calculated from the cutting force, normal force and attack angle θ_a , written as:

$$F_b = \left| F_c \sin\theta_a - F_n \cos\theta_a \right| \tag{4.1}$$

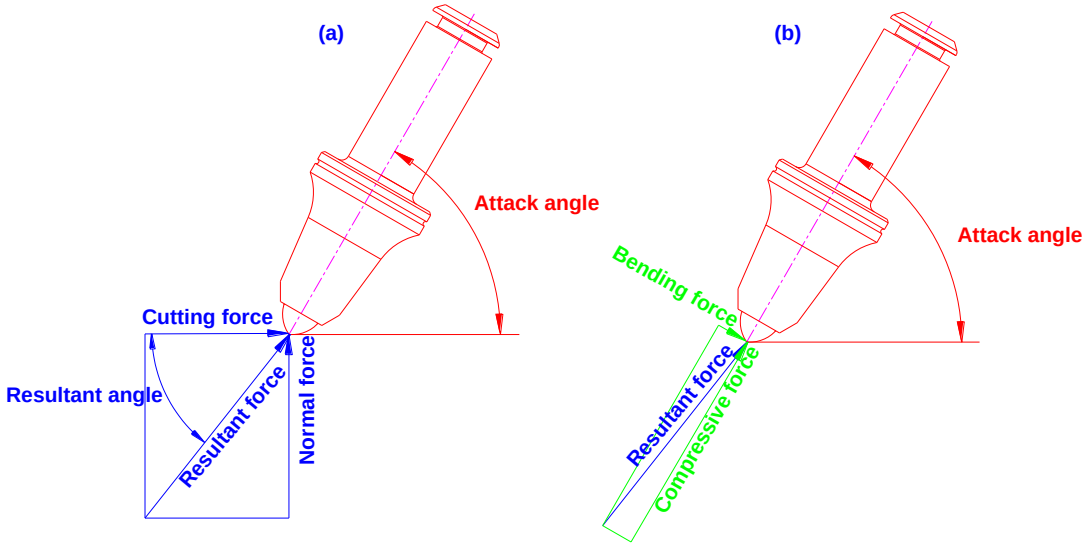

Figure 4.1 Illustration of forces on the pick

4.2.2 Experimental procedure

The following procedures were executed for all the tests:

(1) Trim and clean the rock surface before the cutting of each layer

(2) Change to the required tool holder and pick, and install spring washers

(3) Set depth of cut and line spacing, lock the cross head and bridge nuts

(4) Enter the following information and control parameters into the LabVIEW program

- Data sampling rate
- Cutting speed
- Filename information
- The channels being recorded

(5) Run the cutting test until the table reaches the end of its run, and store the data with specified file name on the computer's hard disk

(6) Collect the chips generated, take two images to record the rock surface information, and record any significant observations

It is to be noted that the boundary cuts which were close to the edge of the rock should be eliminated from the analysis as these tests may give unreliable forces and rock volume values. The maximum cutting forces should not exceed the capacity of the dynamometer.

4.2.3 Experimental design using Taguchi method

The Taguchi method is a popular and efficient experimental design technique for investigating how different parameters affect the mean and variance of a process performance characteristic. The approach can optimise performance characteristics by optimising the settings of design parameters and reduce the sensitivity of system performance to environmental conditions and variations [145]. The Taguchi method overcomes the limitation of full factorial design which has to test all the possible combinations of a process. A set of well-balanced experiments is organized by the manipulation of orthogonal arrays (OA), which allows the necessary data to be collected with a minimum amount of experimentation [146].

In the present study, the main cutting parameters, DOC, attack angle, spacing and cutting speed were selected as the input variables. A 5-level and 4-factor L25 OA was used to design the rock cutting experiments. The selected process parameters and their corresponding levels are shown in Table 4.2. The experimental layout for the cutting parameters using Taguchi's L25 orthogonal array is shown in Table 4.3. By the manipulation of Taguchi's orthogonal design matrix, the required tests reduced from 625 (5^4) to 25, which significantly reduced costs, time and efforts.

Table 4.2 Process parameters and their levels

Symbol	Parameters	Notation	Unit	Levels of factors				
				1	2	3	4	5
A	Attack angle	Θ_A	degree	45	50	55	60	65
B	Depth of cut	d	mm	6	9	12	15	18
C	Spacing	s	mm	24	36	48	60	72
D	Cutting speed	v	m/s	0.5	1	1.5	2	2.5

Table 4.3 Experimental design with Taguchi's L25 orthogonal array

Test No.	**A**	**B**	**C**	**D**
1	1	1	1	1
2	1	2	2	2
3	1	3	3	3
4	1	4	4	4
5	1	5	5	5
6	2	1	2	3
7	2	2	3	4
8	2	3	4	5
9	2	4	5	1
10	2	5	1	2
11	3	1	3	5
12	3	2	4	1
13	3	3	5	2
14	3	4	1	3
15	3	5	2	4
16	4	1	4	2
17	4	2	5	3
18	4	3	1	4
19	4	4	2	5
20	4	5	3	1
21	5	1	5	4
22	5	2	1	5
23	5	3	2	1
24	5	4	3	2
25	5	5	4	3

4.3 Experimental results and discussion

Mean cutting force (MCF), mean normal force (MNF) and bending force (F_b) were selected as the response factors for the cutting performance analysis. The results obtained from the rock cutting tests are shown in Table 4.4. In Taguchi method, the loss function which was further transformed into signal-to-noise (S/N) ratios is used to measure the quality characteristic deviating from the desired values [147]. There are three types of S/N ratio (η) characteristics to optimise the output responses: nominal-the-best (NTB), smaller-the-better (STB), and larger-the-better (LTB) [147]. The calculations of these S/N ratios are given in the following equations:

$$\eta_{NTB} = 10\log_{10}(\frac{\bar{y}^2}{S_y{}^2}) \tag{4.2}$$

$$\eta_{STB} = -10\log_{10}(\frac{1}{n}\sum_{i=1}^{n} y_i{}^2) \tag{4.3}$$

$$\eta_{LTB} = -10\log_{10}(\frac{1}{n}\sum_{i=1}^{n} \frac{1}{y_i{}^2}) \tag{4.4}$$

where η_{NTB}, η_{STB}, and η_{LTB} are the S/N ratios for the nominal-the-best , smaller-the-better , and larger-the-better cases, $\bar{y}$ the average value of the observed data, $S_y{}^2$ the variation of y , n the number of tests, and y_i the values of observed test results. Since lower values of mean cutting force, mean normal force and bending force are desirable in rock cutting process, the smaller-the-better S/N quality characteristic was chosen in this study. The S/N ratios calculated by Eq. (4.3) are also given in Table 4.4.

Table 4.4 Forces and corresponding S/N ratios

Exp No.	MCF		MNF		F_b	
	Result (kN)	S/N (dB)	Result (kN)	S/N (dB)	Result (kN)	S/N (dB)
1	2.66	-8.508	3.20	-10.105	0.38	8.401
2	4.58	-13.209	6.27	-15.944	1.20	-1.563
3	6.32	-16.020	9.69	-19.722	2.38	-7.520
4	8.88	-18.964	14.45	-23.196	3.94	-11.909
5	11.35	-21.098	19.09	-25.618	5.48	-14.773
6	3.41	-10.651	5.08	-14.121	0.66	3.667
7	5.70	-15.113	10.01	-20.009	2.07	-6.320
8	7.03	-16.939	12.58	-21.996	2.70	-8.639
9	7.20	-17.144	8.50	-18.588	0.83	1.637
10	5.76	-15.206	6.46	-16.201	0.26	11.693
11	3.05	-9.687	4.63	-13.321	0.16	15.922
12	3.36	-10.540	3.39	-10.603	0.81	1.806
13	5.25	-14.402	5.83	-15.310	0.96	0.377
14	4.78	-13.581	5.58	-14.935	0.71	2.964
15	7.12	-17.050	8.63	-18.721	0.88	1.087
16	2.20	-6.837	2.41	-7.643	0.70	3.130
17	3.59	-11.092	4.29	-12.641	0.96	0.331
18	3.47	-10.798	3.73	-11.424	1.14	-1.133
19	6.13	-15.747	7.20	-17.142	1.71	-4.657
20	6.31	-15.995	5.69	-15.109	2.61	-8.345
21	3.03	-9.617	3.56	-11.027	1.24	-1.854
22	3.51	-10.899	4.13	-12.326	1.43	-3.117
23	4.50	-13.061	3.96	-11.950	2.40	-7.618
24	7.47	-17.464	7.08	-16.999	3.78	-11.543
25	8.90	-18.989	8.40	-18.485	4.52	-13.098

4.3.1 Determination of optimal cutting conditions

The mean S/N ratios of each process factors at different experimental levels were obtained by averaging their S/N ratios at corresponding levels. For example, the mean S/N ratio for attack angle at level 1 was determined by averaging the S/N ratios for the tests 1-5 in Table 4.4. The mean S/N ratio for DOC at level 1 was calculated by averaging the S/N ratios for the tests 1, 6, 11, 16 and 21. The mean S/N ratios for other process factors at different levels were computed in the similar manner. All these mean S/N ratios produced the S/N responses, as shown in Table 4.5. Tables 4.5-4.7 show the S/N responses for mean cutting force, mean normal force and bending force respectively.

Table 4.5 S/N response table for mean cutting force

Symbol	Parameters	Mean S/N ratio (dB)					
		Level 1	Level 2	Level 3	Level 4	Level 5	Max-Min
A	Attack angle	-15.560	-15.011	-13.052	-12.094	-14.006	3.466
B	Depth of cut	-9.060	-12.171	-14.244	-16.580	-17.667	8.607
C	Spacing	-11.798	-13.944	-14.856	-14.453	-14.671	3.057
D	Cutting speed	-13.049	-13.424	-14.067	-14.308	-14.874	1.825

Table 4.6 S/N response table for mean normal force

Symbol	Parameters	Mean S/N ratio (dB)					
		Level 1	Level 2	Level 3	Level 4	Level 5	Max-Min
A	Attack angle	-18.92	-18.18	-14.58	-12.79	-14.16	6.13
B	Depth of cut	-11.24	-14.30	-16.08	-18.17	-18.83	7.58
C	Spacing	-13.00	-15.58	-17.03	-16.38	-16.64	4.03
D	Cutting speed	-13.27	-14.42	-15.98	-16.88	-18.08	4.80

Table 4.7 S/N response table for bending force

Symbol	Parameters	Mean S/N ratio (dB)					
		Level 1	Level 2	Level 3	Level 4	Level 5	Max-Min
A	Attack angle	-5.473	0.401	4.431	-2.135	-7.446	11.877
B	Depth of cut	5.853	-1.773	-4.907	-4.708	-4.687	10.760
C	Spacing	3.762	-1.817	-3.561	-5.742	-2.863	9.504
D	Cutting speed	-0.830	0.419	-2.731	-4.026	-3.053	4.445

The objective quality characteristic of this study was the-smaller-the-better, which means the smallest magnitude of the cutting forces would be the ideal situation. Thus, the optimal cutting condition of this study should be obtained with the maximum mean S/N ratio of each process factor according to the Taguchi method. The optimal level of each parameter with the highest S/N ratio was highlighted in red circles in the S/N response graphs (Figures 4.2-4.4).

The mean S/N ratio plot for mean cutting force is shown in Figure 4.2. As can be seen from Figure 4.2, the highest S/N ratio for mean cutting force was obtained at attack angle of 60^{o} (level 4), DOC of 6 mm (level 1), spacing of 24 mm (level 1), and cutting speed of 0.5 m/s (level 1). Hence, the optimal parametric combination for mean cutting force is A4B1C1D1.

Similarly, in Figure 4.3 the highest S/N ratio for mean normal force was also obtained at attack angle of 60^{o} (level 4), DOC of 6 mm (level 1), spacing of 24 mm (level 1), and cutting speed of 0.5 m/s (level 1). Therefore, A4B1C1D1 is also the optimal parametric combination for mean normal force. Again, in Figure 4.4 the S/N ratio for bending force was the highest at attack angle of 55^{o} (level 3), DOC 6 mm (level 1), spacing of 24 mm (level 1), and cutting speed of 1.0 m/s (level 2). Therefore, the optimal parametric combination for mean bending force is A3B1C1D2.

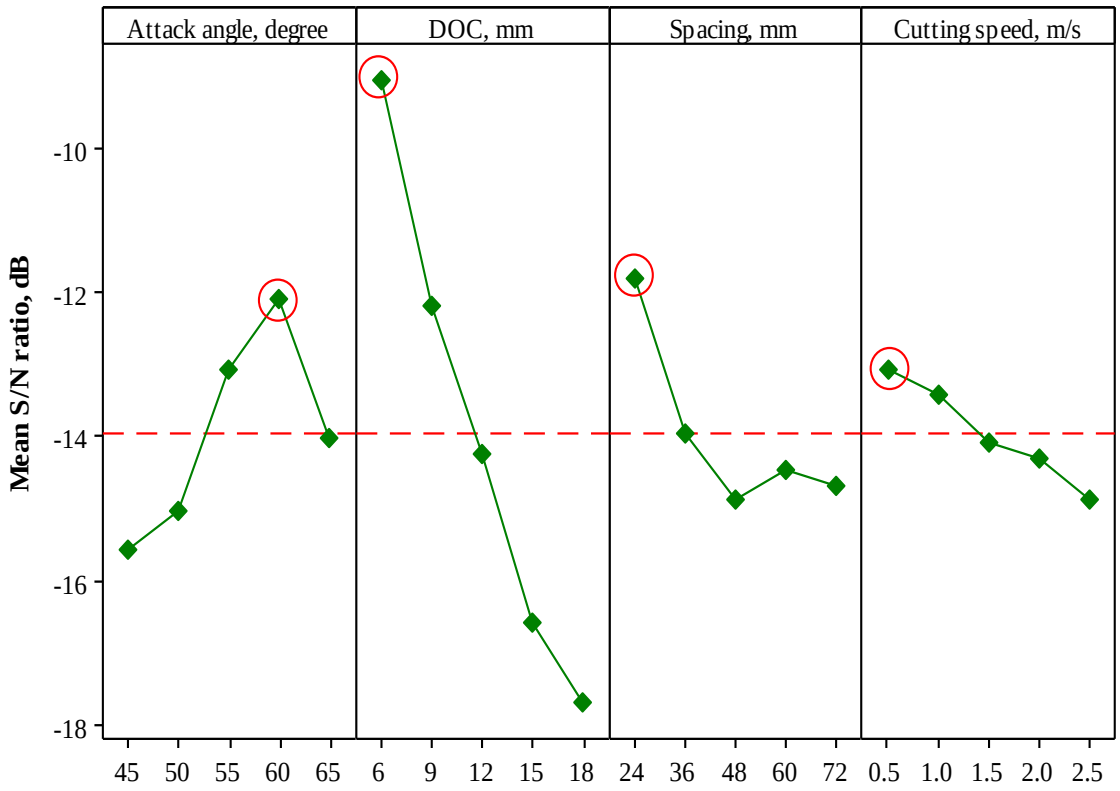

Figure 4.2 Mean S/N ratio graph for mean cutting force

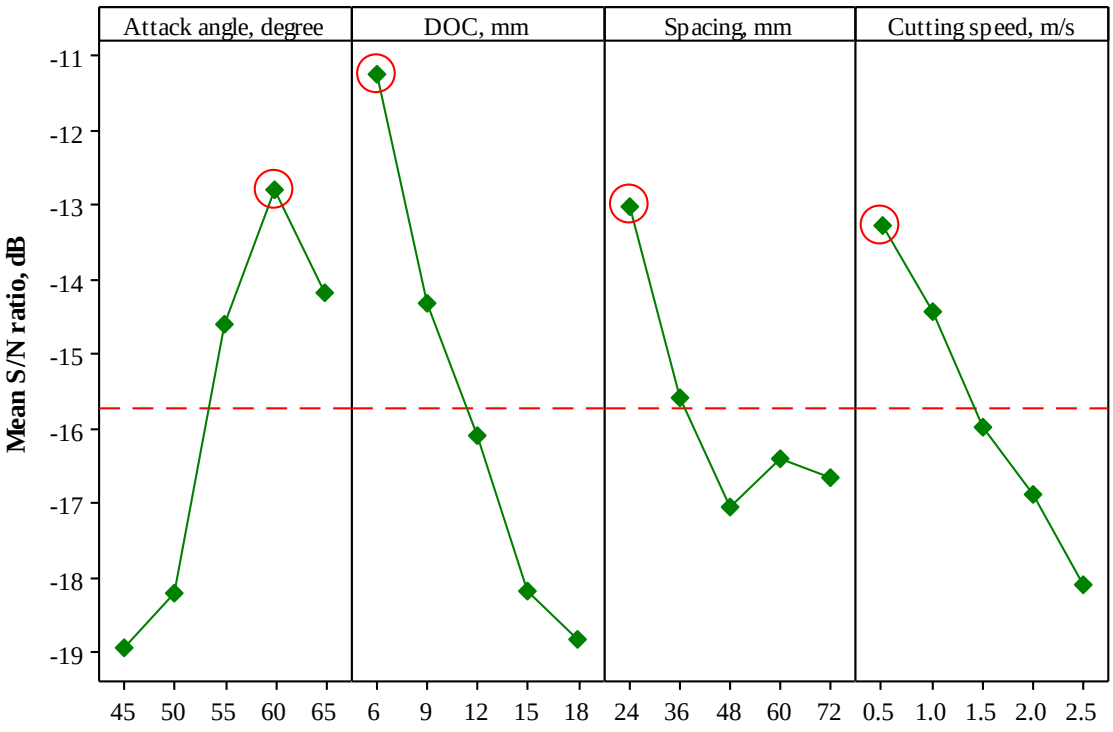

Figure 4.3 Mean S/N ratio graph for mean normal force

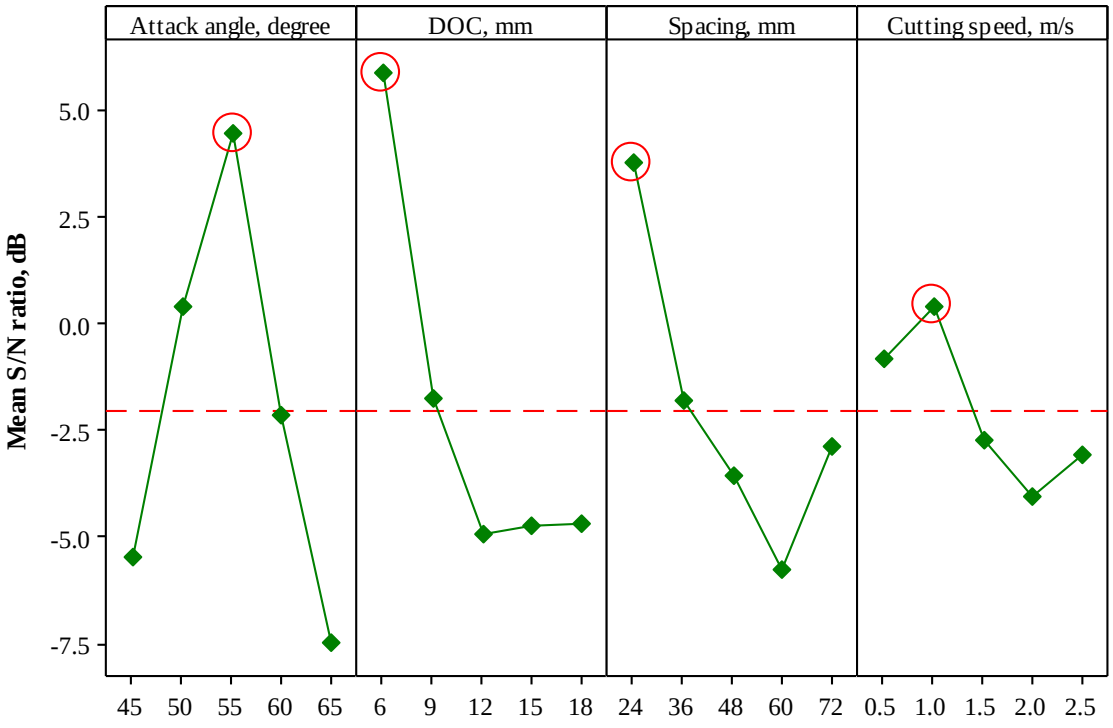

Figure 4.4 Mean S/N ratio graph for bending force

4.3.2 Analysis of variance （ANOVA）

ANOVA is an analysis tool used for studying the statistically significant parameters that influence the quality characteristic and identify the percent contribution ratio (PCR) of each process factors on output responses. The total variance of the response (i.e. the sum of squares of all the observation deviations from the grand mean) is decomposed into contributions related to each of the design parameter and the error [148]. Thus, the total sum of squared deviations SS_T can be written as:

$$SS_T = SS_d + SS_e \tag{4.5}$$

where

$$SS_T = \sum_{i=1}^{n} (\mu_i - \mu_m)^2 \tag{4.6}$$

Here, SS_d and SS_e are the sum of squared deviations due to each design parameters and errors respectively, n the number of experiments, μ_i the mean response for ith experiment and μ_m the overall mean of the response.

The PCR of each design parameter is equal to the sum of squared deviations due to each design parameters SS_d divided by the total sum of squared deviations SS_T . In the ANOVA table, the mean square deviation (MS) is computed by dividing the sum of squared deviations SS by the number of degrees of freedom associated with the design parameter or error. Then, F-value or Fisher's F ratio is simply the ratio of mean squared deviation (MS_d) due to each design parameters to the mean squared deviation due to error (MS_e).

P-value (probability of significance) is then determined from the F-value. If the P-value for a factor is equal to or smaller than the significance level 0.05 (confidence level 95%), it suggests that the contribution of the factor is significant.

The results of ANOVA for mean cutting force, mean normal force and bending force are presented in Tables 4.8-4.10 respectively. The PCR of each cutting parameter on these forces are shown in Figures 4.5-4.7. It can be found from Table 4.8 that attack angle, DOC and spacing are the statistically significant factors influencing the mean cutting force as the P-value of these factors are much less than 0.05. It is also observed from Table 4.8 and Figure 4.5 that the most influential factor for mean cutting force is DOC with a contribution percentage of 65.66%, followed by attack

angle and spacing which contribute 14.52% and 11.95% respectively. Cutting speed (4.77% contribution) has a relatively insignificant effect on mean cutting force.

Table 4.8 Results of ANOVA for mean cutting force

Factor	DF	Seq SS	Adj SS	Adj MS	F ratio	P	Contribution (%)
Attack angle	4	18.1226	18.1226	4.5306	9.36	0.004	14.52
Depth of cut	4	81.9198	81.9198	20.4799	42.32	0	65.66
Spacing	4	14.9080	14.9080	3.7270	7.7	0.008	11.95
Cutting speed	4	5.9498	5.9498	1.4874	3.07	0.083	4.77
Error	8	3.8717	3.8717	0.4840			3.10
Total	24	124.7718					100

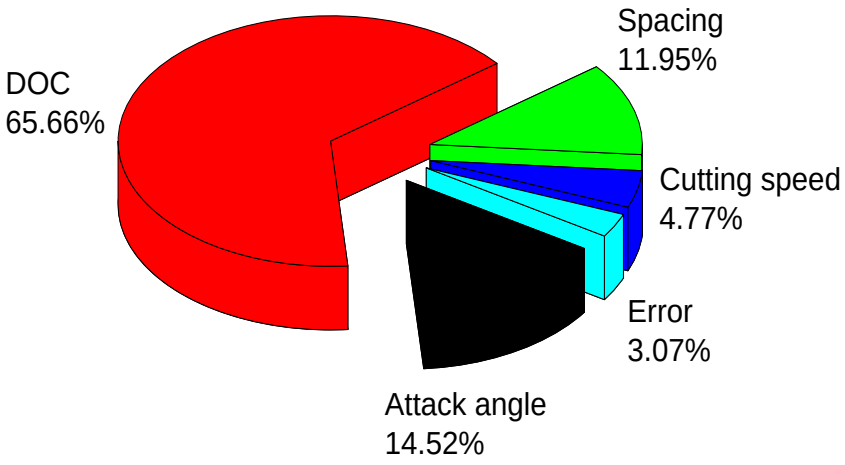

Figure 4.5 Contribution pie of mean cutting force

According to Table 4.9, attack angle, DOC, spacing and cutting speed all have statistical and physical significance on mean normal force. It is observed from Table 4.9 and Figure 4.6 that the most significant factor affecting mean normal force is attack angle (contribution 33.65% contribution), followed by DOC (29.86% contribution) and cutting speed (18.84% contribution), and then by spacing (13.01% contribution).

Table 4.9 Results of ANOVA for mean normal force

Factor	DF	Seq SS	Adj SS	Adj MS	F ratio	P	Contribution (%)
Attack angle	4	123.57	123.57	30.892	13.98	0.001	33.65
Depth of cut	4	108.98	108.98	27.245	12.33	0.002	29.68
Spacing	4	47.77	47.77	11.941	5.4	0.021	13.01
Cutting speed	4	69.19	69.19	17.297	7.83	0.007	18.84
Error	8	17.68	17.68	2.21			4.82
Total	24	367.18					100.00

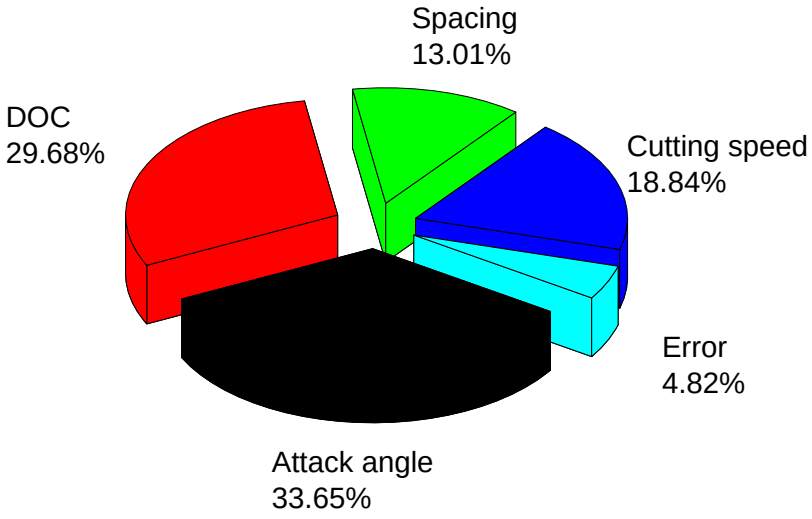

Figure 4.6 Contribution pie of mean normal force

From the analysis of bending force data (table 4.10) and Figure 4.7, only attack angle and DOC have statistical significance on bending force. Spacing and cutting speed are insignificant factors because the P-values of these factors exceed 0.05. The contribution order of the rock cutting process factors is attack angle, DOC, spacing and cutting speed, which affect the bending force by 32.47%, 28.18, 20.02 and 6% respectively.

Table 4.10 Results of ANOVA for bending force

Factor	DF	Seq SS	Adj SS	Adj MS	F ratio	P	Contribution (%)
Attack angle	4	15.525	15.525	3.8812	4.87	0.028	32.47
Depth of cut	4	13.476	13.476	3.3689	4.23	0.04	28.18
Spacing	4	9.571	9.571	2.3928	3	0.087	20.02
Cutting speed	4	2.868	2.868	0.7171	0.9	0.507	6.00
Error	8	6.378	6.378	0.7972			13.34
Total	24	47.818					100.00

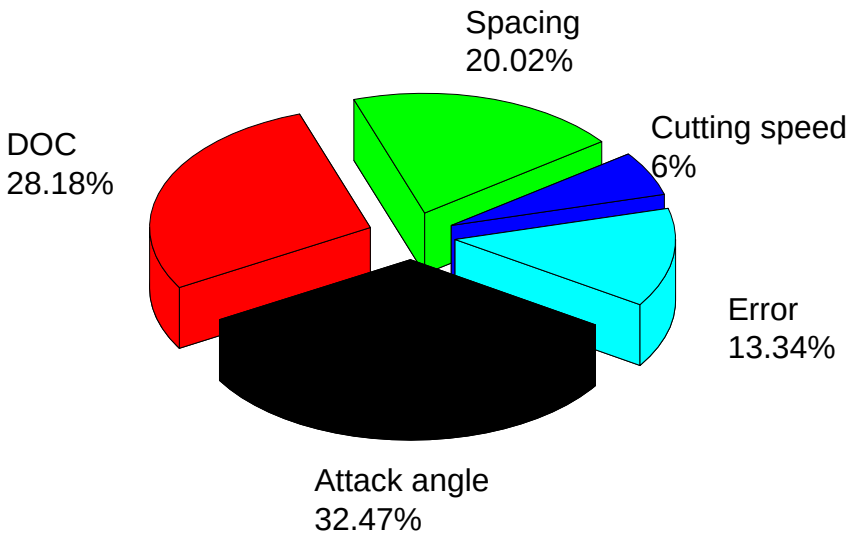

Figure 4.7 Contribution pie of bending force

4.3.3 Effect of cutting parameters on responses

The effects of the main cutting parameters on the values of mean cutting, normal and bending forces are shown in Figures 4.8-4.10. As shown in Figure 4.8, the mean cutting force decreases rapidly with the increasing attack angle, reaching a minimum value at an attack angle of 60^{o}, then mean cutting force starts to increase with a further increase of attack angle. While the increase in DOC, spacing and cutting speed, in general, leads to an increase in the magnitude of mean cutting force.

As shown in Figure 4.8, DOC causes a rapid increase in mean cutting force. There appears a linear relationship between DOC and mean cutting force. As expected, the mean cutting force increases with an increase in spacing. The dependence of the mean cutting force on spacing is obvious for an increase from 24 mm to 60 mm. For spacing greater than 60 mm, the mean cutting force tends to be constant. As the cutting speed increases, the mean cutting force also increases, but the rate of increase is not as high as with DOC.

Similarly, Figure 4.9 shows the influences of attack angle, DOC, spacing and cutting speed on mean normal force. It is seen that mean normal force also decreases rapidly when the attack angle increases from 45^{o} to 60^{o}. Beyond this point, any increase in the attack angle result in increases in mean normal force. The mean normal force increases linearly along with the increase of DOC as

observed in mean cutting force. This linearity is also supported by the previous studies by Bilgin [4], Roxborough [149] and Hurt and Laidlaw [11]. This has been attributed to the energy requires to fragment a brittle material is directly proportional to the amount of new surface area produced. When the DOC increases, larger chips or fragments are produced. So a higher energy consumption is required to generate the increase in the fracture surface, therefore resulting in higher cutter forces. The increment of spacing also causes an increase of mean normal force, but when spacing is larger, the mean normal force begins to level off as observed in mean cutting force, indicating the point at which interaction between adjacent cuts ceases and the cutting mode change from relieved cutting to unrelieved cutting condition. The mean cutting force is still found to increase with the increasing cutting speed.

Bending force is another significant factor determining the cuttability of SMART*CUT picks as the TSDC tip is a brittle material and has much lower fracture toughness compared with the WC insert. Figure 4.10 shows the main effects of operating cutting parameters on the mean value of the bending force. As shown in Figure 4.10 that there is a minimum in the bending force for an attack angle of 55^{o}. The increase of the DOC and cutting speed cause an increase in the bending force. It is observed that the bending force also increases with an increment of spacing from 24 mm to 60 mm.

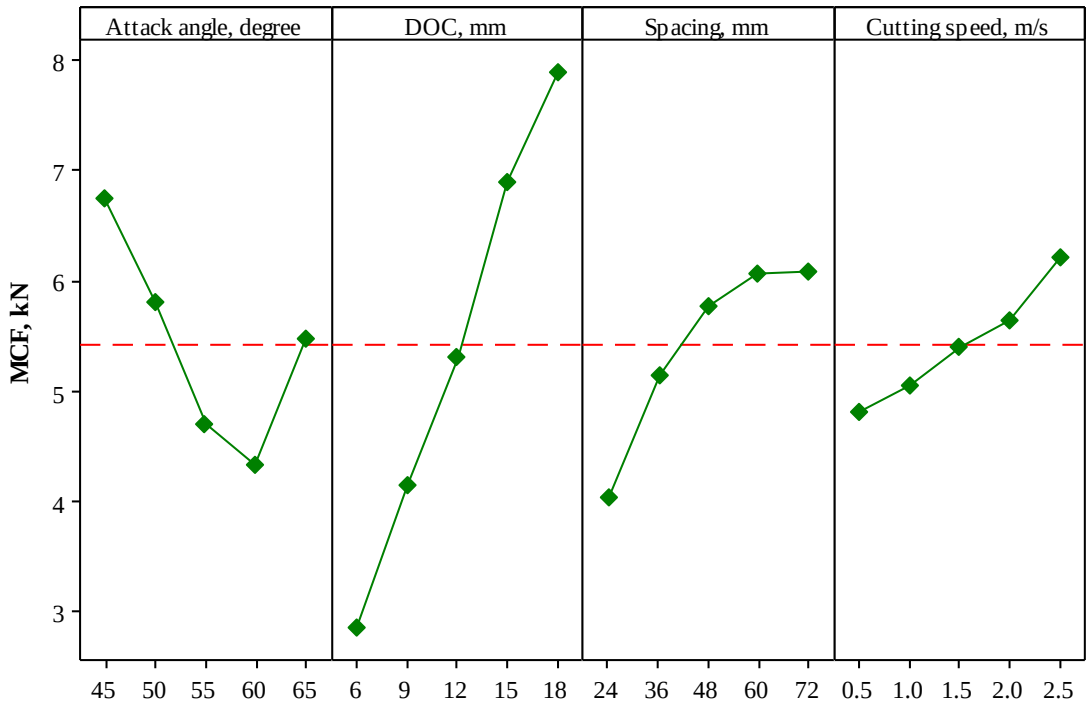

Figure 4.8 Mean effects plot for mean cutting force (red dashed line indicates mean value)

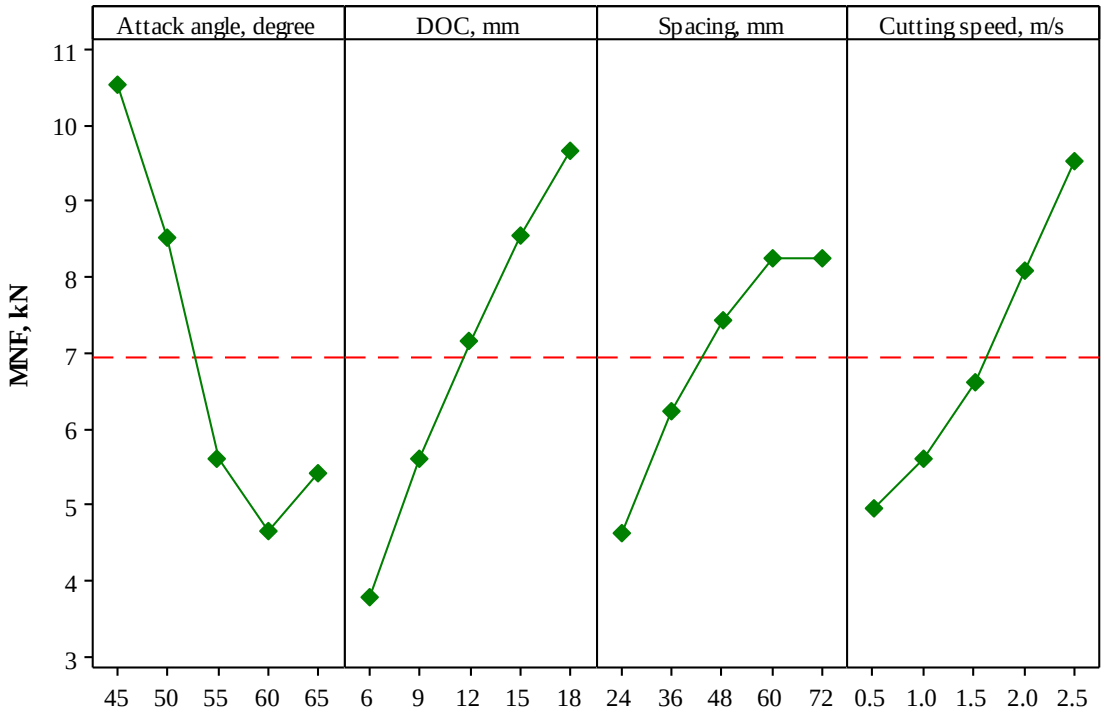

Figure 4.9 Mean effects plot for mean normal force (red dashed line indicates mean value)

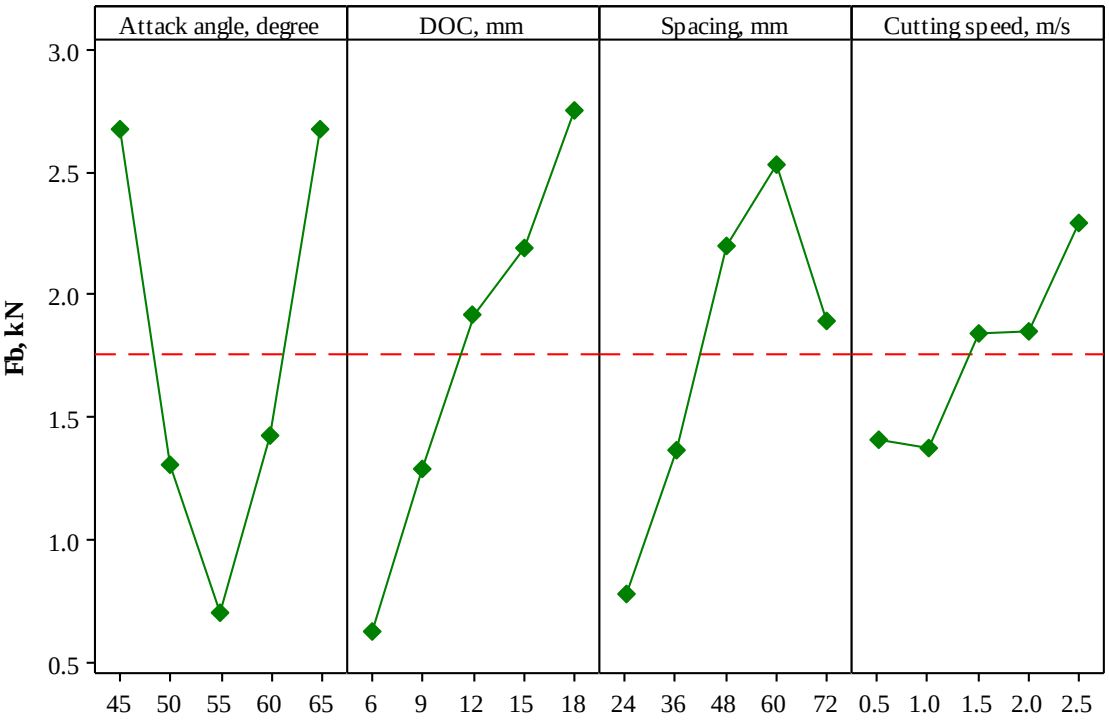

Figure 4.10 Mean effects plot for bending force (red dashed line indicates mean value)

4.4 Development of force estimation models

Statistical methods of multiple linear regression (MLR) and artificial neural network (ANN) which have been widely used for prediction and forecasting in mining and underground tunnelling engineering are applied to develop empirical models of mean cutting and normal forces on the TSDC tipped picks.

4.4.1 Multiple linear regressions (MLR)

Multiple linear regression (MLR) is a statistical analysis technique to predict the linear relationship between a dependent variable and two or more independent variables with a mathematic formula [7, 150]. This mathematical formula aims to fit a line to the data points with the minimum sum of squares of differences between observed and predicted values. Thus, the MLR model is sometimes also referred to as the least-squares model, which can be generally expressed as:

$$Y = \beta_0 + \beta_1 X_1 + \beta_2 X_2 + \cdots + \beta_n X_n + \varepsilon \tag{4.7}$$

where Y denotes dependent variable, $X_1, X_2, ..., X_n$ indicate independent variables, $\beta_0, \beta_1, ..., \beta_n$ represent the regression coefficients and ε is the error.

In multiple regression analysis, multicollinearity needs to be checked. It occurs when two or more independent variables in the MLR model are highly correlated. With multicollinearity, the standard errors of the affected coefficients tend to be large, thereby leading to an unreliable MLR analysis. Variance inflation factor (VIF) and Tolerance are common tools to detect the severity of a multicollinearity problem. Tolerance is the reciprocal number of VIF. Generally, if the VIF or Tolerance is equal to 1, there is no linear correlation between the independent variables. If the VIF is larger than 10 or Tolerance value is less than 0.1, serious multicollinearity problems exist in the regression model.

In this study, MLR models were developed to predict the relationship between dependent variables mean cutting force and mean normal force and the independent variables DOC, attack angle, spacing and cutting speed. The models for mean cutting force and mean normal force, i.e. Eqs. (4.8) and (4.9), were obtained using SPSS software.

$$MCF = 1.716 - 0.081\theta_a + 0.426d + 0.042s + 0.681v \quad (4.8)$$

$$MNF = 9.372 - 0.282\theta_a + 0.490d + 0.077s + 2.342v \quad (4.9)$$

where MCF and MNF are the mean cutting and normal force respectively, θ_a, d, s and v denote the attack angle, DOC, spacing and cutting speed respectively. The VIF values of the independent variables in these two models are all equal to 1, which means there is no multicollinearity problem in the models. Both coefficients of determination (R^2) of the models are 0.86, which indicates that 86% of the variance in MCF and MNF can be explained by the variables θ_a, d, s and v. The standard error of the estimate is the standard deviation of the errors of prediction. In these two models, the standard errors of estimate which show the standard deviation of the residuals are 0.91 and 1.57 respectively. The analysis of variance of the regression models for MCF and MNF gives p-values of 0.0000. This means the derived models are statistically significant.

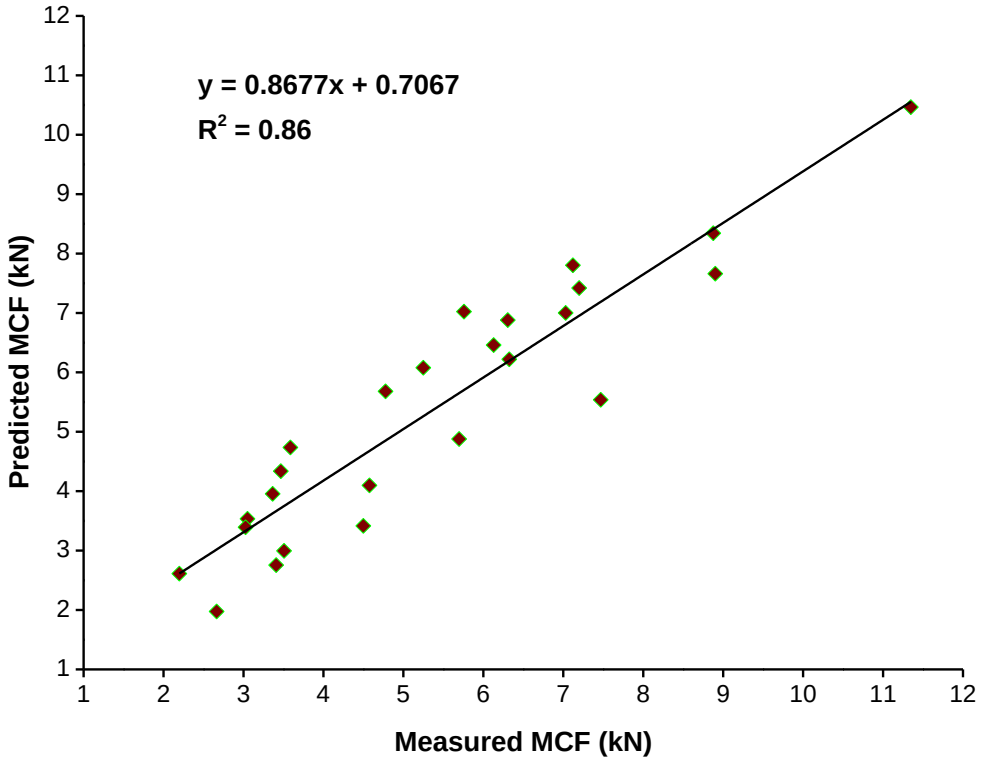

Figure 4.11 Relationship between the measured and predicted values of mean cutting force by MLR

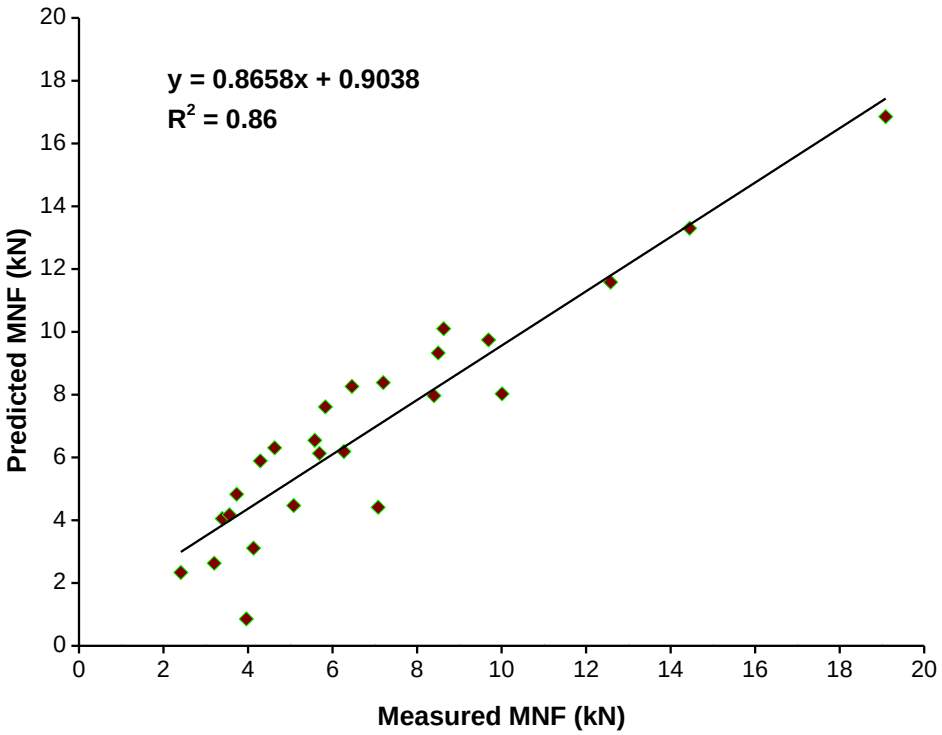

Figure 4.12 Relationship between the measured and predicted values of mean normal force by MLR

4.4.2 Artificial neural network (ANN)

ANN is a complex computational method inspired from biological neural network [151]. It has been widely used for predictive modelling and classification in many science and engineering problems, and should be a powerful tool for the analysis of cutting forces. In this work, a three-layer, feed forward back propagation network, the most commonly used neural network, was chosen as the prediction model for MCF or MNF. Figure 4.13 shows the schematic of this neural network. The independent cutting variables, including attack angle, DOC, spacing and cutting speed, were selected as the network inputs, the dependent variable MCF or MNF was considered as the output of the network. Eight neurons were included in the single hidden layer. A tangent sigmoid transfer function was used as the activation function in the single hidden layer. The general mathematical expression of the output of the network can be shown in the following equation:

$$Y = f\left(\sum_{j=1}^{m} v_j \left[\sum_{i=1}^{n} \varphi(w_{ij} X_i + \theta_j)\right] + \beta\right) \qquad (4.10)$$

Where Y is the output value of dependent variable predicted from input variables ($X_1, X_2, ..., X_n$), with X_i representing the input value of *ith* independent variable; w_{ij} is the weight factor between the *ith* input neuron and the *jth* hidden neuron; v_j is the weight factor between *jth* hidden neuron and

output neuron; θ_j and β are the biases of *jth* hidden and output neuron respectively; $f(.)$ and $\varphi(.)$ are the activation functions of output and hidden neurons respectively.

The input and output data in Tables 4.3 and 4.4 were used to train the neural network. 15% of the scaled experimental data was randomly selected as a validation set; another 15% of the data was defined as a test set and the rest (70% of the data) was classified as a training set. The Levenberg-Marquardt algorithm for back propagation, which is included in the MATLAB Neural Network Toolbox, was applied to build the ANN models. The training process proceeded in an iterative manner. Networks errors for the ANN model of MCF or MNF were monitored. In the optimisation procedure, the learning process was ceased when the validation error started to grow at a certain number of iterations. The best set of weights and biases were saved at the minimum validation error. It was observed during the training process that similar good performance was achieved for the test set error, and no significant over-fitting occurred. All three data sets were put through the network and linear regression was carried out between the network outputs and the measured MCF or MNF after unnormalising the network outputs. The coefficient of determination (R^2) of the ANN models for MCF and MNF are 0.97 and 0.98 respectively, indicating a very high percentage of the variance in MCF and MNF can be explained by the variables.

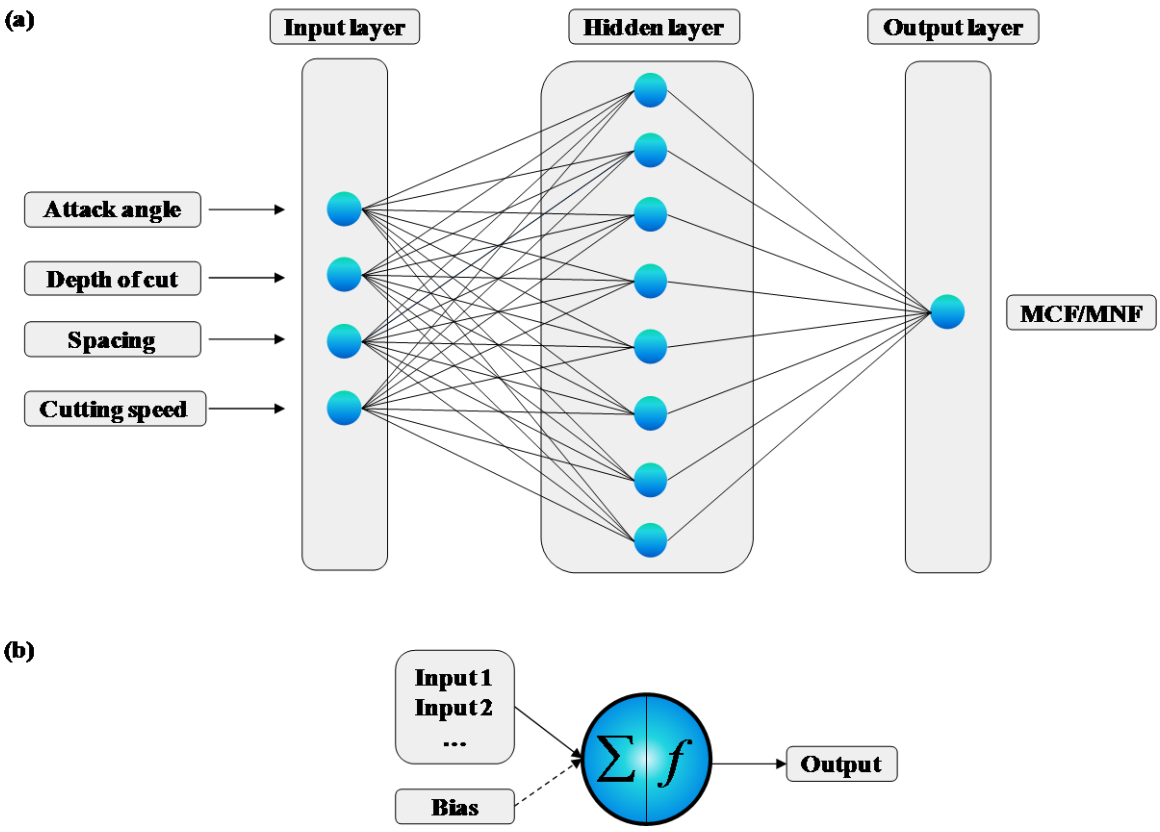

Figure 4.13 (a) The three-layer ANN used in this work (b) schematic of each neuron in the network

4.4.3 Comparison of the prediction models

The relationship between the measured and predicted values of mean cutting force obtained using the ANN model is shown in Figure 4.14. The determination coefficient (R^2) of the ANN model is 0.97, which means a consistent agreement exists between the measured and predicted values of mean cutting force. The comparison of measured and predicted mean cutting forces using both MLR and ANN is shown in Figure 4.15. It should be noted that the R^2 value of MLR model obtained is 0.86 (see Figure 4.11). It is clear from Figure 4.15 that the mean cutting force values calculated using the ANN prediction model are very close to the measured ones. But the MLR prediction values have a higher deviation from the experimental measurements.

Similarly, Figure 4.16 shows the relationship between the measured values and predicted values of mean normal force obtained from the ANN model. The R^2 value for the correlation in the prediction of mean normal force is 0.98, which has a higher degree of explanatory as compared to that of the MLR prediction model (0.86) as shown in Figure 4.12. The comparison of the measured and predicted mean normal force values obtained from the MLR and ANN models are presented in Figure 4.17. It is observed that the mean normal force values calculated using the ANN prediction model are in better agreement with the measured force values than those predicted by the MLR model.

These results indicate that both MLR and ANN methods can provide reasonably accurate predictions of mean cutting and mean normal forces; however, the ANN model is more accurate in predicting these forces using the stated rock cutting variables.

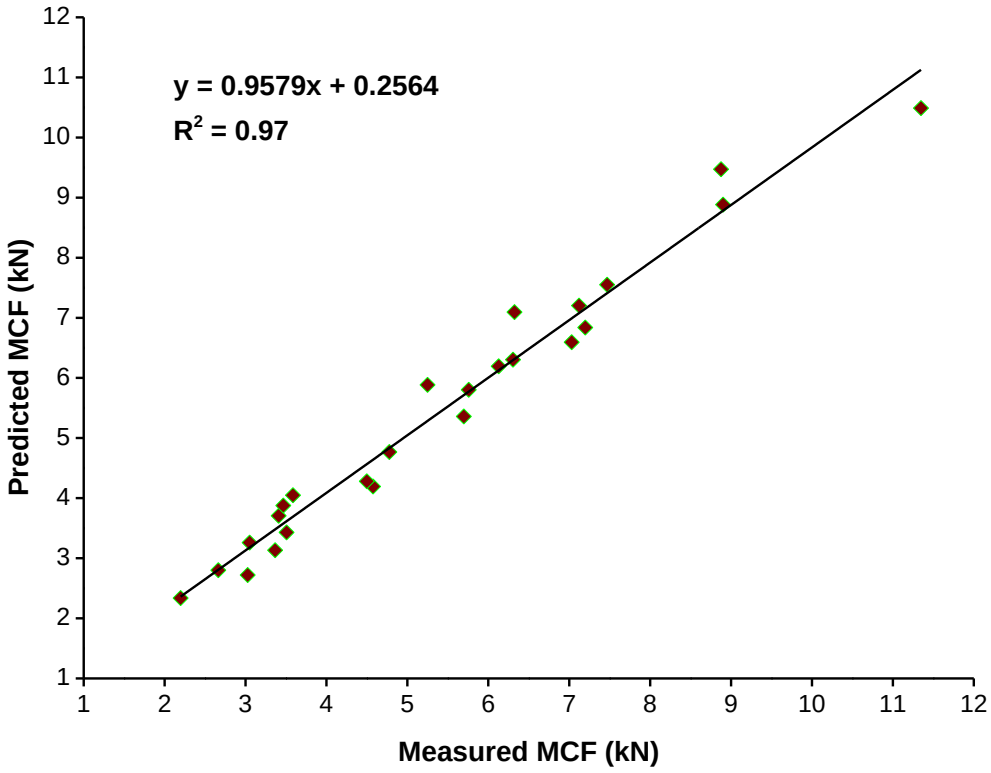

Figure 4.14 Relationship between measured and predicted values of mean cutting force by ANN

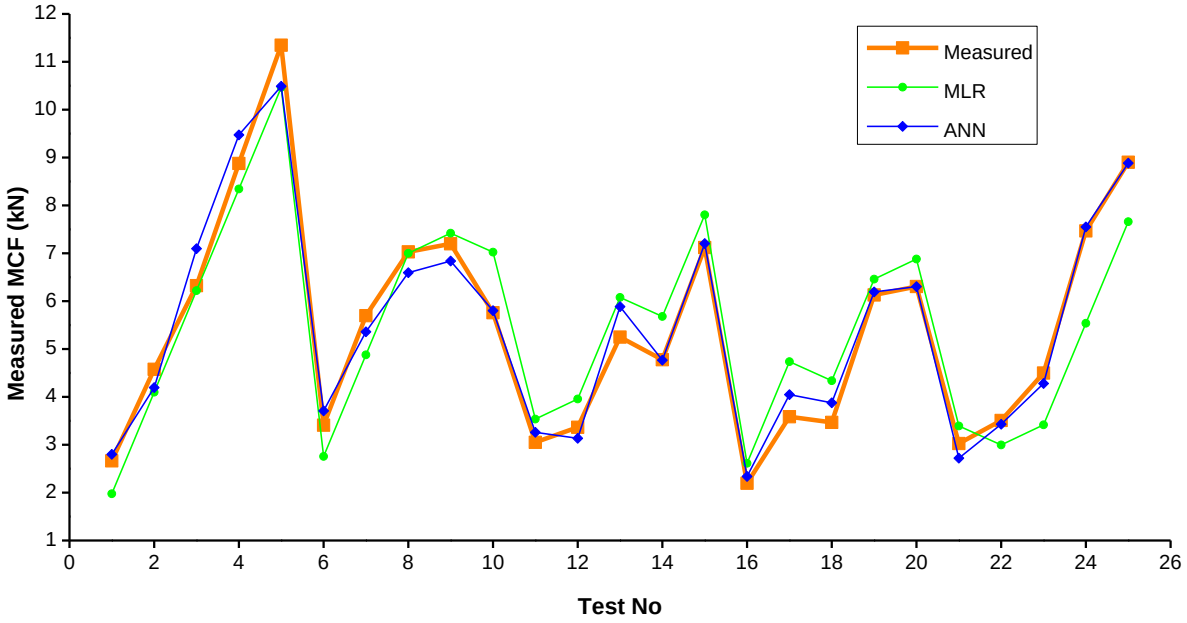

Figure 4.15 Comparison of measured and predicted mean cutting force of MLR and ANN

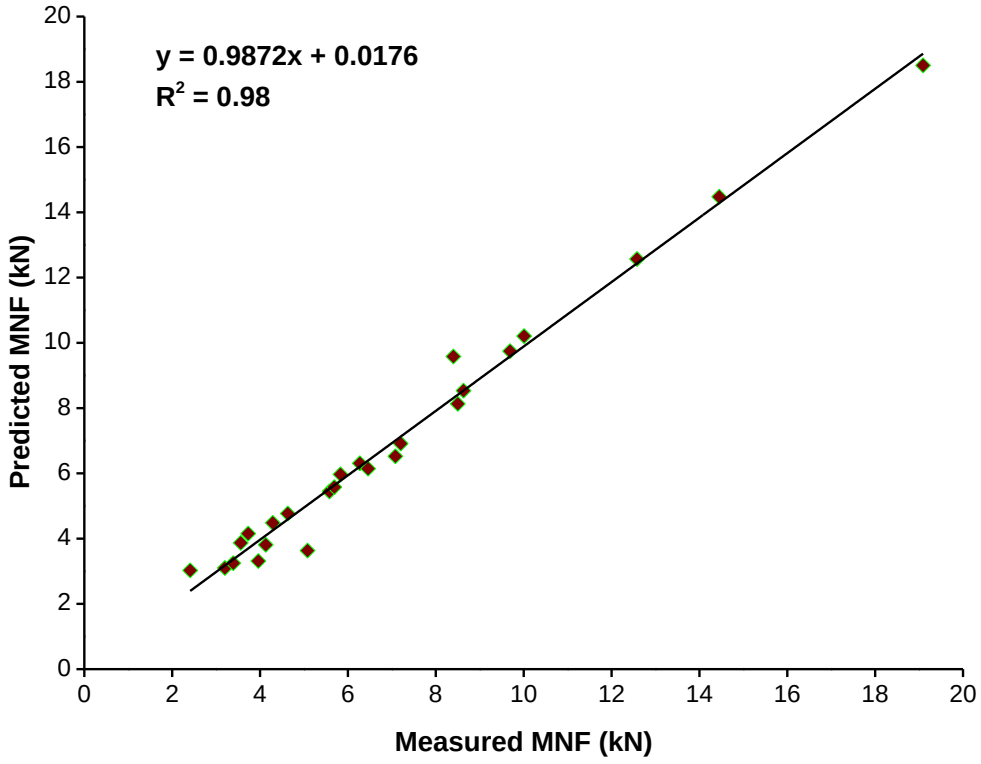

Figure 4.16 Relationship between measured and predicted values of mean normal force by ANN

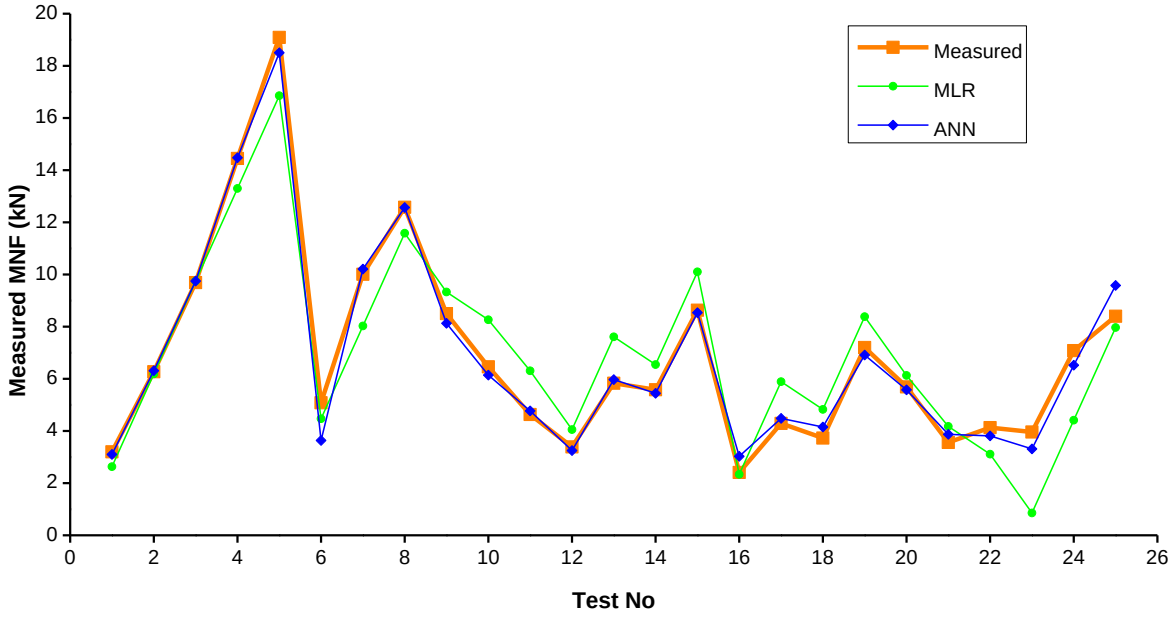

Figure 4.17 Comparison of measured and predicted mean normal force of MLR and ANN

4.5 Concluding remarks

The effects of attack angle, depth of cut, spacing and cutting speed on the cutting performance of TSDC tipped picks was systematically investigated. The tests were performed on the basics of Taguchi's L25 orthogonal array. The optimised rock cutting parameters for minimising the mean cutting, normal bending forces were obtained based on the mean S/N ratio. The optimal parametric combination for mean cutting and normal forces was: attack angle of 60^{o}, DOC of 6 mm, spacing of 24 mm, and cutting speed of 0.5 m/s, while for bending force the combination was attack angle of 55^{o}, DOC of 6 mm, spacing of 24 mm, and cutting speed of 1.0 m/s.

From the ANOVA analysis, it was found that attack angle, DOC and spacing were the statistically significant factors influencing the mean cutting force. The most influential factor was DOC, followed by attack angle and spacing. The cutting speed had the least effect. However, for the normal force, all four factors had statistical significance with a significance order of attack angle > DOC > cutting speed > spacing. Although the bending force is a function of the cutting and normal forces, the influences of the cutting parameters on it were different. Only attack angle and DOC had statistical significance, with an order of attack angle > DOC > spacing > cutting speed.

Empirical models for predicting the mean cutting and normal forces on TSDC tipped picks have been developed based on multiple linear regression (MLR) and artificial neural network (ANN) techniques. The established force models showed good predictive capabilities with acceptable accuracy. The ANN models offered better accuracy and less deviation than the MLR models.

5

Rock cutting temperature and thermal analysis

5.1 Introduction

The occurrence of frictional ignition of methane is a significant hazard in coal mining safety, and has resulted in a number of fatal mining incidents in Australia and overseas [91, 92]. Most cases of frictional ignition in Australia were caused by the striking of machine picks on a high silica material (conglomerate roof, sandstone roof or material associated with geological structures) in gassy conditions. According to the previous reports, cutter pick condition was the most important factor and acts as the trigger for nearly 70% of all frictional ignitions [92].

In order to assess the risk of frictional ignition for a pick striking of a rock stratum in a given condition, it is critical to determine the heat (or thermal energy) generated in the striking process. Although the heat cannot be measured directly, any thermal effects during rock cutting can be detected as changes in temperature at the rock-pick interface – referred as the 'hot spot'. It is suggested that the ignition potential is remarkably affected by the size and temperature of the hot spot [152]. Meanwhile, the occurrence of elevated interface temperature could arise from the considerable frictional heat or thermal energy generated between cutter picks and rock, which in turn, has a significant effect on the determination of the wear rate of the cutting tool [90, 93]. It is pointed out by many researchers that severe reduction in pick performance and significant thermal stress in rock as well as the tool could ultimately be caused by the elevated temperatures encountered in pick-rock interface [94-100]. Thus the determination of pick cutting temperature is extremely necessary as it will assist in assessing the performance and economics of drag bits and quantifying the risk of frictional ignition.

Some attempts have been made to study the problem of frictional heating in coal mining industry. A series of ignition tests were performed at the US Bureau of Mines. It was concluded that ignition events could be reduced by decreasing bit tip speed. It was further concluded that locked in picks are more liable to increase the incidence of frictional ignition (sometimes described as being more "incendive", than those that are free to rotate) [153].

Larson [154] found that frictional ignition was more prone to arise with worn point-attack picks. The risk in ignition for worn picks was 3 to 4 times greater than that for new picks at the same depth of cut. In 1993, Appl et al [113] conducted a series of cutting experiments on granite rock to determine the effects of cutting forces and interfacial temperatures on the life of PDC bits, which are the picks that have a thin layer of diamond (usually 1-2 mm thick) on a tungsten carbide base. It was concluded that the wear rate increased with increasing temperature and the critical temperature

for PDC bits was approximately 700 ^{o}C. A novel thermocouple configuration was developed by Cools [99] to measure the temperatures both inside and on the surface of the wear flat of a rock cutting chisel. He reported that temperatures of up to 550 ^{o}C and 800 ^{o}C were recorded when cutting a sandstone block and a limestone block. The temperature at a distance of 0.5 mm from the cutting interface was over three times lower than at the surface. Martin and Fowell [8] performed a series of rock cutting tests on rock planer to investigate the factors affecting the onset of severe drag tool wear in rock cutting. A K-type thermocouple was employed to detect the temperature close to the pick tip. A Calex Ranger infra-red gun was additionally used to monitor the tip temperature at the end of each cut. It was concluded that the heat developed during cutting is a determining factor accounting for severe tool wear. Materials that can maintain high values of indentation hardness at temperatures over 800 ^{o}C need to be exploited for cutting tools.

To data, a few of analytical studies have been proposed to predict the interface temperature during rock cutting [8, 90, 155, 156]. However, calculating the temperature from these solutions must inevitably suffer from the disadvantage of making major simplifications to the problem; such calculation may not be able to provide accurate predictions of the temperature because of the complicated real-life situation in rock cutting process.

Despite the efforts of these earlier studies, numerous difficulties and limitation still exist for the determination of pick cutting temperature during rock cutting process [114]. For instance, due to the different physical properties of the cutting tools and workpieces, tool-work thermocouple and metallographic techniques could not be used in rock cutting process. Temperature measurements through infrared methods are significantly affected by chip obstruction [102, 115].

In this chapter, a temperature measurement system will be developed to measure the interface temperature between a rock block and a pick tip. Firstly, a thermal infrared camera with high speed imaging rates will be used to acquire the temperature distribution in the cutting area. A comparison between the cutting performance of SMART*CUT and conventional WC picks in terms of temperature and forces is presented. Secondly, an embedded thermocouple technique is employed to investigate and analyse the influence of the typical cutting parameters on pick cutting temperature.

5.2 Temperature measurement methods

In a metal machining process, several measurement techniques were developed to measure the temperature at the tool-chip interface, including tool-work (dynamic) thermocouples, embedded thermocouples, single wire thermocouples, thin-film thermocouples, radiation pyrometers, infrared cameras. Those methods can be classified into direct conduction and indirect radiation. Among these methods, some can measure the temperature at a given point or the mean temperature over a certain area, while others can be used to investigate the temperature distribution near the cutting zone.

5.2.1 Thermocouple techniques

Thermocouple techniques are the most extensively used methods for temperature measurement in the metal machining process [157]. It is based on the fact that when two dissimilar metals or alloys are joined together to form hot and cold junctions, an electromotive force (emf) is generated if there is a temperature gradient between the two junctions. The tool-work (dynamic) thermocouple is a widely established method to investigate the tool-chip interface temperatures in cutting. In this thermocouple technique, the tool and the workpiece are used as the two elements of the thermocouple. The thermal emf is produced across the contact interface between the tool and workpiece. Leshock et al. [158] employed this technique to analysed the tool-chip interface temperature in turning of 4140 steel alloy and Inconel 718 with tungsten carbide tools. This technique was also used by Grzesik [159-162] to investigate the influence of different coatings on the cutting temperature. However, it can only provide an average value of temperature around the entire contact area between the tool and workpiece, and high local transient temperature cannot be captured [115]. A coolant cannot be used with this method. In addition, both the tool and workpiece should have a good electrical conductivity and need to be accurately calibrated, which makes this technique impossible to be applied in rock cutting.

Embedded thermocouple is another commonly used method to estimate the temperature involved in various machining processes. This method requires the drilling of a number of fine holes near the cutting edge in a cutting tool. The temperatures at multiple points can be measured by the thermocouples which are inserted into these holes. Korkut et al. [101] investigated the chip-back temperature in turning AISI 1117 steel with a K type thermocouple. It was observed that the temperature at the back rack surface increased with the increase of cutting speed, feed rate and depth of cut. The cutting temperatures of the orbital drilling and conventional drilling of aluminium,

CFRP (carbon fiber reinforced plastic) and titanium composites were measured by Brinksmeier et al. [163] using embedded thermocouples close to the tool tip. Their results showed that temperatures in orbital drilling were much lower than that in the conventional drilling of the three materials. The surface integrity at boreholes in these materials generated by the orbital drilling was also better than that observed in the conventional drilling. The difficulty of this technique is that it requires the drilling of fine holes as close as possible to the tool-chip contact surface, in many cases, in hard and difficult-to-machine materials such as tungsten carbide, ceramics and polycrystalline diamond composite.

The single-pole grindable thermocouple was developed by Rowe et al. [164] for measuring the temperature at the contact surface in surface grinding. In this approach, a single pole foil thermocouple assembly was housed in a pre-machined slot either in a grinding wheel or in a workpiece (usually in the workpiece as it is much simpler and less expensive). Batako et al. [103] compared different approaches of temperature measurement in High-Efficiency Deep Grinding (HEDG) and found that the single-pole grindable thermocouple technique was the simplest and most reliable technique. The thermocouple geometry was found to be a significant factor that affects the reliability of the signals under HEDG conditions. This method worked well for the grinding process. To apply this technique in rock cutting process, the rock specimen has to be split into pieces to mount the single pole foil thermocouple assembly. Only one brief temperature might be measured for only a very short time in one single pass of the pick. In addition, the shaking of the cutter during cutting would make the temperature even more difficult to be measured.

5.2.2 Radiation techniques

The radiation techniques, such as radiation pyrometers and infrared cameras, are non-invasive methods to determine the thermodynamic temperature of a body based on the thermal radiation it emits. The radiation technique offers many advantages such as non-intrusive measurement, fast response, no physical contact as well as being able to provide thermal fields compared to the thermo-electric technique. Lin et al. [165] installed several infrared (IR) pyrometers with fiber optic at the rake face near the cutting edge to detect the infrared radiation for both carbide and ceramic tools with cutting speed of 600 m/min. It was found that the heat dissipation at the cutting edge was significantly affected by the thermal properties of the tool material. Although the interface temperatures were similar, the input heat for the ceramic tool with high thermal resistance was much less than that of a carbide tool with low thermal resistance. Using a two-colour pyrometer with a fiber coupler, the tool frank temperature of a chamfered CBN cutting tool was measured by Ueda et al. [166]. Three high hardness steels were chosen as the work materials. The cutting speed

and hardness were found to be the significant factors influencing the cutting temperature. The highest temperature reached nearly 1000 ^{o}C when cutting AISI52100 at the cutting speed of 300 m/min. Infrared (IR) photographic technique was first exploited by Boothroyd [167] for determining the temperature distribution in the workpiece, chip and tool. Jeelani [168] used a more sensitive high speed IR film and more accurate calibrations to improve the earlier measurements of temperature distribution in machining an annealed 18% Ni maraging steel by IR photographic technique. Recent advances of high bandwidth solid-state detector arrays sensors in modern thermal imaging cameras have led to the proliferation of IR photographic techniques for the temperature measurement in high speed machining processes [169-172]. However, chip obstruction might be the main issue for radiation techniques as it significantly affects the measurement accuracy, especially when cutting some brittle materials such as rocks and ceramics.

A number of other methods have also been proposed to determine the temperature distribution at the tool-workpiece interface including micro thin film thermocouples (μ-TFTCs) [173], thermal paints [174], PVD (physically vapor deposited) films [175], and metallographic evaluations of the microstructural and microhardness changes [176]. However, these methods are tedious and difficult to be applied in rock cutting as the physical properties of the cutting tool and workpiece are totally different. Therefore, research involving the measurement of temperature in rock cutting processes still faces numerous difficulties and limitations.

5.3 Temperature measurement by infrared photographic technology

5.3.1 Experiment details

As shown in section 3.2, the linear rock cutting tests were also performed on the CSIRO's rock cutting planer. The temperature distribution in the cutting area was acquired using a thermal infrared camera FLIR SC7600M (Figure 5.1) and the recorded data were processed with the Altair Software. The camera was equipped with an InSb sensor with 1.5-5.1 μm band pass arranged on 640×512 pixel array.

The TSDC tipped SMART*CUT picks developed by CSIRO and the conventional WC pick with similar geometry (Figure 5.2) were used in these tests. The rock sample was the sandstone of high strength (unconfined compressive strength (UCS) = 120 MPa, Brazilian tensile strength = 7.8 MPa, Cerchar abrasivity index = 1.4). The constant conditions throughout the testing programme included the cutting speed of 3 m/s, and the skew and tilt angles of 0^{o}. The depth of cut and attack angle were

10 mm and 60^{o} respectively. Normal force, cutting force and lateral force were recorded during each cutting test.

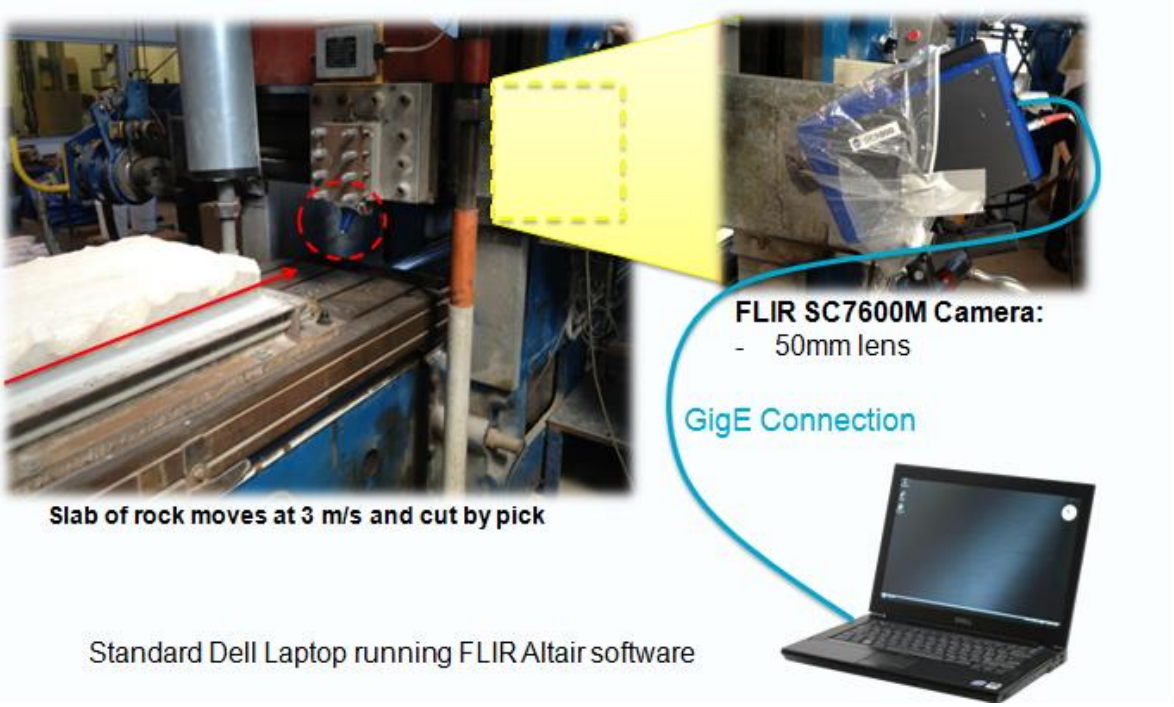

Figure 5.1 Temperature measurement by an infrared camera

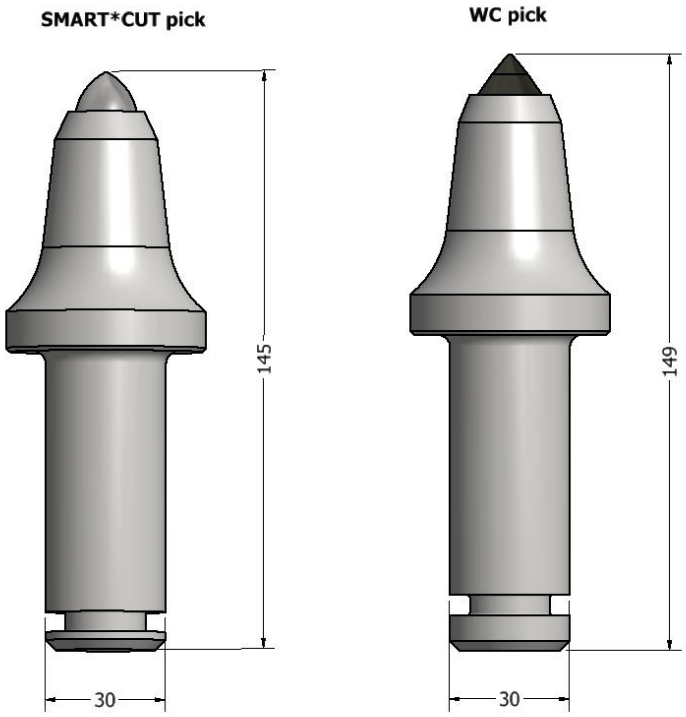

Figure 5.2 The TSDC tipped SMART*CUT and WC picks

A comparison of the cutting performance of TSDC tipped SMART*CUT and conventional WC picks in terms of temperature, cutting force, normal force and resultant angle in full-scale linear rock cutting tests is given in this section.

5.3.2 Results and discussion

5.3.2.1 Force

Cutter forces obtained with high reliability from the full-scale linear cutting tests are of vital importance to assess the cuttability of cutting tools and excavation machines. It is also an important indication of the temperature in the cutting zone. So in this study, the cutting forces were measured together with the temperature for comparison purpose. Due to the brittle nature of rock, wide fluctuations in cutter forces and discontinuous formation of cutting chips are always observed in rock cutting.

Resultant angle (θ) is another important factor determining the cutting performance of cutting tools. It can be calculated from cutting force (F_c) and normal force (F_n), which is defined as:

$$\theta = arc\tan(\frac{F_n}{F_c}) \qquad (5.1)$$

When the resultant angle is equal to the attack angle, the resultant force is aligned parallel to the axial direction of the pick, so the bending force on a cutting pick is minimised (Figure 4.1).

Figure 5.3 shows the cutting force, normal force and resultant angle history under the following cutting conditions: the depth of cut = 10 mm, the speed of cut = 3 m/s and the angle of attack = 60^o. The typical saw-tooth shapes of force-time diagrams can be seen in Figure 5.3. The average values of the forces, obtained from at least three repeated tests, give the mean cutting and mean normal forces.

Compared to the conventional tungsten carbide picks, which are conical, the SMART*CUT picks have a bullet shape. It can be seen from Figures 5.3 and 5.4 that the cutting and normal forces for the SMART*CUT picks are 7.0% and 4.6% smaller than the respective forces for the conventional WC picks.

It can also be seen from Figures 5.3c and 5.4 that the resultant angle for the SMART*CUT picks is slightly greater than that for the WC picks, suggesting that a greater attack angle should be employed for SMART*CUT picks to minimise the bending force on the TSDC tips.

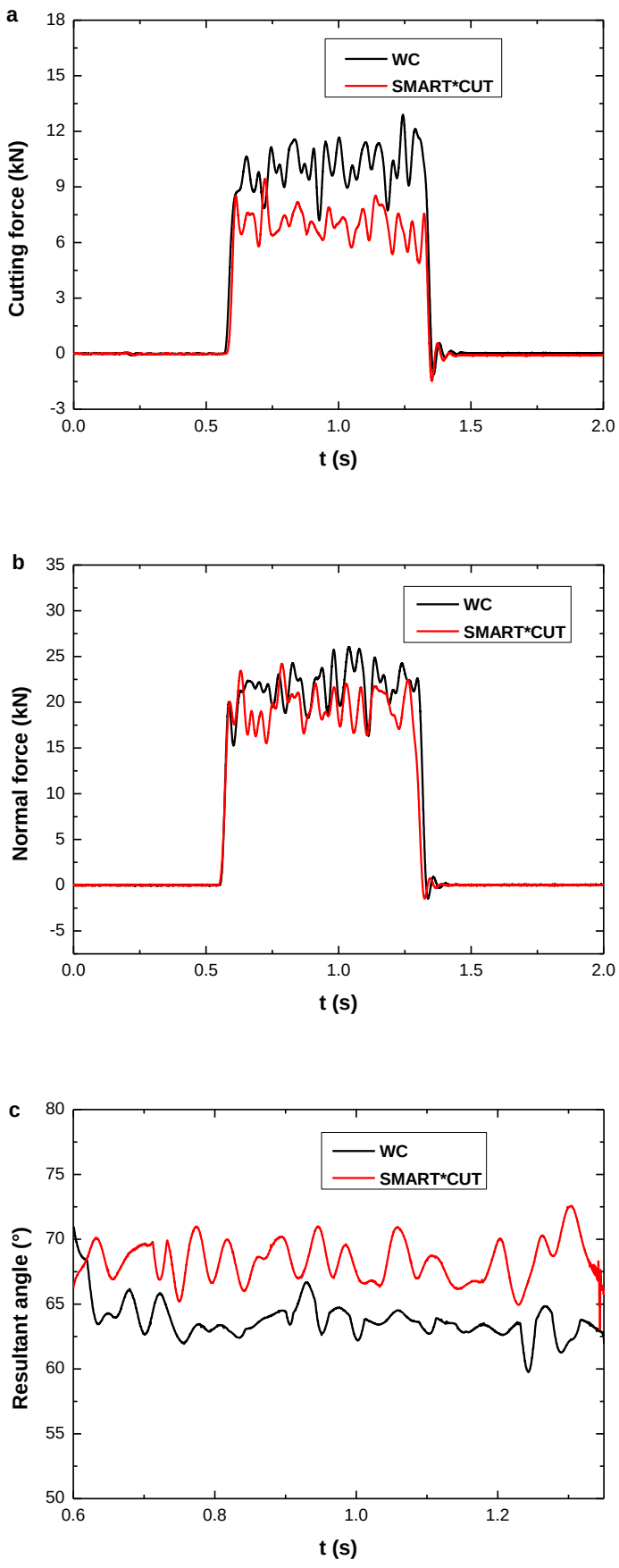

Figure 5.3 Time histories of cutting force (a), normal force (b) and resultant angle (c)

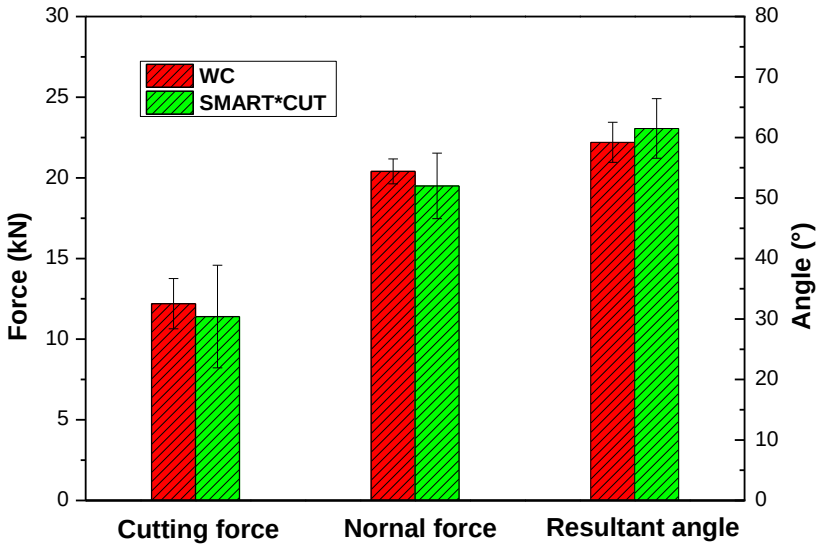

Figure 5.4 Comparison of the average cutter forces and resultant angles between the two different picks

5.3.2.1 Temperature

Pick cutting temperature is a good indicator of the heat or thermal energy generated in the rock cutting process. The determination of pick cutting temperature will assist in quantifying the risk of frictional ignition. To measure the peak cutting temperature, high frame rates are essential. Recent advances in infrared video technology have made such image capture possible, at sufficiently high speeds; so the pick temperatures at cutting speeds of 3 m/s (a speed commonly used on mining equipment) could be measured.

As shown in Figure 5.5 the maximum temperature around the cutting area of the TSDC tipped SMART*CUT picks was about 511 ^{o}C, which was more than 40% lower than that of over 860 ^{o}C for the conventional WC tipped picks used. Apparently the SMART*CUT picks generated much lower thermal energy during cutting. As shown in Figure 5.5, the maximum residual temperatures were about 104 ^{o}C and 388 ^{o}C for the SMART*CUT and WC picks, respectively. The SMART*CUT pick was significantly cooler after rock cutting compared to the WC pick. It was also observed in the test that sparks produced by the SMART*CUT picks were also much fewer than that by the WC picks.

Another advantage of SMART*CUT picks in terms of lower potential for frictional ignition is that diamond materials have much higher thermal conductivities than tungsten carbide. As the major ingredient of TSDC is synthetic diamond, it is expected that the thermal conductivity of a TSDC tip

should be much higher than that of a WC tip. So the heat produced during the cutting process was transferred to the steel body more quickly, thus leading to the reduction of the thermal energy at any hotspot that is known to be a major ignition source.

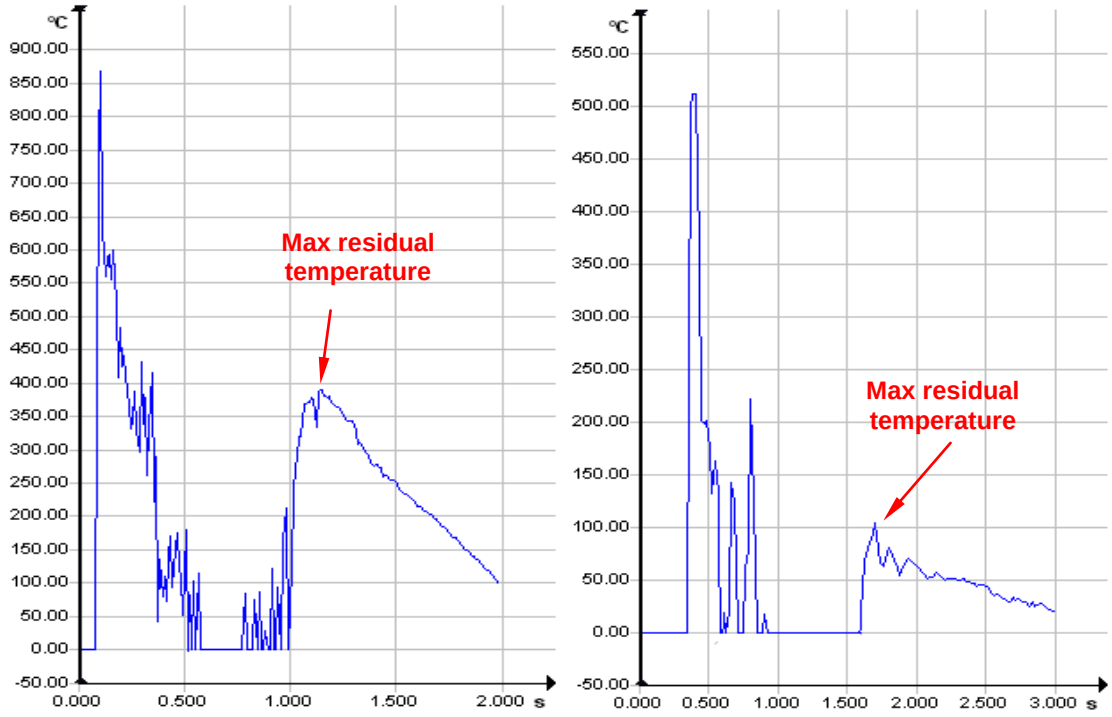

Figure 5.5 Cutting temperatures of (left) WC and (right) SMART*CUT picks

5.4 Temperature measurement by embedded thermocouple

Although the modern infrared photographic technology provides a high capture speed, fast response time and non-intrusive way to determine the temperature distribution at the pick-rock interface, the measurement might not be sufficiently accurate as flying chips and dust could strongly affect the measurement. It is hard to detect the "true" temperature at the hotspot using this technology. Therefore, a special thermocouple configuration was developed to measure the temperature at the contact surface. The influence of the cutting parameters including DOC, spacing and cutting speed on pick cutting temperature were investigated.

5.4.1 Experiment details

In this section, the rock cutting experiments were carried out on a block of Helidon sandstone. The uniaxial compressive strength, Brazilian tensile strength, Young's modulus, density and Poisson's ratio of this rock are summarised in Table 4.1. A commercial Sandvik Q8TA-2089-49612 conical

WC pick with a gauge of 70 mm, flange diameter of 51 mm, shank diameter of 30 mm, tip diameter of 16 mm and primary tip angle of 78^o was used in the test program.

As mentioned in section 3.4, a type K chromel-alumel thermocouple assembly was embedded inside the pick. A fine hole with diameter of about 1.7 mm was drilled into the WC pick by electric discharge machining (EDM). The diameter of the hole was enlarged to 3 mm near the surface of the pick tip, which produced a shoulder that prevented axial movement of the thermocouple assembly during cutting. Two half plugs made of the same pick material were designed, the two insulated thermocouple wires were glued into the pre-machined plugs and each wire terminated at the surface. The two halves were joined together to make a cylindrical insert which was then inserted into the picks (Figures 3.3 and 3.4) to measure the temperature at the pick-rock contact area during cutting.

The aim of the experiments was to measure the pick-rock interface temperature, and to investigate the influence of cutting parameters on the pick cutting temperature. A total of 16 series of tests were conducted and each test was repeated at least two times. The cutting conditions remained constant throughout the testing, including the attack angle of 55^o, the skew and tilt angles of 0^o. The normal force, cutting force and lateral force were recorded during each cutting test. The data sampling rate was 3200 per second. During the tests, the depth of cut, spacing and cutting speed were varied. The experimental conditions for temperature testing were summarised in Table 5.1.

5.4.2 Results and discussion

Figure 5.6 schematically shows the rock failure processes expected during linear rock cutting. In this figure, d is the depth of cut and θ_A is the angle of attack. Major features of the cutting process agree with the cutting theory proposed by Nishimatsu [34]. A primary crushed zone '1' is generated in front of the pick tip as soon as it has penetrated into the rock. Then a coarse chip is formed due to the propagation of a macroscopic crack when the pick penetrates deeper. This failure crack will be crushed into a fine chip zone '2' as the rock advances against the stationary pick. Finally the major chip '3' is formed without any considerable resistance until the new cycle starts again. A typical force-time history of a cutting event can be seen in Figure 5.7. The normal force was 40% greater than that of the cutting force, but the sideway force was insignificant. At the starting stage of cutting the glue and the insulation around the thermocouple wires melted due to the high temperatures generated by frictional heating. So a hot junction was formed, the two thermocouple wires connected via the WC inserts and temperatures were measured. Note that this junction was technically an "extended-junction" and not the normal "point-junction" found in conventional thermal systems. So it configuration would measure the "true" temperature at the hotspot.

Figure 5.7 shows both the measured forces and temperature in one cutting run with cutting speed of 2.5 m/s, DOC of 10 mm and spacing of 50 mm. It is seen that the transient temperature measured at the cutting interface increased rapidly when the rock starts to contact with the pick. The increase time during this stage is the time takes for the thermocouple to response to the temperature, which is also termed as the "rise time" of the thermocouple. After this period, the temperature tends to stabilize at about 1100 ^{o}C as the rock advanced continuously against the pick. Finally, the temperature decreased gradually to the room temperature after the cutting ceased. The measured pick forces fluctuated as the rock advanced through the rock surface.

Table 5.1 The rock cutting conditions for temperature measurement

Exp no.	**Attack angle (degree)**	**DOC (mm)**	**Spacing (mm)**	**Cutting speed (m/s)**
1	55	10	20	1.5
2	55	10	30	1.5
3	55	10	40	1.5
4	55	10	50	1.5
5	55	10	60	1.5
6	55	10	50	0.5
7	55	10	50	1
8	55	10	50	1.5
9	55	10	50	2
10	55	10	50	2.5
11	55	3	50	1.5
12	55	6	50	1.5
13	55	9	50	1.5
14	55	12	50	1.5
15	55	15	50	1.5
16	55	18	50	1.5

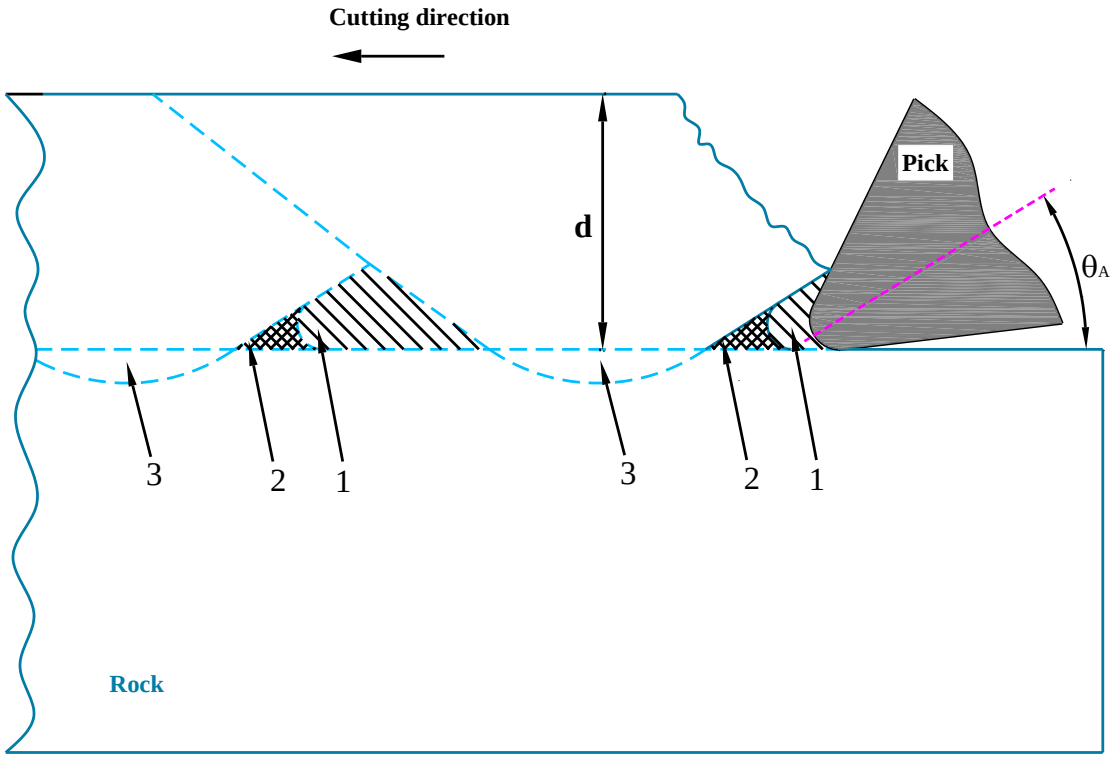

Figure 5.6 Illustration of a rock removal process in linear rock cutting (after [34])

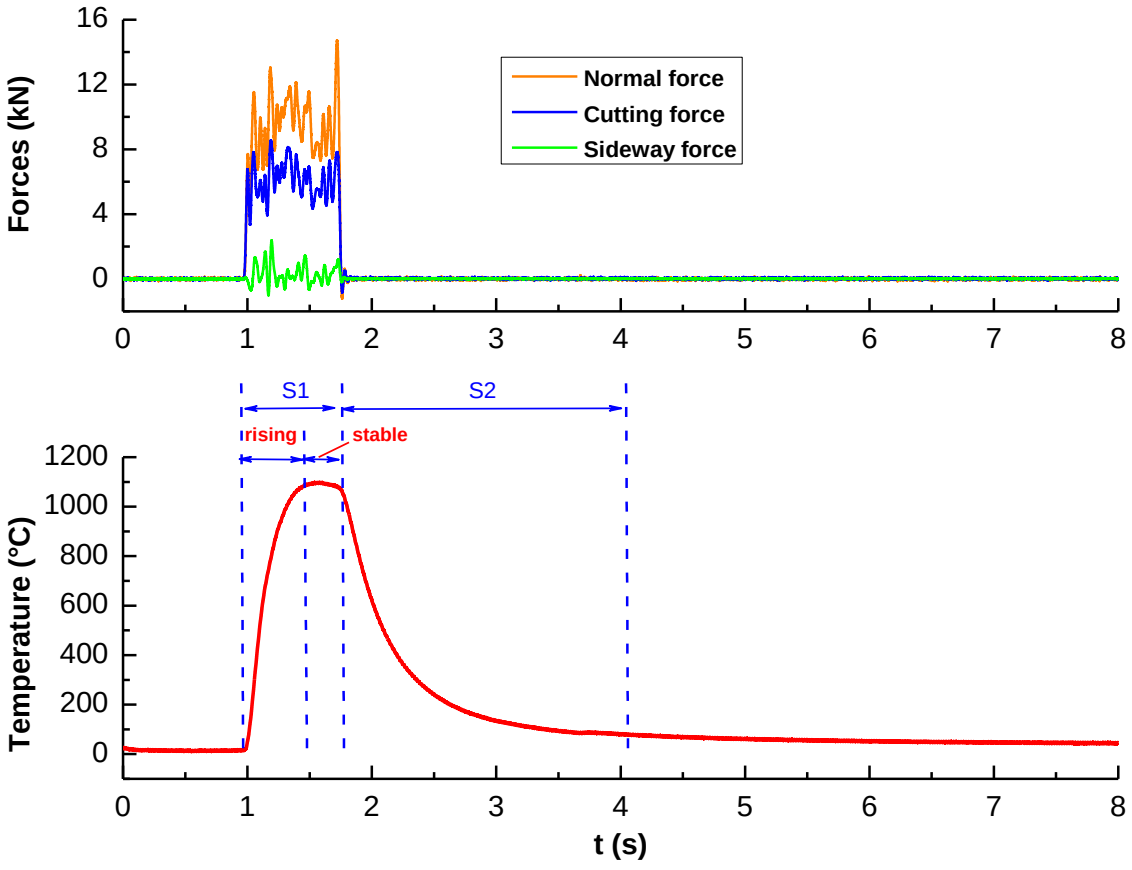

Figure 5.7 Measured rock cutting forces and temperature (v = 2.5 m/s, d = 10 mm, s = 50 mm)

5.4.2.1 Effect of cutting speed

Temperature measurements were made over the cutting speeds varied from 0.5 m/s to 2.5 m/s. The depth of cut, spacing and attack angle were set as 10 mm, 50 mm and 55^{o}, respectively. Figure 5.8 shows the time histories of the temperatures for different cutting speeds, clearly demonstrating that the higher the cutting speed, the higher the cutting temperature generated and the shorter period of thermal effect. It is obvious that there were some oscillations of the temperature curve when the cutting speed was relatively lower (e.g. 0.5 m/s and 1 m/s). When the cutting speed was higher, the temperature curve was much smoother. The fraction of large rock debris decreased with the increasing cutting speed, which means more efficient fragmentation of rock occurred at the lower cutting speed. The fragmentation of more large rock chips also led to the intermittent contact between thermocouple and rock specimen, thereby causing some fluctuations of the temperature curve when the cutting speed was low. As the cutting speed increased higher, the proportion of large rock debris became smaller and more dust was generated during the tests. The effect of cutting speed on the maximum cutting temperature is also shown in Figure 5.9. It is seen that the temperature increased continuously from 414 ^{o}C to 1100 ^{o}C as the cutting speed increased from 0.5 m/s to 2.5 m/s. The increase of temperature might be attributed to the increase of specific cutting energy, which will be discussed in details later in Chapter 6.

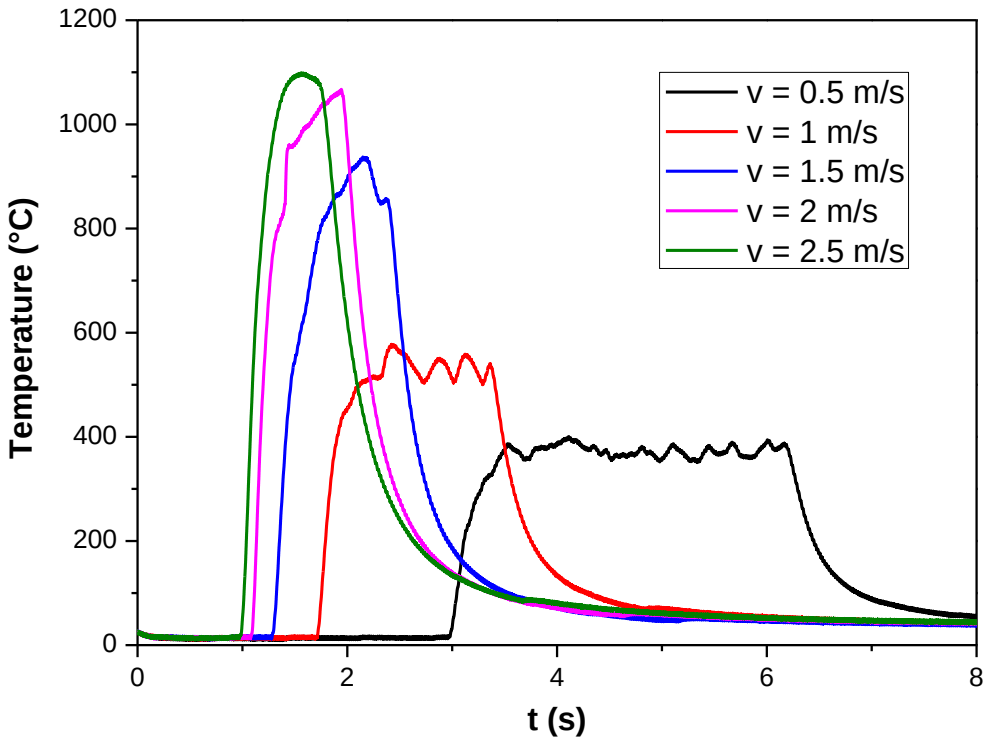

Figure 5.8 The cutting temperature time histories for different cutting speeds

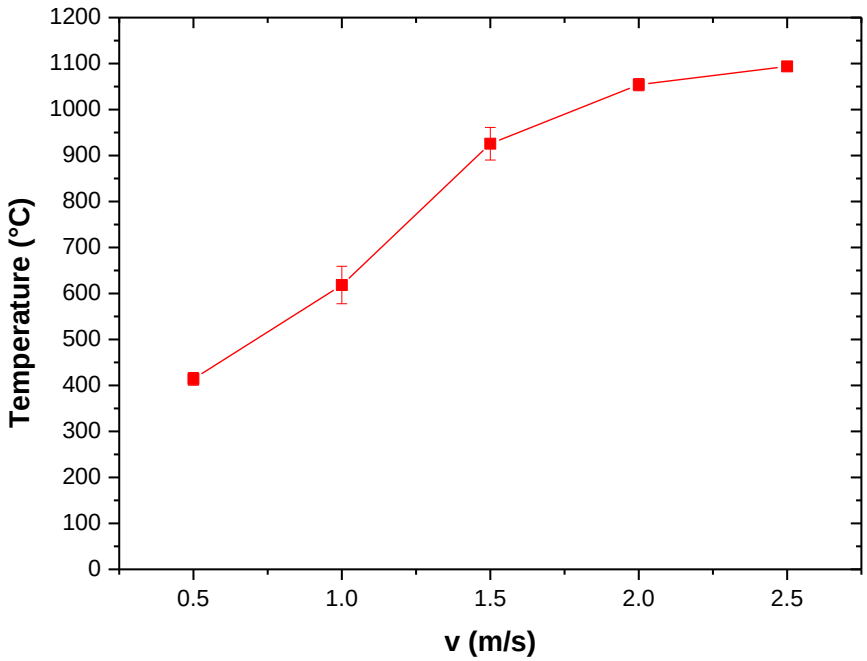

Figure 5.9 Effect of cutting speed on maximum cutting temperature

Figures 5.10 to 5.12 show the effect of cutting speed on the mean cutting force, mean normal force and resultant angle. It is seen that both the cutting force and mean force increased with increasing cutting speed. The influence was more significant for the mean normal force. The mean normal force increased about 142.6% from 3.66 kN to 8.88 kN when the cutting speed increased from 0.5 m/s to 2.5 m/s. While the increment for mean cutting force was only 54.6% in the same cutting speed range. The increases in pick forces were attributed to a less efficient fragmentation of rock occurred when the cutting speed increased. It can also be seen in Figure 5.12 that the increase in cutting speed led to the increase in resultant angle, suggesting that a larger attack angle should be employed for high speed cutting.

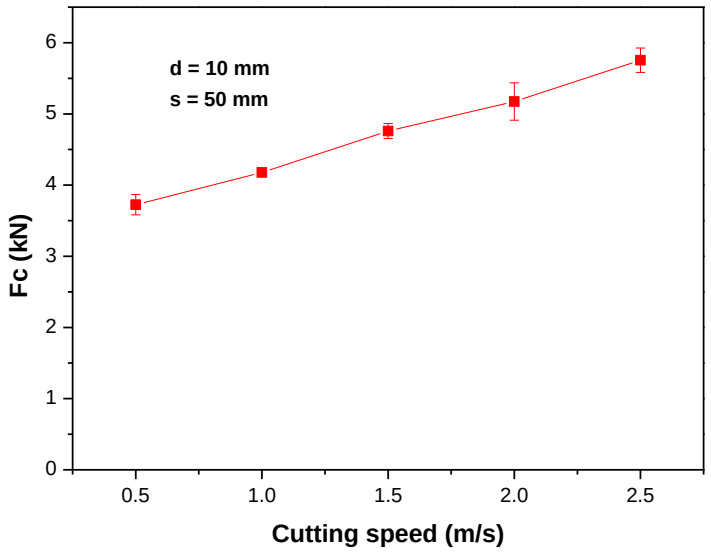

Figure 5.10 Effect of cutting speed on mean cutting force

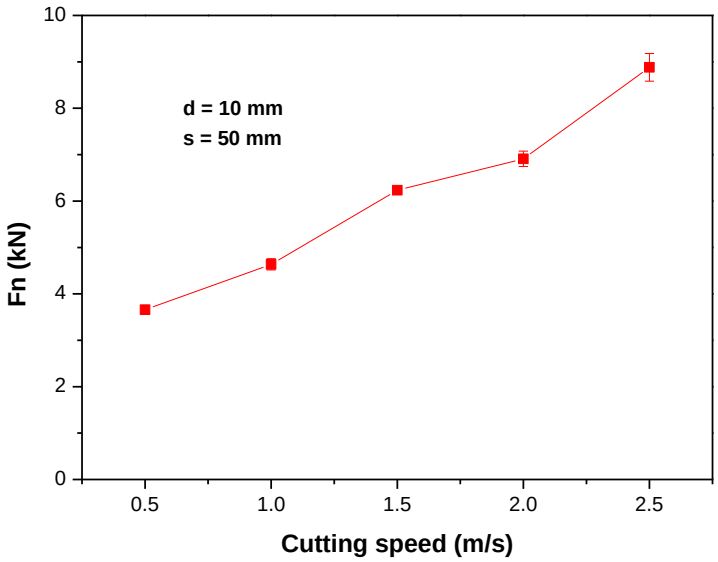

Figure 5.11 Effect of cutting speed on mean normal force

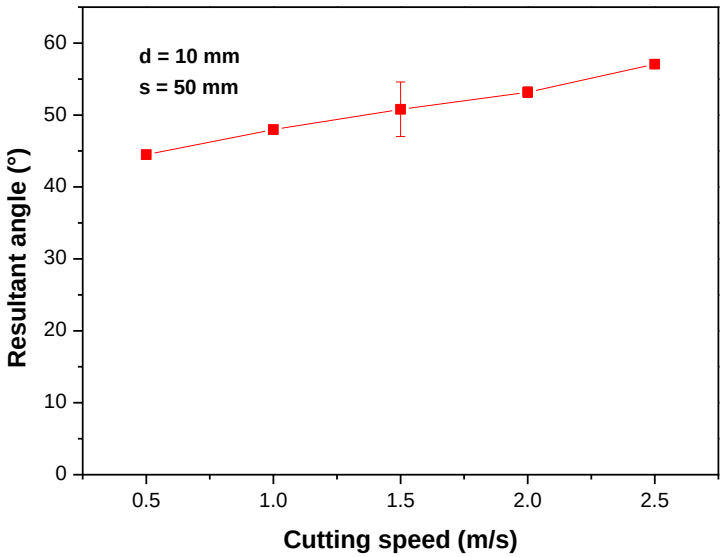

Figure 5.12 Effect of cutting speed on resultant angle

5.4.2.2 Effect of depth of cut

Depth of cut is a significant factor that affects the pick cutting performance. In this section, a wide range of depths of cut from 3 mm to 18 mm was selected to investigate their effect on the pick temperature. The other cutting conditions, including the speed of 1.5 m/s, spacing of 50 mm and attack angle of 55^{o}, were keep constant. Figures 5.13 and 5.14 show the temperature time histories and the maximum temperatures for various depths of cut used. It is seen that the increased depth of cut generally caused an increase in cutting temperature. The reasons accounted for this might be (a) the energy required to fragment the rock is proportional to the amount of new surface area produced and (b) the measured cutting forces increased linearly with the increase of depth of cut. As mentioned before, larger chips or fragments need to be breakout from the rock block when the depth of cut increases. This means higher energy consumption is required to generate larger new fracture area, thereby resulting in more frictional heat and thus higher temperature generated at the pick rock interface. It is also noted from Figure 5.14 that the temperature increase was much more significant at lower depths of cut. The maximum cutting temperature increased about 152.7% from 313 ^{o}C to 791 ^{o}C when the depth of cut increased from 3 mm to 9 mm. However, when the depth of cut varied from 9 mm to 18 mm, the cutting temperature arose only about 19.2% from 791 ^{o}C to 943 ^{o}C. This might partly because the specific energy was reaching a saturated value with the increasing depth of cut [48, 87-89].

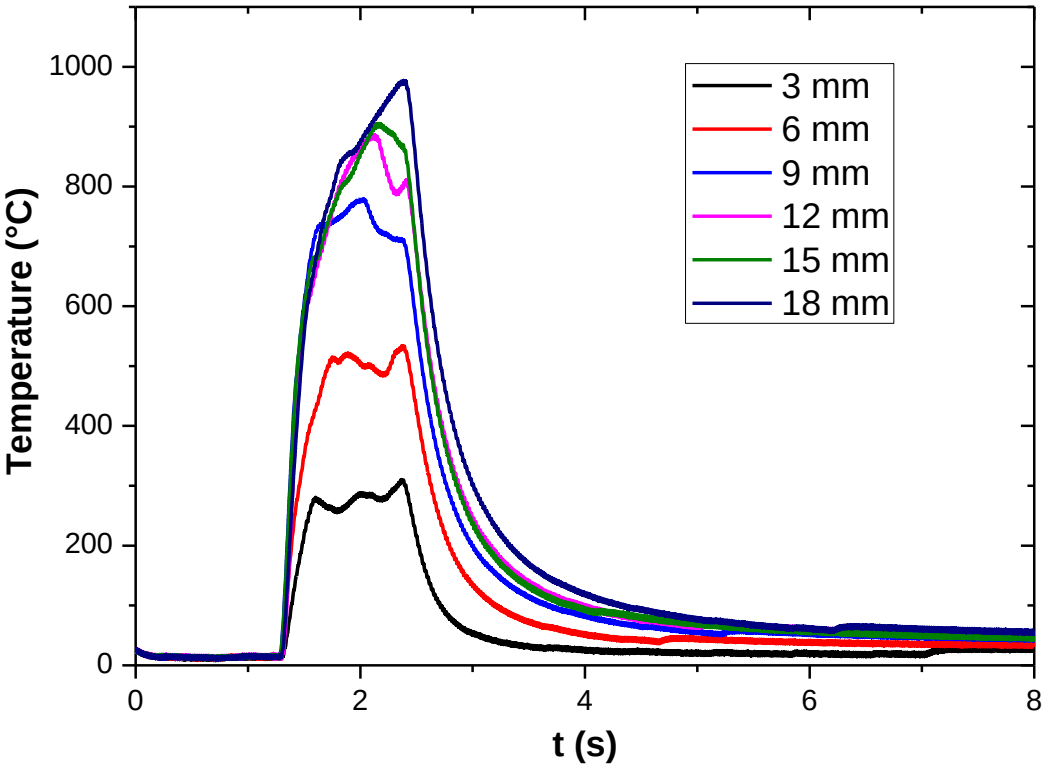

Figure 5.13 The cutting temperature time histories for different depths of cut

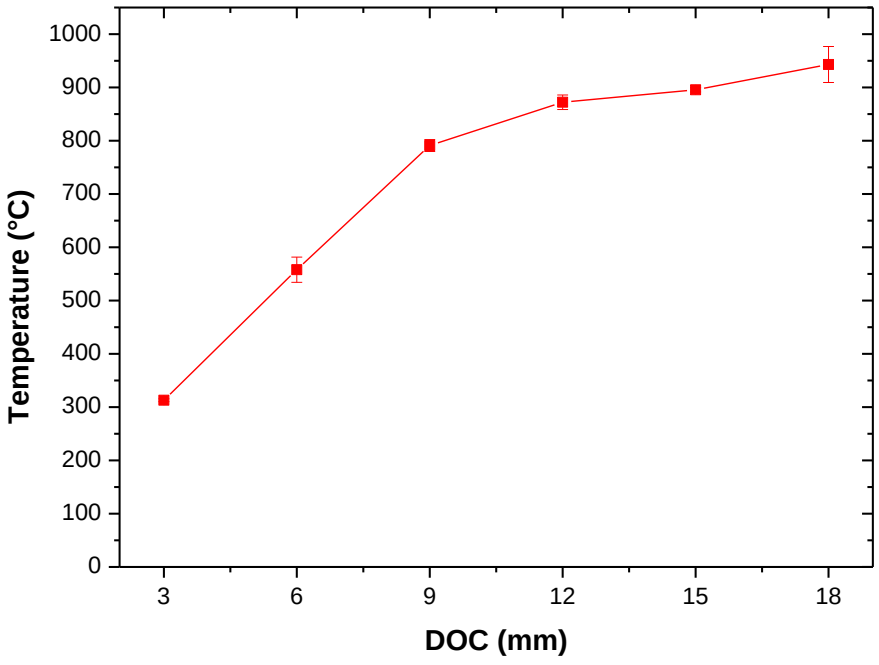

Figure 5.14 Effect of depth of cut on maximum cutting temperature

The effect of depth of cut on mean cutting force, mean normal force and resultant angle are shown in Figures 5.15 to 5.17, respectively. It can be seen in Figures 5.15 and 5.16 that both the pick forces (mean cutting and normal forces) have linear relationship with the depth of cut, with

determination coefficients (R^2) of 0.99. Both the magnitude and increase rate of mean normal force were higher than that of mean cutting force. From Figure 5.17 it can also be seen that there was a fluctuation of the resultant angle when the depth of cut was below 9 mm; however, it decreased gradually when the depth of cut increased from 9 mm to 18 mm.

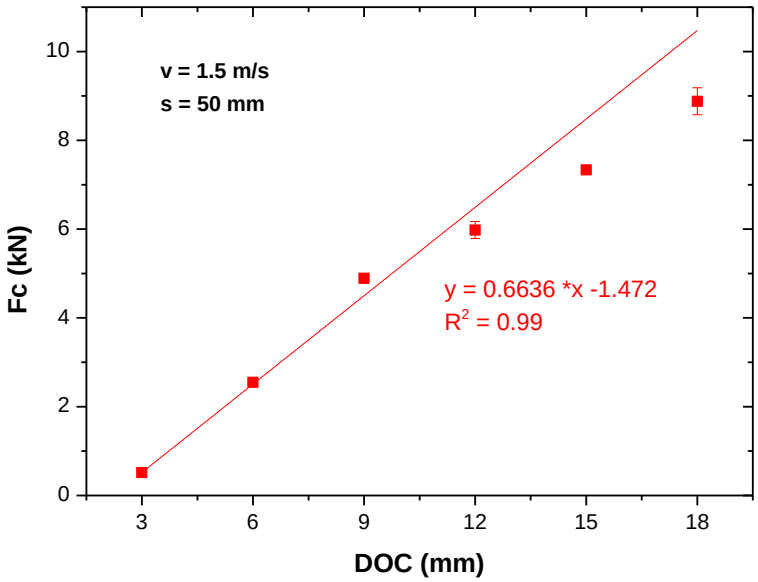

Figure 5.15 Effect of depth of cut on mean cutting force

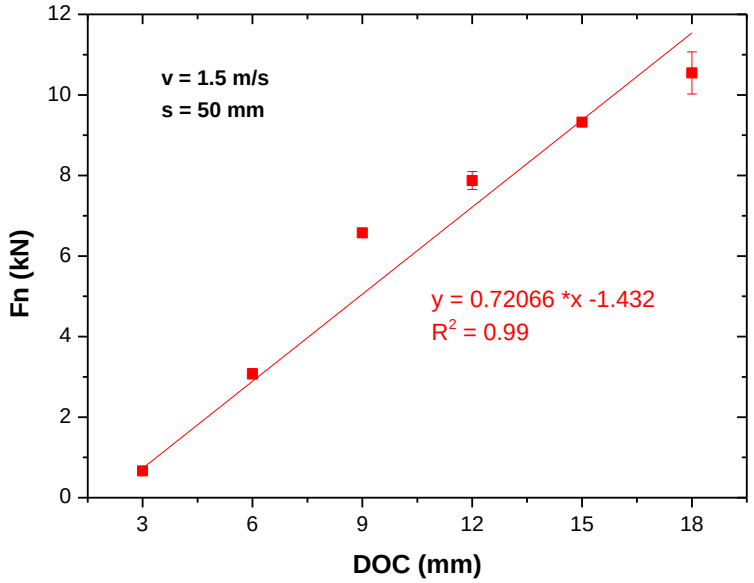

Figure 5.16 Effect of depth of cut on mean normal force

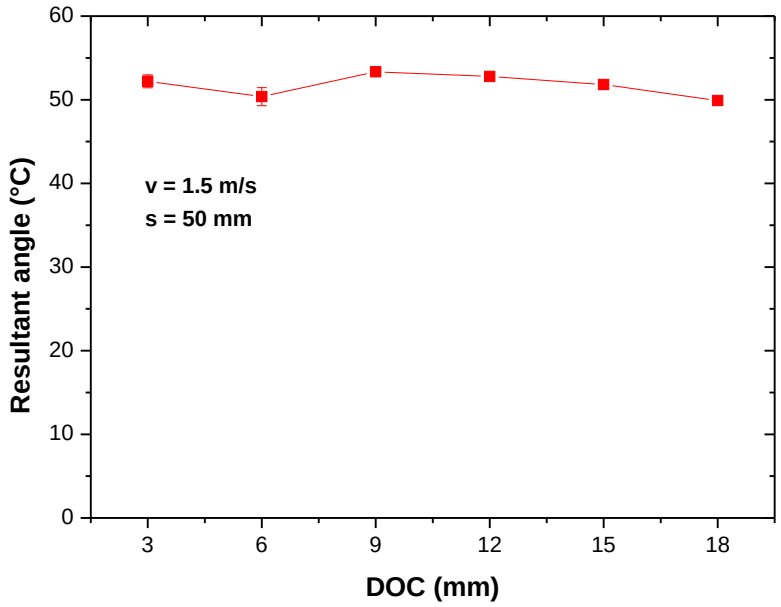

Figure 5.17 Effect of depth of cut on resultant angle

5.4.2.3 Effect of spacing

The effect of the spacing between two adjacent cuts on the cutting temperature was examined. The spacing was ranged from 20 mm to 60 mm, while the depth of cut, speed and attack angle were kept constant at 10 mm, 1.5 m/s, and 55^{o}. The temperature time histories and the maximum temperatures obtained at various spacing are shown in Figures 5.18 and 5.19. It is seen that the increase in the spacing resulted in an increase in the interface temperature. The temperature increased about 34.7% from 668 ^{o}C to 900 ^{o}C for the spacing below 40 mm, while there was only a slight increase of about 5.2% from 900 ^{o}C to 947 ^{o}C when the spacing was above 40 mm. The increasing rate of the temperature for the spacing below 40 mm was greater than for the spacing above 40 mm. It is suggested that the difference in the temperature response outlined above is due to a change in cutting mode. Relieved cutting occurred at relatively narrow spacing, so the amount of rock volume was smaller and more effective interaction might be created under this cutting condition. This also means that less energy was required to remove the rock, thereby resulting in lower interface temperature at narrow spacing. When the spacing increased above 40 mm, the cutting might be converted to the unrelieved cutting, so the cutting efficiency dropped rapidly due to the formation of ridge. The pick forces and the rock volumes being removed from the rock surface would not be changed if unrelieved cutting happens. That was why the variation of temperatures was insignificant when the spacing was too great. Apparently, the effect of spacing on pick cutting temperature was not as great as the effects of cutting speed and depth of cut.

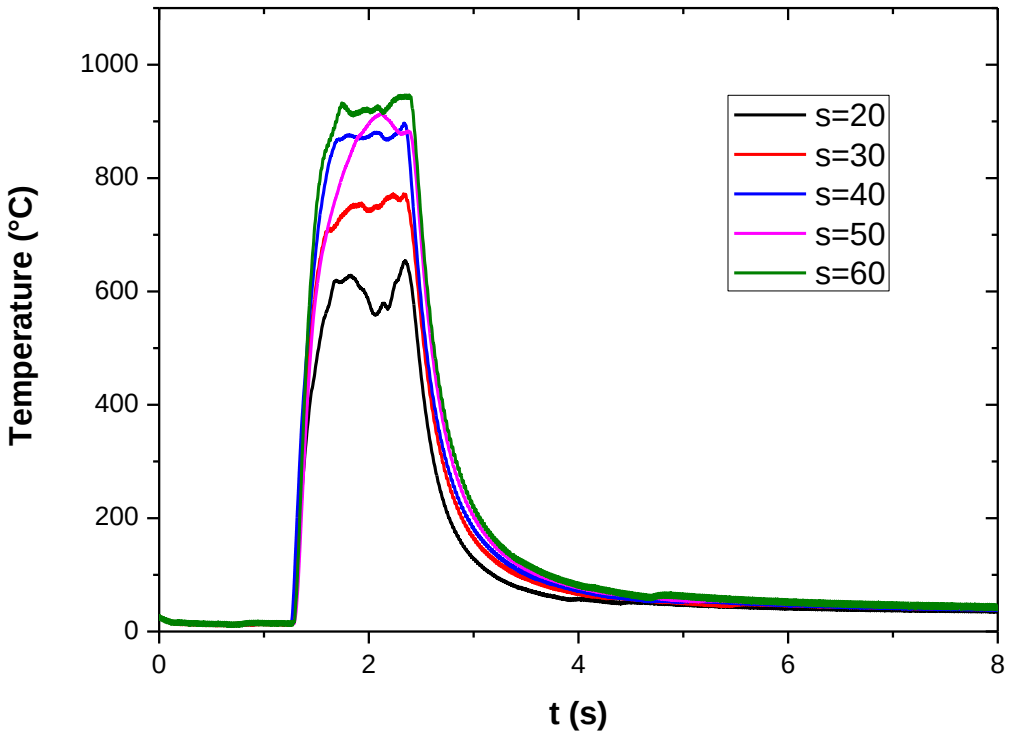

Figure 5.18 The cutting temperature time histories for different line spacing

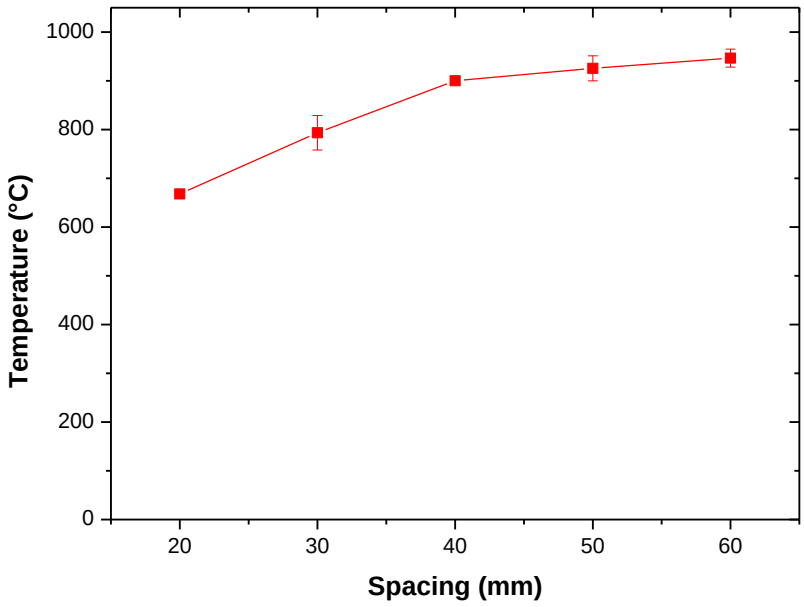

Figure 5.19 Effect of spacing on maximum cutting temperature

Spacing is a key parameter in cutterhead design, and plays an important role in influencing the cutting efficiency. The effect of spacing on mean cutting force, mean normal force and resultant angle is shown in Figures 5.20 to 5.22. The pick forces increased gradually with the increasing spacing, but increase of the force was much smaller when the spacing was above 50 mm. This is

because no interaction between adjacent cuts occurred when the spacing was greater than 50 mm and the cutting mode changed from relieved to unrelieved cutting. From Figure 5.22, it can see that the effect of spacing on the resultant angle was insignificant. The resultant angle varied from 47.8^{o} to 51.3^{o} for all the spacing used.

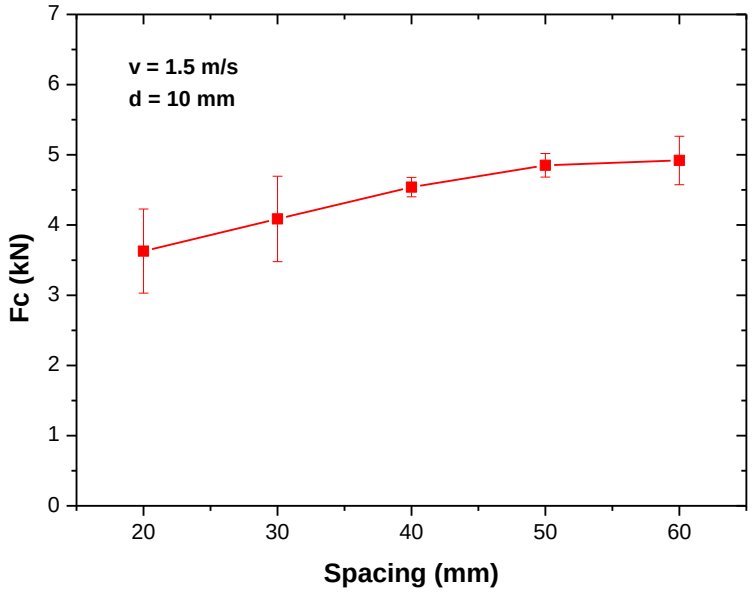

Figure 5.20 Effect of spacing on mean cutting force

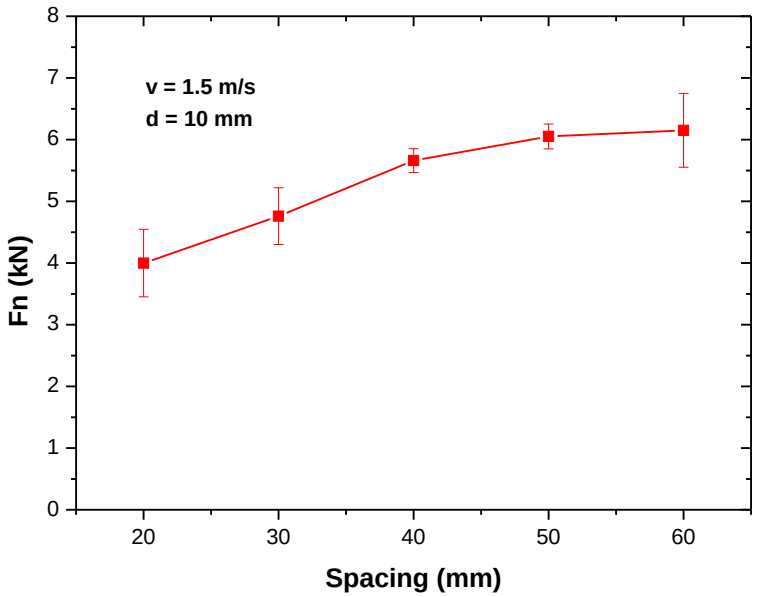

Figure 5.21 Effect of spacing on mean normal force

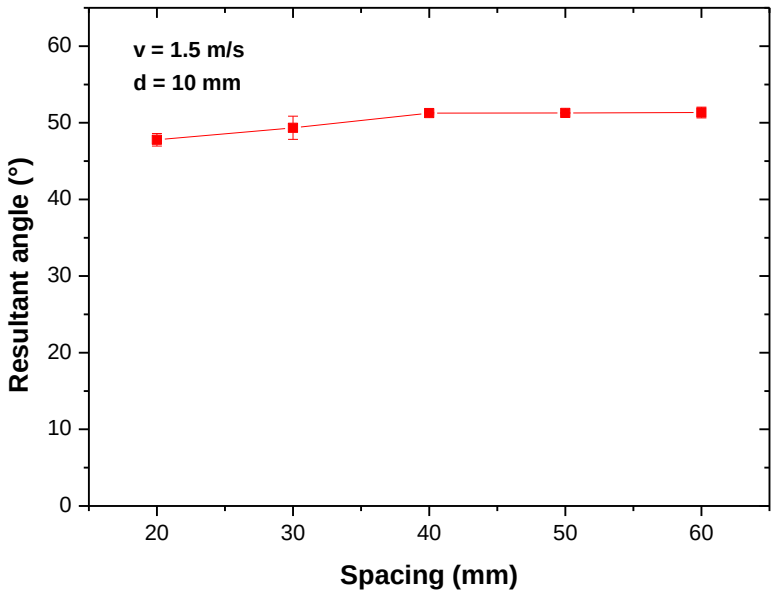

Figure 5.22 Effect of spacing on resultant angle

The highest temperature of 1100 ^{o}C was obtained at the cutting speed of 2.5 m/s, the depth of cut of 10 mm and the spacing of 50 mm. Reddish and black discontinuous banding chips were found in the cutting grooves under this cutting condition, as shown in Figure 5.23.

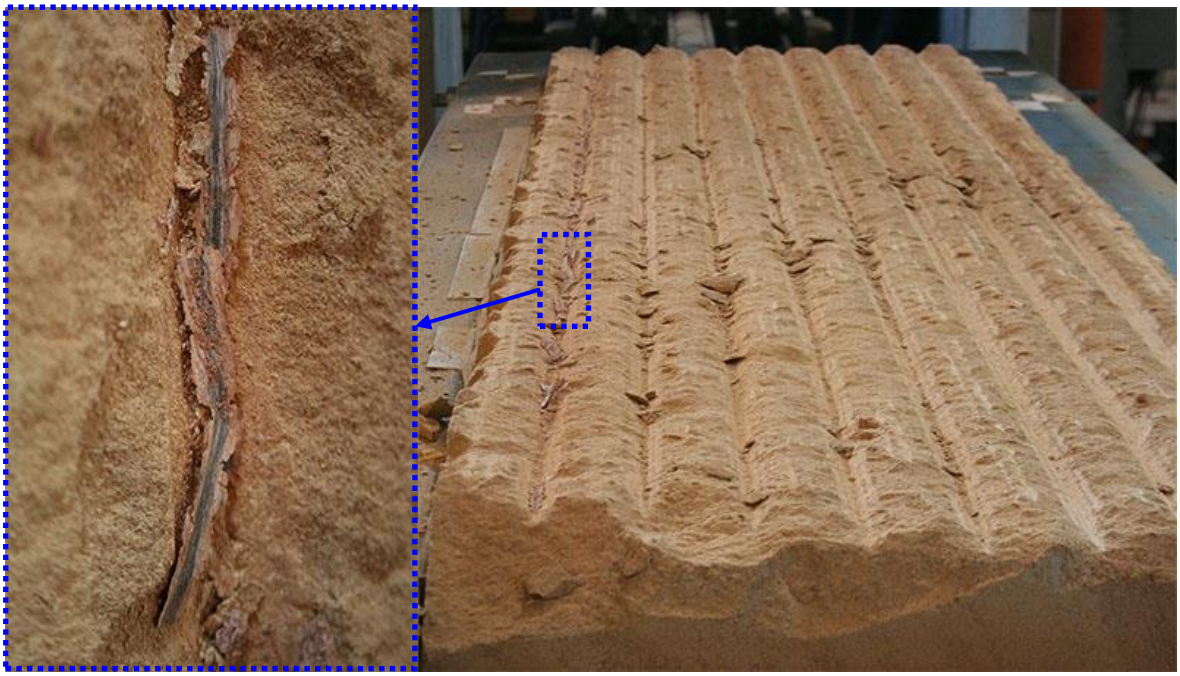

Figure 5.23 Reddish and black discontinuous banding chips was found in the cutting grooves when the cutting temperature reached 1100 ^{o}C (v = 2.5 m/s, d = 10 mm, s = 50 mm)

5.5 Concluding remarks

A thermal infrared camera with high capture rates was used to measure the temperature distribution in the cutting area. The SMART*CUT picks appeared to generate much less heat during cutting than the conventional WC picks. The maximum temperature around the cutting area of the SMART*CUT pick was about 511 ^{o}C, which is more than 40% lower than that of the conventional WC tipped pick (over 860 ^{o}C). The residual temperature of the SMART*CUT picks after the rock cutting was lower compared with that of the WC picks. The average residual temperatures were about 104 ^{o}C and 388 ^{o}C for the SMART*CUT and WC picks, respectively. The sparks produced by the SMART*CUT picks were also much fewer than those caused by the WC pick.

A special thermocouple configuration was further developed to measure the temperature upon the contact surface between a pick and the rock material. The transient temperature at the hot spot was successfully measured when the rock advanced against the pick. The effects of the cutting parameters including depth of cut, spacing and cutting speed on pick temperature were investigated. It was found that the pick tip temperature increased significantly with the increased depth of cut and cutting speed. The effect of spacing on the pick tip temperature was smaller than that of the depth of cut and cutting speed, particularly when the spacing was greater than that required to change from unrelieved to relieved cutting. For all the cutting conditions used, the pick tip temperature varied from 313 ^{o}C to 1100 ^{o}C. The highest temperature was obtained as about 1100 ^{o}C with cutting speed of 2.5 m/s, DOC of 10 mm and spacing of 50 mm. Reddish and black discontinuous banding chips were found in the cutting grooves under this cutting condition.

6

Cutting chips and specific energy

6.1 Introduction

Cutting efficiency is another important factor to determine the production and economics of rock cutting machinery [177]. An indicator of the efficiency of mechanical excavators [4, 78, 80] is specific energy which is defined as the work done per unit volume of rock cut. It can be used to assess the rock cuttability and excavation performance for a particular mechanical excavator. Size distribution of the chips generated during rock cutting process is also closely related with rock cutting efficiency, and may provide some information on rock fragmentation mechanisms [177]. It is therefore very important to investigate the chip size distribution and specific energy under different cutting conditions.

In this chapter, a series of full-scale linear rock cutting tests based on the Taguchi method was initially performed to identify and quantify the effects of different rock cutting parameters on the coarseness index of TSDC tipped picks. Then, depth of cut, cutting speed and spacing which have relatively greater contributions on the coarseness index were chosen to further analyse rock chips sizes and distribution. Finally, the cutting specific energy under various cutting conditions was investigated.

6.2 Coarseness index

Chip size is an important parameter to determine the cutting efficiency in rock cutting. Several methods have been proposed in the past to analyse the rock chips from instrumented cutting tests [178]. It was pointed out by Bruland [179] that chip size is mainly controlled by advance of the cutters into the rock per revolution of the cutterhead and the spacing between the neighbouring cutter grooves. Tuncdemir [177] stated that rock discontinuities also play an important role in the dimensions of chips.

The coarseness index (CI) which is defined as the sum of the cumulative weight percentages of rock debris retained in each sieve is a convenient and rapid technique to analyse the debris size [48]. It is evident that this non-dimensional number increases with the increase of cutting efficiency [180]. As mentioned in section 3.7, a series of sieves have been used in this study: 22.4 mm, 16mm, 8 mm, 4 mm and 1 mm. After each test, the collected chips were passed through these sieves and assembled into six size classes, the mass retained in each sieve was

weighed and the cumulative percentage mass retained from coarsest to finest mesh was obtained. The summation of the cumulative percentage values represented the Coarseness Index of the sample. An example of the calculation of coarseness index is given in Table 6.1.

Table 6.1 Calculation of coarseness index

Mesh size (mm)	Weight (g)	Weight (%)	Cumulative weight (%)
22.4	788.4	62.1	62.1
16	106.6	8.4	70.5
8	88	7.0	77.5
4	82.5	6.5	84
1	78	6.1	90.1
<1	125.2	9.9	100
Total weight	1268.7		
Coarseness Index (CI)			$\sum = 484.3$

6.2.1 Experimental details

In this section, the rock cutting experiments were still conducted on a block of Helidon sandstone. The TSDC tipped picks (Figure 3.8) developed by CSIRO were used as the cutting tool. The Taguchi's L25 orthogonal array (Table 4.3) was also applied to investigate the effects of the main cutting parameters on coarseness index.

6.2.2 Results and discussion

The coarseness index was set as the objective function for the chip size analysis, and four factors (i.e., attack angle, DOC, spacing and cutting speed) were selected as the main cutting parameters. The results obtained from the cutting tests according to the Taguchi experimental plan are shown in Table 6.2.

Since higher values of coarseness index are desirable in rock cutting process, the larger-the-better S/N quality characteristic is chosen in this section. By taken into consideration Eq. (4.4), the S/N ratios for each experiment was calculated and tabulated in Table 6.2.

Table 6.2 Experimental results of CI and corresponding S/N ratios

Test No.	Attack angle (°)	DOC (mm)	Spacing (mm)	Cutting speed (m/s)	Coarseness index	
					Result	S/N (dB)
1	45	6	24	0.5	304	49.670
2	45	9	36	1	385	51.706
3	45	12	48	1.5	435	52.775
4	45	15	60	2	486	53.739
5	45	18	72	2.5	528	54.454
6	50	6	36	1.5	293	49.325
7	50	9	48	2	328	50.313
8	50	12	60	2.5	360	51.131
9	50	15	72	0.5	484	53.702
10	50	18	24	1	505	54.071
11	55	6	48	2.5	238	47.549
12	55	9	60	0.5	417	52.396
13	55	12	72	1	459	53.246
14	55	15	24	1.5	451	53.092
15	55	18	36	2	422	52.513
16	60	6	60	1	314	49.951
17	60	9	72	1.5	389	51.799
18	60	12	24	2	364	51.213
19	60	15	36	2.5	380	51.602
20	60	18	48	0.5	512	54.193
21	65	6	72	2	266	48.502
22	65	9	24	2.5	312	49.887
23	65	12	36	0.5	445	52.974
24	65	15	48	1	457	53.204
25	65	18	60	1.5	482	53.662

6.2.2.1 The S/N ratio analysis

Based on the S/N ratios of each experiment in Table 6.2, the mean S/N ratios of each process factors at different experimental levels can be obtained by averaging their S/N ratios at the

corresponding levels. All these mean S/N ratios produce the S/N response table for coarseness index (see Table 6.3).

The objective quality characteristic of the coarseness index is larger-the-better, which means the highest value of coarseness index would be the ideal situation. The mean S/N ratio for coarseness index is shown in Figure 6.1. It can be seen that the highest S/N ratio for coarseness index is obtained at attack angle of 45^{o} (level 1), depth of cut of 18 mm (level 5), spacing of 72 mm (level 5), and cutting speed of 0.5 m/s (level 1).

Table 6.3 S/N response table for coarseness index

Symbol	Parameters	Mean S/N ratio (dB)					
		Level 1	Level 2	Level 3	Level 4	Level 5	Max-Min
A	Attack angle	52.47*	51.71	51.76	51.75	51.65	0.82
B	Depth of cut	49.00	51.22	52.27	53.07	53.78*	4.78
C	Spacing	51.59	51.62	51.61	52.17	52.34*	0.75
D	Cutting speed	52.59*	52.44	52.13	51.25	50.92	1.66

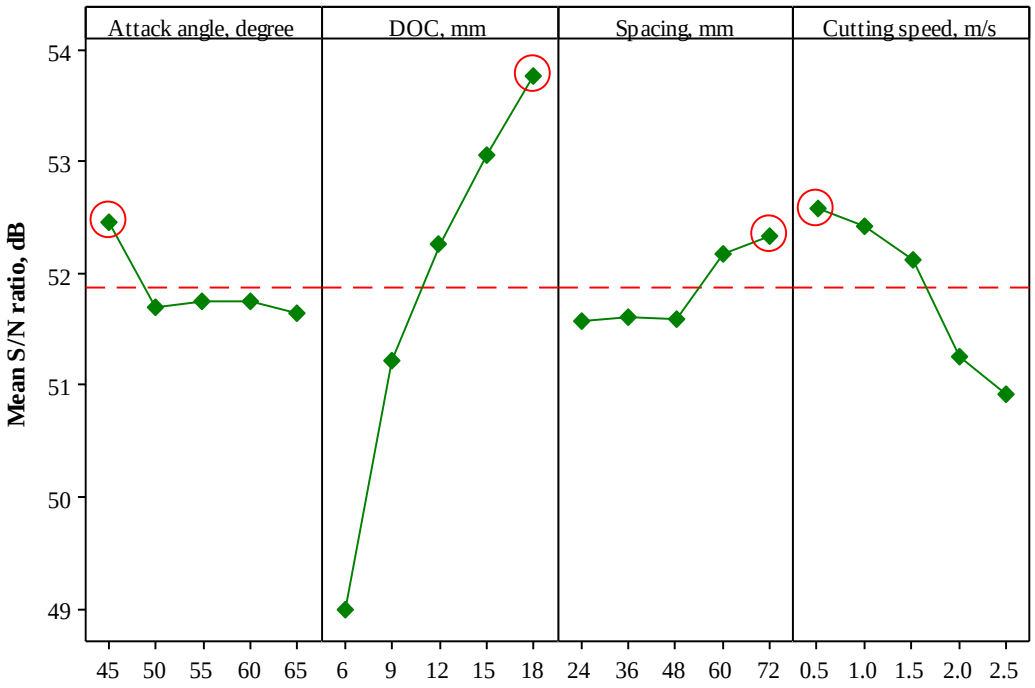

Figure 6.1 Mean S/N ratio graph for coarseness index

6.2.2.2 Analysis of variance （ANOVA）

Various relative quality effects including total squared deviation, the mean squared deviation, F ratio, P-value and contribution are computed in the ANOVA table to investigate the statistically significant parameters influencing the quality characteristic and identify the percent contribution ratio (PCR) of each process factor on output responses. The results of ANOVA for coarseness index are presented in Table 6.4. It can be seen from Table 6.4 that DOC and cutting speed have statistical significance on coarseness index as their P-value of are much less than 0.05. It is observed from Figure 6.1 that the most influential factor for coarseness index is DOC with a contribution percentage of 78.75%, followed by cutting speed (11.57% contribution). Spacing and attack angle, which contribute 3.66% and 2.82% respectively, have relatively insignificant effects on coarseness index.

Table 6.4 Results of ANOVA for coarseness index

Factor	DF	Seq SS	Adj SS	Adj MS	F ratio	P	Contribution (%)
Attack angle	4	4612	4612	1153	1.76	0.229	2.82
DOC	4	128711	128711	32177.7	49.23	0	78.75
Spacing	4	5989	5989	1497.1	2.29	0.148	3.66
Cutting speed	4	18905	18905	4726.3	7.23	0.009	11.57
Error	8	5229	5229	653.7			3.20
Total	24	163446					100

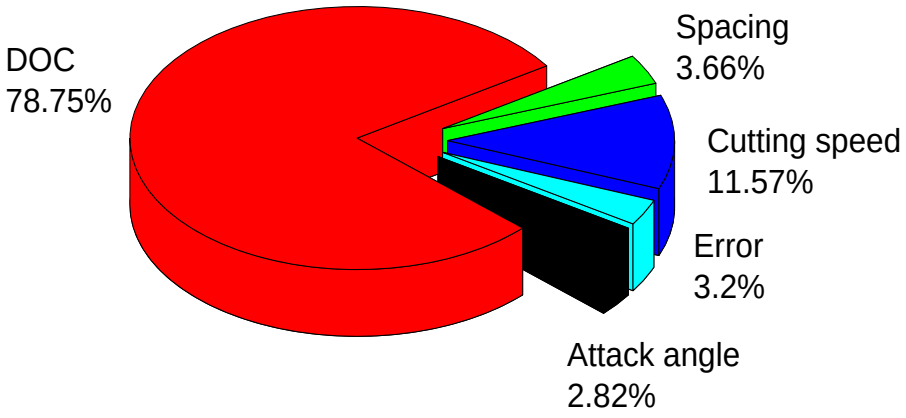

Figure 6.2 Contribution pie chart of coarseness index

6.2.2.3 Effect of cutting parameters on coarseness index

The coarseness index value of each process factors at different experimental levels can be determined by averaging their coarseness index at corresponding levels. The effects of the main cutting parameters on mean values of coarseness index are shown in Figure 6.3. According to Figure 6.3, the coarseness index decreases when the attack angle increases from 45^{o} to 50^{o}, then coarseness fluctuates slightly with further increases of attack angle. The increases in DOC and spacing, in general, produce increases in the magnitude of coarseness index.

The increase of DOC, as shown in Figure 6.3, caused a rapid increase in coarseness index. The coarseness index increased about 73% from 283.2 to 490 when the DOC increased from 6 mm to 18 mm. The coarseness index also increased with an increase of spacing. However the rate of increase was only around 10%, which is much less than that of DOC. As the cutting speed increased, the coarseness index gradually decreased.

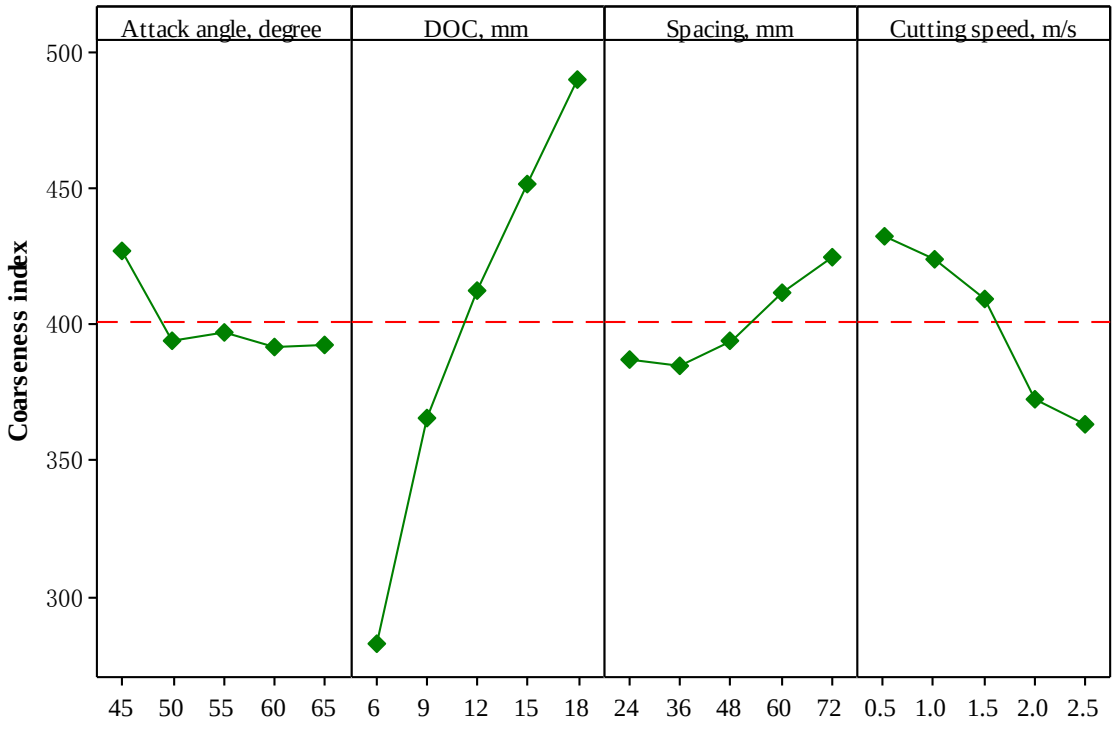

Figure 6.3 Mean effects plot for coarseness index (red dashed line indicates mean value)

6.3 Rock chips sizes and distribution

The size and distribution of the rock chips may help to decipher some possible breaking mechanisms. The dust, cutting specific energy and economic efficiency are directly affected by rock debris sizes [181]. The larger the rock chips and the fewer fines means less the dust, a lower specific energy and a higher economic efficiency. From the above section it can be seen that depth of cut, cutting speed and spacing have relatively greater contributions to the coarseness index. Thus, in this section another 15 tests were performed to further analyse the influence of these parameters on the rock chips sizes and distribution of TSDC tipped picks. The constant conditions throughout the testing program include the attack angle of 55^{o}, the skew and tilt angles of 0^{o}. After each test, the rock debris were carefully collected and sieved into five sieves to determine the mass percentages of the chips with different sieve sizes. The experimental program of the linear cutting tests is list in Table 6.5.

Table 6.5 Experimental program of the rock cutting tests

Test No.	Attack angle (degree)	DOC (mm)	Spacing (mm)	Cutting speed (m/s)
1	55	6	50	1.5
2	55	9	50	1.5
3	55	12	50	1.5
4	55	15	50	1.5
5	55	18	50	1.5
6	55	10	20	1.5
7	55	10	30	1.5
8	55	10	40	1.5
9	55	10	50	1.5
10	55	10	60	1.5
11	55	10	50	0.5
12	55	10	50	1.0
13	55	10	50	1.5
14	55	10	50	2.0
15	55	10	50	2.5

Different size groups of rock chips obtained in the tests are shown in Figure 6.4. The effect of depth of cut, spacing and cutting speed on the size and distribution of rock chips was analysed in the following sub-sections. As shown in Table 6.5, the depths of cut of 6 mm, 9 mm, 12 mm, 15 mm and 18 mm, the spacing of 20 mm, 30 mm, 40 mm, 50 mm, and 60mm and the cutting speeds of 0.5 m/s, 1 m/s, 1.5 m/s, 2 m/s and 2.5 m/s were used in the linear rock cutting tests,.

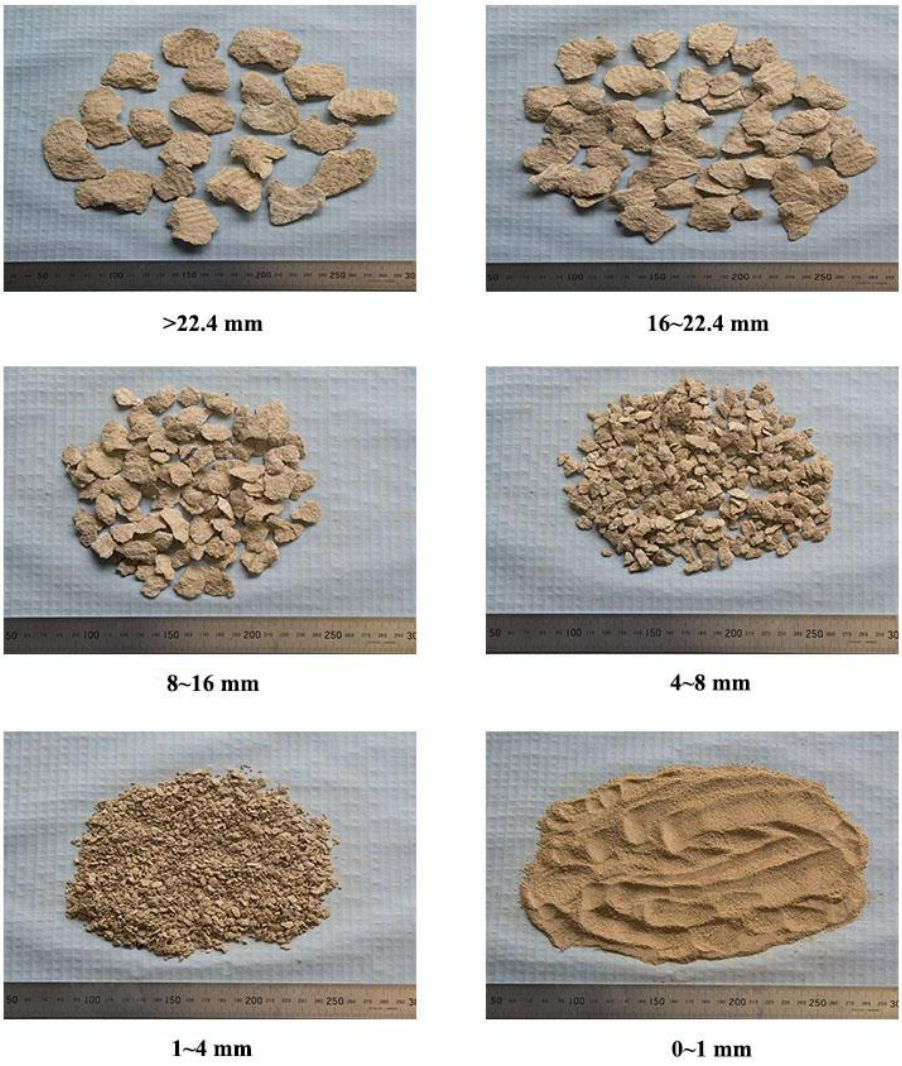

Figure 6.4 Rock chips sizes

6.3.1 Effect of depth of cut

In order to study the effect of depth of cut on the size and distribution of rock chips, the spacing and cutting speed were set as a constant (50 mm and 1.5 m/s respectively). The chip size distribution in terms of mass percentages under the different depths of cut was presented

statistically in Figure 6.5. The fraction of rock chips size less than 1 mm was considered as the dust proportion generated during each test. The reasons offered to account for these fines were the remarkable friction between rock and picks and the secondary crushing of rock chips. It was shown in Figure 6.5 that the dust proportion decreased from about 20% to around 10% when the depth of cut increased from 6 mm to 18 mm. Similar trends were found at size ranges of 1~4 mm, 4~8 mm, and 8~16 mm. Moreover, chips at depths of cut of 6 mm and 9 mm were almost distributed on size below 22.4 mm. While chips at larger depths such as 12 mm, 15 mm, and 18 mm were distributed mainly over size above 22.4 mm. It was evident that the mass percentages for the size of chips larger than 22.4 mm increased with the increase of depth of cut. Figure 6.6 shows typical sets of chips generated at different depths of cut. According to this figure, the size of chips also increased significantly with the increase of depth of cut.

It can be concluded that cutting efficiency was higher at larger depth of cut as less dust, and more and larger chips were generated.

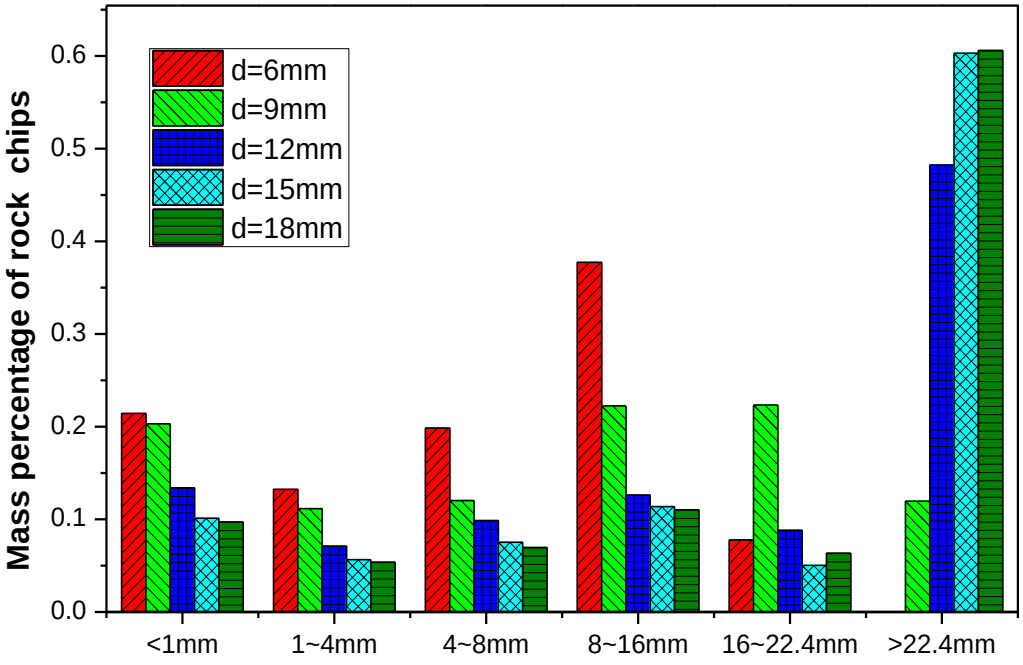

Figure 6.5 Chip size distribution under different depths of cut

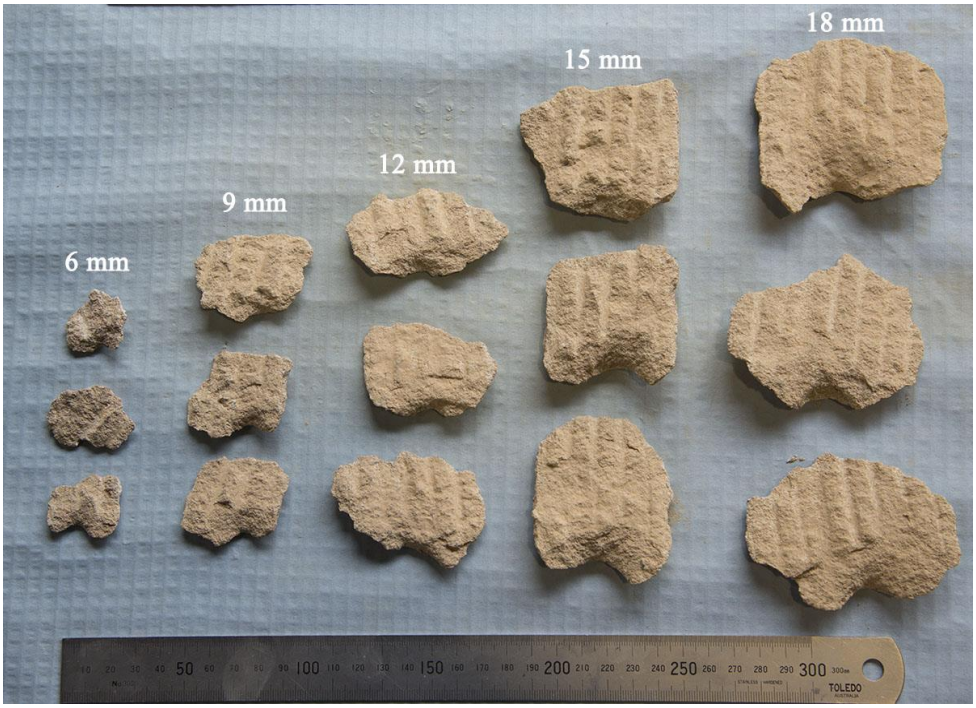

Figure 6.6 Morphology of the typical chip sets at different depths of cut

6.3.2 Effect of spacing

In order to keep the spacing to depth of cut ratio (s / d) within a certain range (from 2 to 6), the spacing was set to 20 mm, 30 mm, 40 mm, 50 mm, and 60mm when the depth of cut and cutting speed were kept as a constant (10 mm and 1.5 m/s respectively).

Figure 6.7 shows the statistical chip size distribution in terms of mass percentages under different spacing. It can be seen that the variation of the dust proportion at various spacing was not as obvious as that with different depths of cut. The fraction of rock chips size less than 1 mm decreased a little when the spacing increased from 20 mm to 30 mm, then the dust proportion increased slightly with a further increase of spacing. Chips mostly distributed on size large than 8 mm for all the spacing. It was clear that the mass percentages of large chips (over 22.4 mm) was maximum (nearly 35%) at the spacing of 40 mm. While the fraction of large chips for other spacing was around 25%. The typical sets of chips generated at different spacing were shown in Figure 6.8. It was worth noting that the width of the chips increased gradually as the spacing increased from 20 mm to 60 mm.

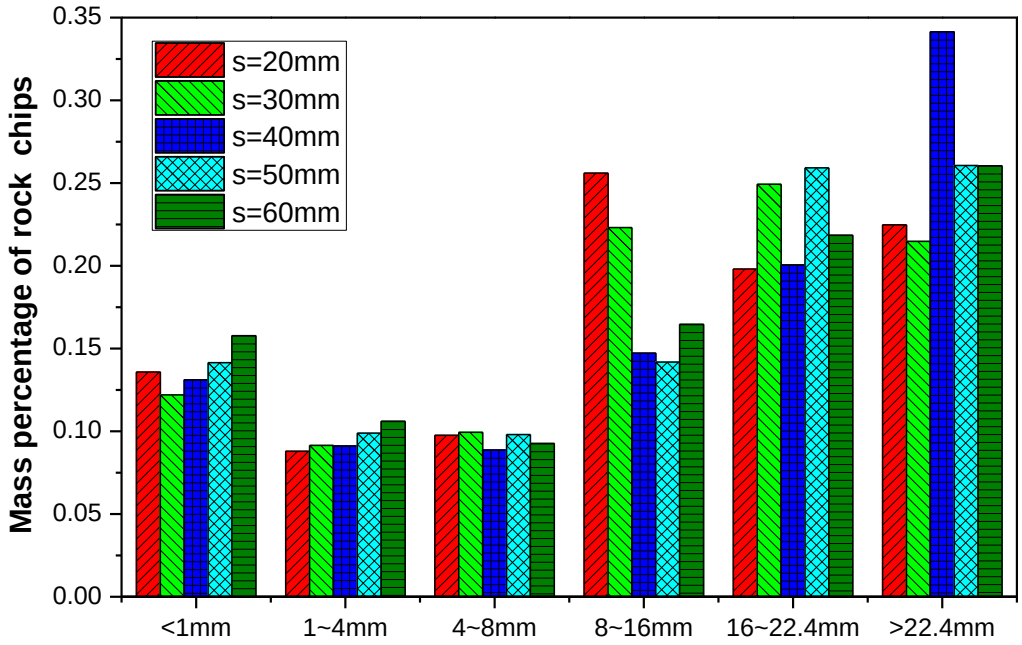

Figure 6.7 Chip size distribution under different spacing

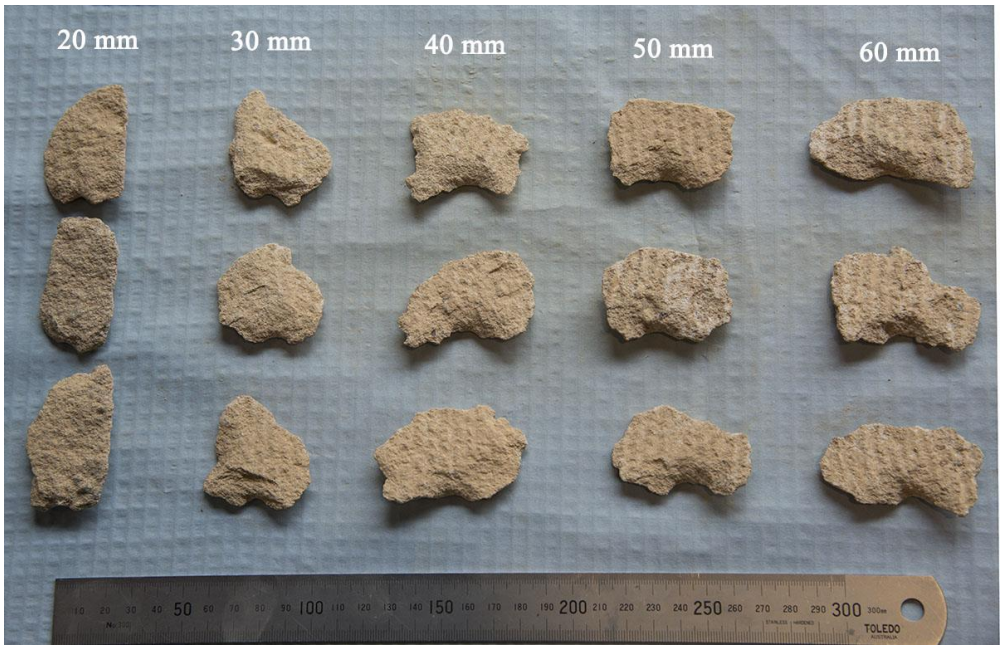

Figure 6.8 Morphology of the typical chip sets at different spacing

6.3.3 Effect of cutting speed

Rock cutting tests were also conducted at cutting speeds of 0.5 m/s, 1 m/s, 1.5 m/s, 2 m/s and 2.5 m/s when the depth of cut and spacing were kept as a constant (10 mm and 50 mm respectively). The mass percentage of rock chips at these various cutting speeds and the histogram are shown in Figure 6.9. The fraction of fine grains with the chips size less than 1 mm increased gradually from 12% to 17% as the cutting speed increased from 0.5 m/s to 2.5 m/s. There was also a slight increase of chip mass percentage at the sets of size of 1~4 mm, 4~8 mm, and 8~16 mm with the increase of cutting speed.

For cutting speed of 0.5 m/s, the proportion of large chips with the chip size above 22.4 mm was almost 50%. It decreased rapidly to 23% when the cutting speed changed to 2.5 m/s. However, it was shown in Figure 6.10 that no major difference was found between the chip sizes at different cutting speeds.

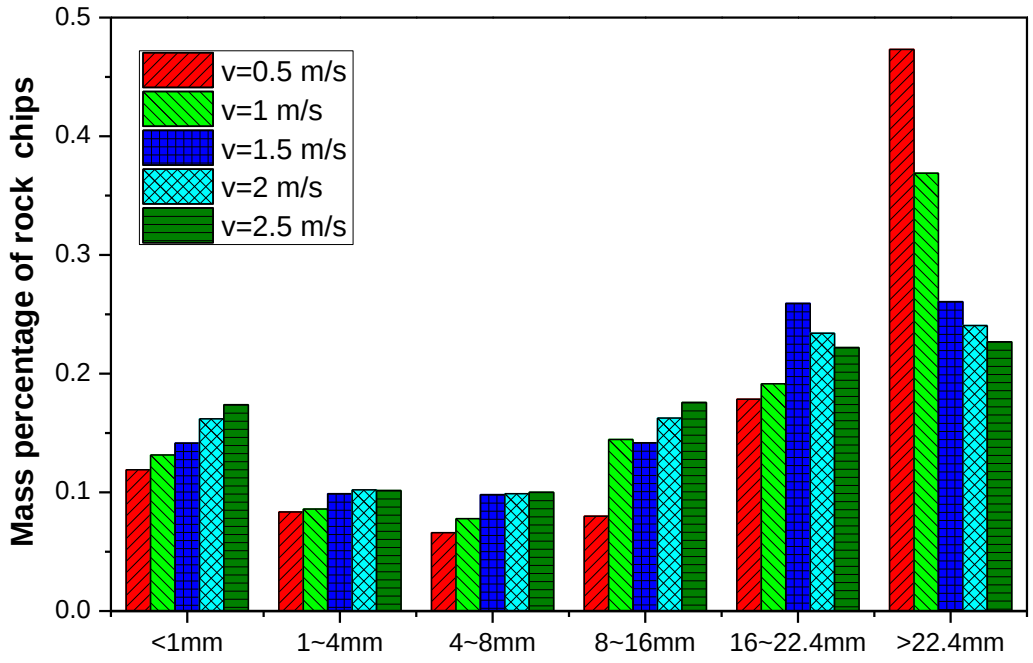

Figure 6.9 Chip size distribution under different cutting speeds

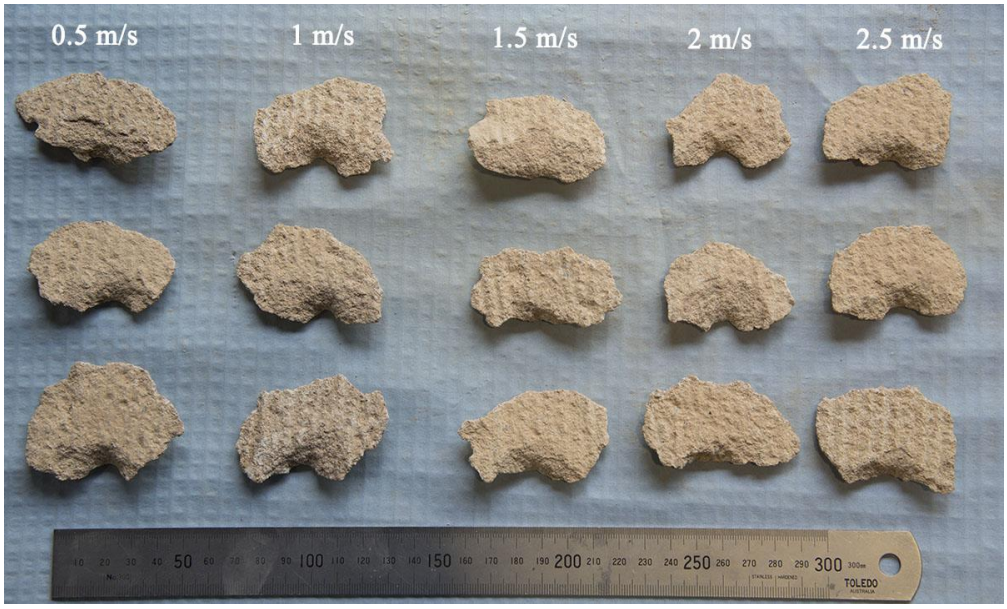

Figure 6.10 Morphology of the typical chip sets at different cutting speeds

6.4 Specific energy

Inyang [53] conducted an analysis of the drag bit cutting parameters such as bit geometry, forces and specific energy. It was concluded that specific energy was the most comprehensive criterion for assessing the efficiency of mechanical excavators. The instantaneous cutting rate of any mechanical excavator can be determined from its optimal specific energy (SE_{opt}) and cutting power (P) [182]:

$$ICR = k_1 \frac{P}{SE_{opt}} \tag{6.1}$$

where ICR denotes the instantaneous cutting rate and k_1 is a constant correlating to the efficiency of the total excavation system. It can be seen from Eq. (6.1) that instantaneous cutting rate follows a reverse trend to specific energy.

The total energy expenditure in a full-scale linear rock cutting test can be computed by integrating the cutting force over the cutting distance. The work done per unit volume of rock

cut (specific energy) is then calculated by dividing the total external work by the volume of rock debris produced. It can be expressed in several ways.

The theoretical cutting volume has usually been used to determine the specific energy:

$$SE = \frac{MCF \times l}{s \times d \times l} \tag{6.2}$$

where SE is the specific energy, MCF is the mean cutting force, l is the cutting length, s is the spacing and d is the depth of cut. This calculation is reasonable only when the rock between two adjacent cutting grooves are completely eliminated and no ridge is formed [183].

By weighing the mass of chips after each cut, specific energy can be formulated as in Eq. (6.3):

$$SE = \frac{MCF \times l \times \rho}{m} \tag{6.3}$$

where ρ is the density of rock, and m is the mass of chips. This "weigh method" could be the most accurate method if all the rock debris produced during each cut can be collected.

In addition, a photogrammetric approach can also be employed to determine the cutting volume and subsequently calculate the specific energy. However, the accuracy of this method is determined by the accuracy of the three dimensional surface model that is developed through the non-contact photography.

The chips under different cutting conditions have been weighed in Section 6.3. The cutting force was also recorded continuously during each cutting test. Thus in this section, the weight method was used to further investigate the effects of DOC, spacing and cutting speed on the specific energy of TSDC tipped picks.

6.4.1 Effect of depth of cut

Pick cutting performance is dominantly affected by depth of cut. In this section, a wide range of depths of cut from 6 mm to 18 mm was selected to investigate the influence of DOC on specific energy, in which the cutting speed, spacing and attack angle were kept as the constants (1.5 m/s, 50 mm and 55^o respectively). Figure 6.11 shows the variation of specific energy with a change of DOC. It was observed that the increase of DOC caused a dramatic

decrease of specific energy. However, the slope of specific energy curve declined gradually, which means an optimal depth of cut can be obtained when the specific energy decreases to a certain level. This variation of specific energy is probably due to the formation of larger rock chips leading to more effective fragmentation at the greater DOC.

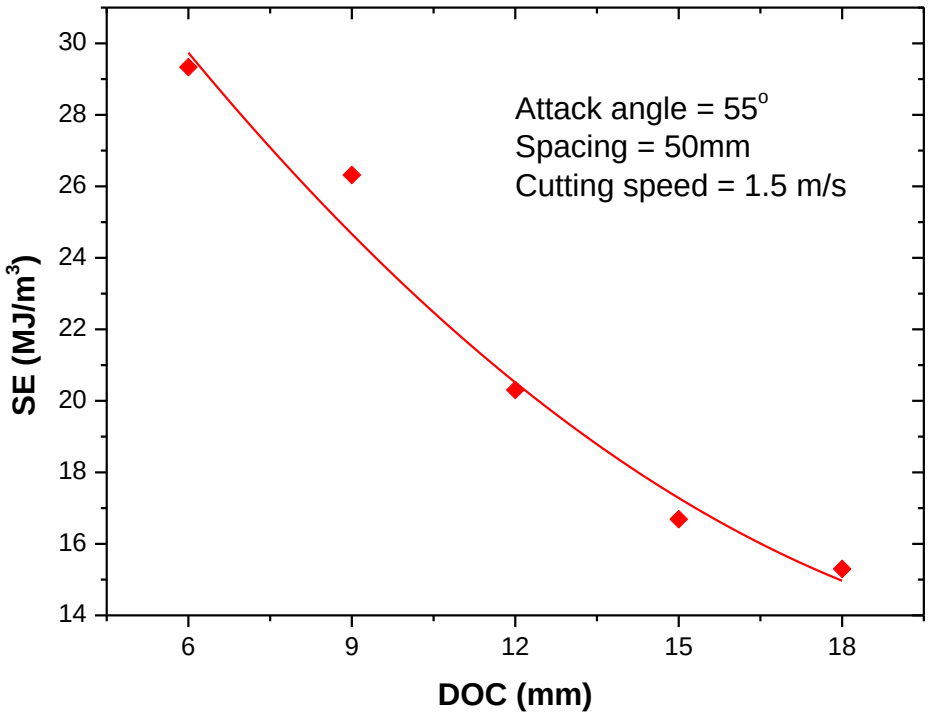

Figure 6.11 Effect of depth of cut on specific energy

6.4.2 Effect of spacing

When the depth of cut, cutting speed and attack angle were fixed at 10 mm, 1.5 m/s and 55° respectively, the influence of spacing between adjacent cuts on specific energy was evaluated in the spacing range of 20 mm to 60 mm. The variation of specific energy at various spacing is illustrated in Figure 6.12. According to Figure 6.12, the increase of spacing resulted in an increase of specific energy in a general trend. The dependence of the specific energy on spacing was more obvious for the increase from 20 mm to 40 mm. It increased about 62.8% from 14.0 MJ/m^3 to 22.7 MJ/m^3 in this spacing range. When the spacing was over 40 mm, however, there was only a slightly increase of about 4.7% from 22.7 MJ/m^3 to 23.8 MJ/m^3 when the spacing increased to 60 mm. The possible reason that would account for this was the difference in cutting mode. If the spacing was small and the spacing to depth of cut ratio

was somehow close to the optimal ratio, the cracks between the adjoining cuts would interact and the rock between these cuts would effectively broke out. This means more effective and economic cutting happened when the spacing was close to the optimal spacing. As the spacing increased, the cutting mode would change from relieved to unrelieved cutting, resulting in the loss of interaction between the adjoining cuts and the formation of isolated ridge between the adjoining cuts. This would lead to "hard" and uneconomic cutting, thereby decreasing the cutting efficiency. Moreover, pick forces and rock volumes removed from the rock surface would not change if totally unrelieved cutting happens. That would explain why there was only a slight variation of the specific energy for spacing greater than 40 mm.

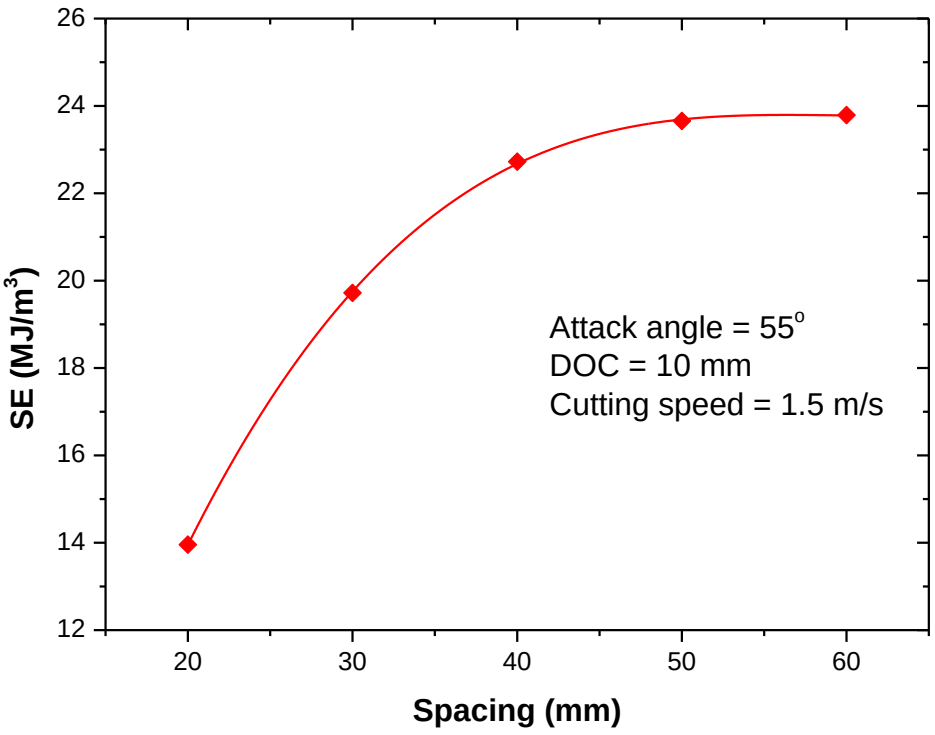

Figure 6.12 Effect of spacing on specific energy

6.4.3 Effect of cutting speed

An examination of the relationship between the specific energy and cutting speed is shown in Figure 6.13, in which the depth of cut, spacing and attack angle were set as 10 mm, 50 mm and 55° respectively. As can be seen from Figure 6.13, the specific energy increased continuously from 20.8 MJ/m^3 to 31.1 MJ/m^3 as the cutting speed increased from 0.5 m/s to 2.5 m/s. This variation might be attributed to the cutting force required to fragment the rock

debris was higher at higher cutting speed (see Figure 4.8), which means more external work needs to be consumed at higher cutting speed during the rock cutting process. As observed in Section 6.3, the size of rock debris below 1 mm increased with the increasing of cutting speed, and the proportion of large chips with the chip size above 22.4 decreased rapidly with the cutting speed, which means more efficient fragmentation of rock occurred, less dust and more large chips were generated at low cutting speed. Thus, the generation of fewer large rock debris and more respirable dust at high cutting speed might be another reason account for the increase of specific energy.

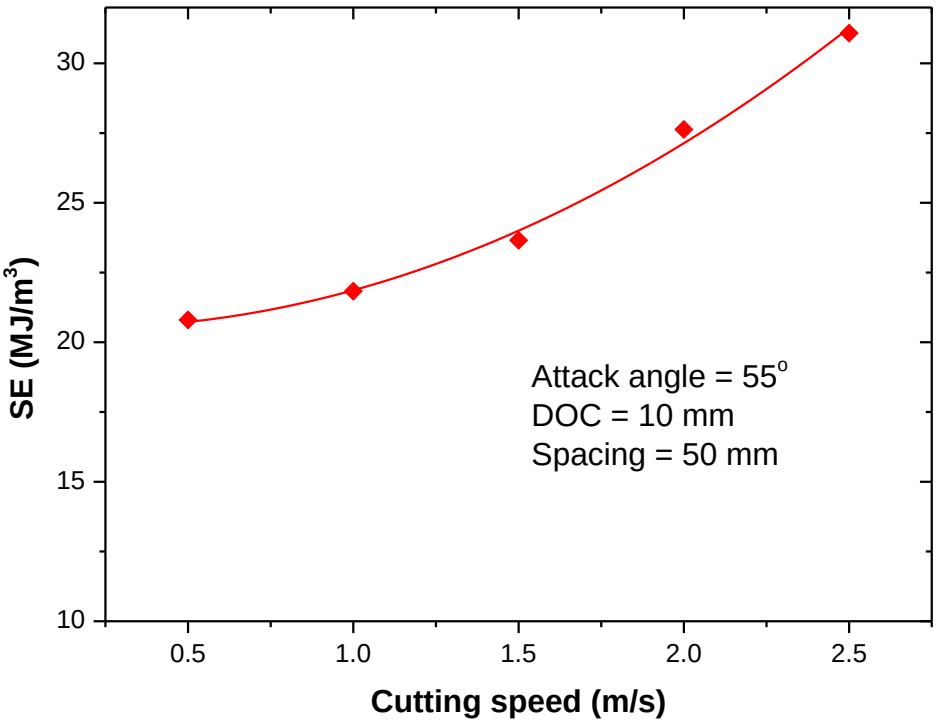

Figure 6.13 Effect of cutting speed on specific energy

6.5 Concluding remarks

A series of full-scale linear rock cutting tests was conducted to identify and quantify the effects of different rock cutting parameters on the chip size distribution. From the mean S/N ratio, the optimal parametric combination for maximizing the coarseness index was: attack angle of 45^{o}, DOC of 18 mm, spacing of 72 mm, and cutting speed 0.5 m/s. From the

ANOVA analysis, DOC was found to be the most influential factor for coarseness index. Attack angle had the least effect on coarseness index.

Then the effects of depth of cut, cutting speed and spacing which have relatively greater contributions to the coarseness index were chosen to further analyse the rock chip size distribution. It was found that the dust proportion decreased with the depth of cut, while the large-sized chips increased with the depth of cut. Chips produced at small depths of cut were mostly distributed within the small sizes. However, chips at larger depths of cut were mainly distributed in larger sizes. Moreover, the size of chips also increased significantly with the increase of depth of cut. The dust proportion decreased a little bit when the spacing increased from 20 mm to 30 mm, then increased slightly with a further increase of spacing. Chips mostly distributed on size large than 8 mm for all the spacing. The width of the chips increased gradually with the increase of spacing. The fraction of fine grains increased gradually with the cutting speed. For cutting speed of 0.5 m/s, the proportion of large chips was dominant. It decreased rapidly when the cutting speed increased to 2.5 m/s. However, no major difference was found between the chip sizes at different cutting speeds.

Finally, the "weigh method" was used to investigate the cutting specific energy of TSDC tipped picks under different DOC, spacing and cutting speed. It was found that the specific cutting energy increased with the increased cutting speed and spacing, while it decreased and then approached a saturated value with increasing depth of cut.

7

Numerical simulation of rock cutting process

7.1 Introduction

Over the years, various methods including full-scale linear cutting test, small-scale cutting test (core cutting), analytical or empirical models, and numerical methods have been used to understand fragmentation mechanism and assess cutter performance. Among these methods, the full-scale laboratory rock cutting test has proven to be the most accepted, reliable and precise approach to understand the interactions between cutting tools and rock [41, 42, 79, 183]. The test results (i.e., the cutting force, normal force, lateral/sideways force, specific energy, and breakout pattern) under different experimental conditions and cutting scenarios can be confidently used as inputs to computer models/software to estimate the overall reaction forces, torque, power requirement, cutting specific energy and production rate of the excavation machine. However, the full-scale linear rock cutting test is a costly and time consuming process, and requires large blocks of rocks, experienced personnel and expensive test rigs that can only be found in a few research centers in the world [41]. Therefore, alternative ways such as small-scale cutting test (or core cutting), analytical or empirical models might be applied when a full-scale linear rock cutting rig is inaccessible.

During the past few years, numerical modelling has emerged as an easier and faster technique to investigate the rock-tool interaction problems. It offers the advantages of yielding a great number of results in a short period, and sometimes providing useful insight into different stages of the rock fragmentation process. Thus, the numerical simulation can be the most efficient and economical approach if a perfect model is developed.

In this chapter, a series of three dimensional numerical rock cutting tests was performed by using a commercial finite element code, LS-DYNA. The forces acting on the tip of pick and the volumes removed from the rock were continuously recorded during the tests. The numerical results including cutting forces and specific energy under different cutting conditions were analysed and compared with those of the experimental tests with the same cutting parameters. Moreover, the cutting forces acting on the pick were analytically calculated.

7.2 Numerical simulation methods

As mentioned in Section 7.1, the laboratory rock cutting tests are usually costly, time consuming and it is hard to obtain useful visualization of rock breakage or fragmentation process. Therefore numerical modelling has emerged as an easier and faster technique to investigate the rock-tool interactions. However, such simulations remain an extremely challenging task. The challenges consist of a series of complicated problems such as (a) the anisotropic, (b) inhomogeneous and (c) non-elastic nature of deformation of the material and the highly nonlinear nature of the process. The contact problem first arises as soon as the tip of the cutter encounters the target material (i.e. rock), followed by the uncertainty of the occurrence of the rock failure. Finally, after the element fails the difficulty of how to initiate the rock breakage process needs to be tackled until the new cycle starts again [184].

Despite these above-mentioned difficulties in numerical modelling, a considerable effort has been made to simulate the rock fragmentation mechanism. The finite element method (FEM), finite difference method (FDM), discrete element method (DEM) and boundary element method (BEM) were the most widely used simulation packages using for modelling of rock-tool interactions. A throughout literature survey of these numerical approaches that are used in rock cutting simulations were outlined in section 2.6, and not repeated here.

It is revealed that the DEM and FEM are the most popular methods for modelling tool-rock interaction problems. The discrete element model is capable of providing valuable information of the key phenomena in a rock cutting process. The micro level and discrete nature of the particles in DEM are the major disadvantages that limit it in rock cutting. As for the FEM technique, the ‘smeared crack’ based FEM is not able to model the dynamic fragmentation process. The explicit FEM code LS-DYNA, on the other hand, is capable of capturing the crack initiation, crack propagation and dynamic fragmentation and therefore used in this study.

7.3 Rock material models

The implementation of a reliable and efficient constitutive model is a persistent challenge in simulating the rock cutting processes with numerical continuum methods. Fortunately, there is a good number (over two hundred) material models, each assigned a unique number, are be

implemented in LS-DYNA. LS-DYNA also contains a wide range of material libraries for concrete and geo-materials. However, many aspects need to be taken into account to select a rational constitutive model for a particular simulation problem, including boundary and loading conditions, confining pressures, the scale of the problem, the time period involved, and the sets of experimental data and observations available for the application or material [185].

Among the various material models, the Inviscid Two Invariant Geologic Cap Model (MAT 25), the Concrete Damage Model (MAT 72), the Johnson-Holmquist Model (MAT 111), and the Continuous Surface Cap Model (MAT 159) are considered as the potential models in simulating the damage and fracture process of rock or rock-like materials in LS-DYNA [186]. Generally, one major limitation of the Geologic Cap model is that it diverges dramatically from the failure and compaction surfaces rapidly, which would result in erroneous results or termination of the calculation [187]. The Johnson-Holmquist model is superior in modelling compression damage in the destruction of material, while tensile damage is not well represented in this model. The Concrete Damage Model, on the other hand, is a comprehensive model in characterizing the rock behaviour under various stress conditions. However, numerous parameters need to be provided as an input by the user, which are hard to find in the literature due to proprietary or security reasons.

In addition, element erosion, which could help to initiate the failure crack and eventually aid in the formation of rock chips, is not contemplated in any of the formulation of these three material models. Therefore, the ADD_EROSION in LS-DYNA needs to be defined to allow the deletion of the element from the rock continuum once any of the failure/erosion criterion (or a combination of criteria) is satisfied. Unfortunately, it is concluded that the implementation of those three material models is limited due to the impossibility to determine a specific erosion criterion for the deletion of elements.

With the robust theoretical basis and unique incorporation of element erosion within the material constitutive damage model, the Continuous Surface Cap Model (CSCM) appears to be the most suitable model in the LS-DYNA material library for the simulation of rock cutting problems in this study.

7.3.1 Basic principles of CSCM model

The Continuous Surface Cap Model, a comprehensive elasto-plastic damage model, was originally developed and implemented into LS-DYNA by the U.S. Department of Transportation as an analysis tool to simulate the dynamic performance of concrete in roadside safety structures such as bridge decks, guardrails and safety barriers collided by vehicles [188]. A thorough description of the theory and formulation of this model has been provided by Murray [189], only a brief summary of the main features are described here.

As shown in Figure 7.1, the yield surface of CSCM includes a shear failure surface and a moveable hardening cap, with a smooth intersection between them. The main characteristics of CSCM are: (a) isotropic constitutive equations, (b) three stress invariant yield surface and a moveable hardening cap, (c) damage based strain softening with erosion and modulus degradation, (d) rate effects for increasing strength with high strain rate [188].

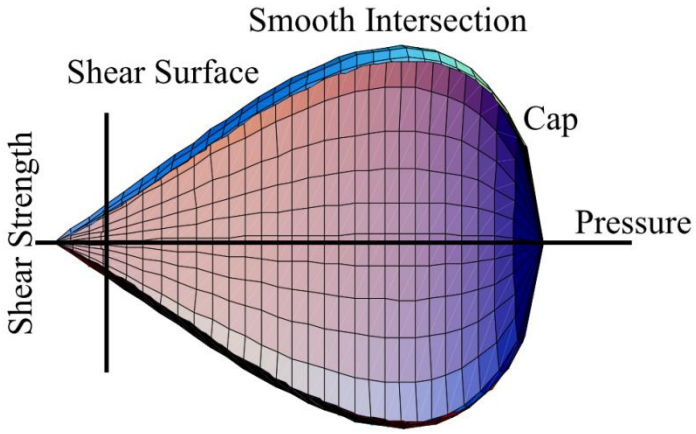

Figure 7.1 Yield surface of the continuous surface cap model in two dimensions [189]

Unlike the Geologic Cap Model which is developed as a function of two stress invariants, the formulation of the yield surface in CSCM is extended to three stress invariants, I_1, J_2 and J_3 (the first, second and third invariant of the stress tensor). Based on these three stress invariant, the failure surface shown in Figure 7.7 can be described as [189]:

$$f(I_1, J_2, J_3, \kappa) = J_2 - \Re^2 F_c' F_f^{\,2} \tag{7.1}$$

where κ is the cap hardening parameter, $\Re$ is the Rubin scale function, F_f is the shear failure and F_c' is the hardening cap. An exponential function in terms of the first invariant of the stress tensor is used to define the shear failure surface [189]:

$$F_f(I_1) = \alpha_1 - \lambda \exp^{-\beta_1 I_1} + \theta_1 I_1 \tag{7.2}$$

where the parameters of α_1, λ, β_1, and θ_1 are estimated by fitting the model surface to the strength measurements from laboratory tri-axial compression (TXC) tests conducted on plain rock cylinders.

7.3.2 Damage accumulation

Two distinct damage modes - namely brittle damage and ductile damage - are incorporated into CSCM to describe the damage accumulation. Ductile damage accumulates when the pressure is compressive and the damage energy threshold τ_{c0} is exceeded, and the brittle damage accumulates when the pressure is tensile and the damage energy threshold τ_{t0} is exceeded. The strain energy terms τ_c *and* τ_t for ductile and brittle damage accumulation are defined as follows [190]:

$$\tau_c = \sqrt{\frac{1}{2}\sigma_{ij}\varepsilon_{ij}} \tag{7.3}$$

$$\tau_t = \sqrt{E\varepsilon_{\max}{}^2} \tag{7.4}$$

where σ_{ij} *and* ε_{ij} are the stress and strain components, E is the elastic Young's modulus and $\varepsilon_{\max}$ is the maximum principal strain.

With the accumulation of the damage, the damage parameter d grows from 0 (undamaged material) to 1 (totally damaged material) according to the following functions [190].

For ductile damage:

$$d(\tau_c) = \frac{d_{\max}}{B}\left[\frac{1+B}{1+B\exp^{-A(\tau_c-\tau_{c0})}} - 1\right] \tag{7.5}$$

For brittle damage:

$$d(\tau_t) = \frac{0.999}{D_1}\left[\frac{1+D_1}{1+D_1\exp^{-C(\tau_t-\tau_{t0})}}-1\right] \tag{7.6}$$

The parameters A *and* B in Eq. (7.5) or C *and* D_1 in Eq. (7.6) set the shape of the softening in stress-displacement or stress-strain curve. The parameter $d_{\max}$ in Eq. (7.5) is the maximum damage level that can be attained.

7.4 Methodology

To numerically simulate the rock cutting process and the associated fragmentation as occurred in the experiments, a set of rock cutting tests under a wide range of depths of cut, attack angles, and cutting speeds were carried out using the explicit FEM software package LS-DYNA.

7.4.1 Model geometry and mesh generation

In the simulation, a conical (point attack) pick and a rock slab were considered for modelling the three dimensional groove cutting. The base rock slab was modelled as a rectangular block, representing the Helidon sandstone used in this work. The rock material was modelled with the continuous surface cap model MAT_159, which was discussed in the previous sections. The conical pick was assumed as a rigid body and thus MAT_20 in LS-DYNA was selected as the cutter material.

The model inputs corresponding to the same properties of the pick and rock obtained from the laboratory are listed in Tables 7.1 and 7.2. Three dimensional hexahedron solid elements are implemented for both the conical pick and the rock block. Generally, the element size throughout the cutting area should be as small as the actual particle size in the sandstone, but this must be compromised due to the computational costs, especially when the depth of cut is quite large. The rock slab in the simulation was divided into two parts. The upper part, where the fragmentation would take place and large deformation would occur, was modelled with a fine mesh. The mesh of the lower part where almost no deformation would occur is much coarser. Figure 7.2 shows the details about the geometry and set up of the model (L_x, L_y and

L_z represent the dimensions of the rock slab), and Table 7.3 summarises all the cutting variables and the dimensions of the rock models.

Table 7.1 The properties of the conical pick

Density (ρ) kg/m^3	Young's modulus (E) (GPa)	Poisson's ratio (ν)
15000	630	0.22

Table 7.2 The properties of the rock sample

Young's modulus	Poisson's ratio	Shear modulus	Bulk modulus	Density	Uniaxial compressive strength	Brazilian tensile strength
E (GPa)	ν	G (GPa)	K (GPa)	ρ (g/cm^3)	σ_c (MPa)	σ_t (MPa)
25.5	0.15	11.09	12.14	2.28	57	5.8

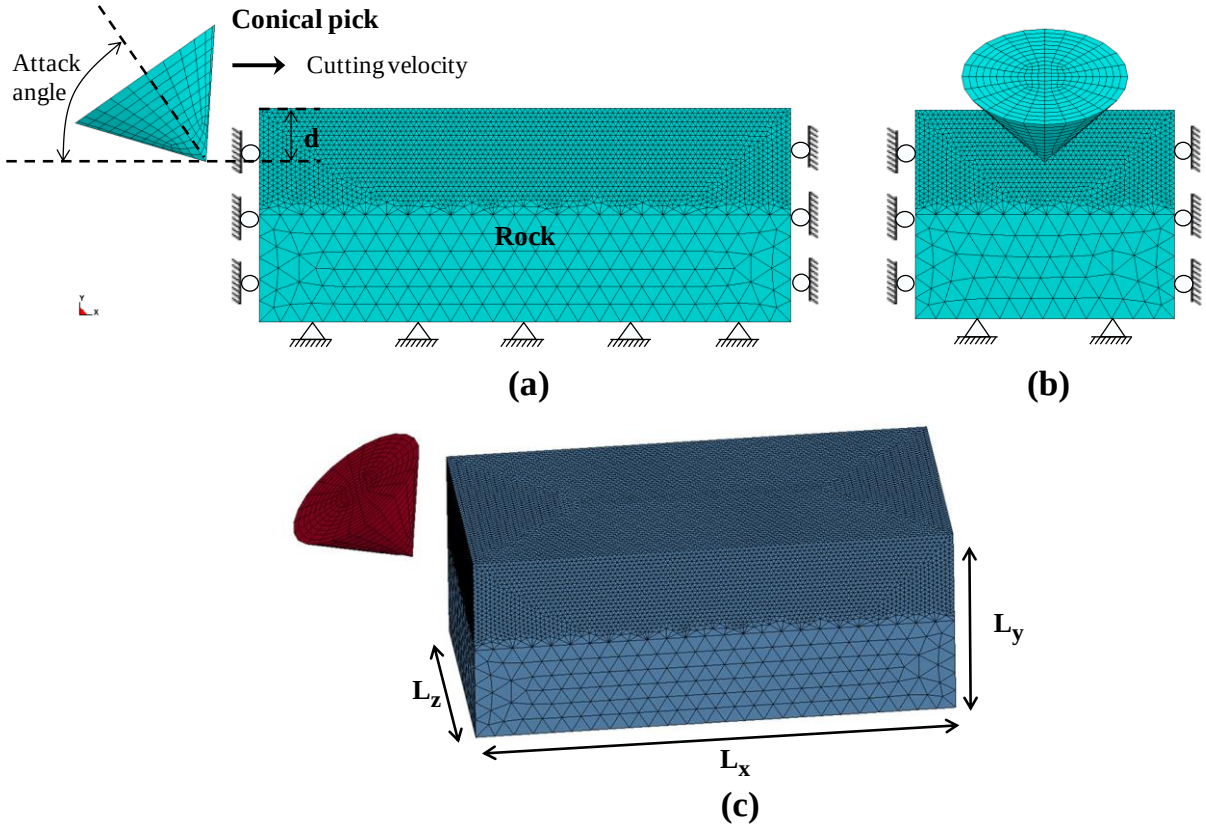

Figure 7.2 The 3D FEM model with meshes and boundary conditions: (a) side view; (b) front view of the FEM model; and (c) oblique view

Table 7.3 Cutting parameters and dimensional information of the rock models

Model ID	DOC	Attack angle	Cutting speed	L_x	L_y	L_z
	d (mm)	α (°)	v (m/s)	(mm)	(mm)	(mm)
d1α3v3	3	55	1.5	30	10	15
d2α3v3	6	55	1.5	60	20	30
d3α3v3	9	55	1.5	90	30	45
d4α3v3	12	55	1.5	120	40	60
d5α3v3	15	55	1.5	150	50	75
d3α1v3	10	45	1.5	100	40	50
d3α2v3	10	50	1.5	100	40	50
d3α3v3	10	55	1.5	100	40	50
d3α4v3	10	60	1.5	100	40	50
d3α5v3	10	65	1.5	100	40	50
d3α3v1	10	55	0.5	100	40	50
d3α3v2	10	55	1	100	40	50
d3α3v3	10	55	1.5	100	40	50
d3α3v4	10	55	2	100	40	50
d3α3v5	10	55	2.5	100	40	50

7.4.2 Boundary conditions

The translational cutting speed of the conical pick was defined as a boundary condition through BOUNDARY_PRESCRIBED_MOTION_RIGID card in LS-DYNA. The translational and rotational degrees of freedom of rock and pick nodes were defined by using a BOUNDAY_SPC_SET card, as shown in Table 7.4.

Table 7.4 Nodal constraints of the FEM models

		Degree of freedoms (1=fixed, 0=free)					
		Translational			Rotational		
		X	Y	Z	X	Y	Z
Rock	Right and left surfaces	1	0	0	0	1	1
	Front and rear surfaces	0	0	1	1	1	0
	Bottom surface	1	1	1	0	0	0
	Top surface	0	0	0	0	0	0
Pick	All nodes	0	1	1	1	1	1

The bottom, right and left surfaces of the rock slab were treated as "non-reflective boundaries", which allows stress waves to be dissipated instead of being reflected, thus the boundary effect did not interfere with the stress state distributions near the edges of the model.

7.4.3 Contact

Accurate definition of the contact between different parts and assemblies is one of the most difficult topics in many large-deformation problems. Proper selection of a contact surface for a given model is also crucial to the prediction capability of the FEM simulations. In LS-DYNA, a contact is defined by identifying what locations (parts, parts sets, and/or node sets) are to be checked for potential penetration of a slave node through a master segment. A search for penetration is made every step. Two distinct algorithms which are referred to as penalty-based contact and constraint-based contact are implemented in LS-DYNA. In the case of a penalty-based contact, normal interface springs are placed between all penetrating nodes and the contact surface [190]. A normal interface force which is proportional to the amount of normal penetration is applied between the slave node and its contact point.

The treatment of the cutter-rock contact was one of the most influential factors for the calculation of contact forces on the cutting tool. The contacts employed in the present study are penalty-based. Among the various available contact types in LS-DYNA, eroding contacts were selected as the solid elements of rock involved in the contact are subject to erosion (element deletion) due to the material failure criteria. The eroding contacts contain logic which allows the contact surface to be updated as exterior elements are deleted. Finally, the contact interface between the cutting tool (i.e. the master part that is a rigid body) and the base rock slab (the slave part that can be deformed) was simulated using CONTACT_ERODING_SURFACE_TO_SURFACE. The static and dynamic coefficients of friction were set as 0.6 and 0.4 respectively. In the simulations, the elements of the rock were eroded once the damage index d_I reached 0.99 and the maximum principal strain ε_1 exceeded 5%. All three force components can be monitored during the numerical simulation.

7.5 Results and discussion

7.5.1 Cutting forces

Figure 7.3(a) shows a snapshot of the rock cutting process in the simulation and Figure 7.3(b) shows the corresponding force histories for the case where DOC = 10 mm, attack angle = 55^{o}, and cutting speed = 1.5 m/s. As can be seen in Figure 7.3(a), a "V" shape groove was formed when the pick cut across the rock surface and the effective strain (Von Mises) reached the maximum at the leading edge of the pick. Cyclic saw-tooth shape force histories of the three force components can be seen in the Figure 7.3(b). The normal force was greater than the cutting force. The magnitude of the side force was negligible compared with those of cutting and normal forces. These results were in good agreement with the experiment. To quantitatively validate the numerical models, the mean cutting forces simulated using different cutting conditions were compared with those of the experimental tests. The mean cutting forces acting on the conical pick were also analytically calculated according to the most cited theoretical models by Evans [52] and Goktan [39], as suggested in Eqs. (2.12) and (2.15). As recommended by Goktan, the friction angle between the pick and rock was set as 10^{o}.

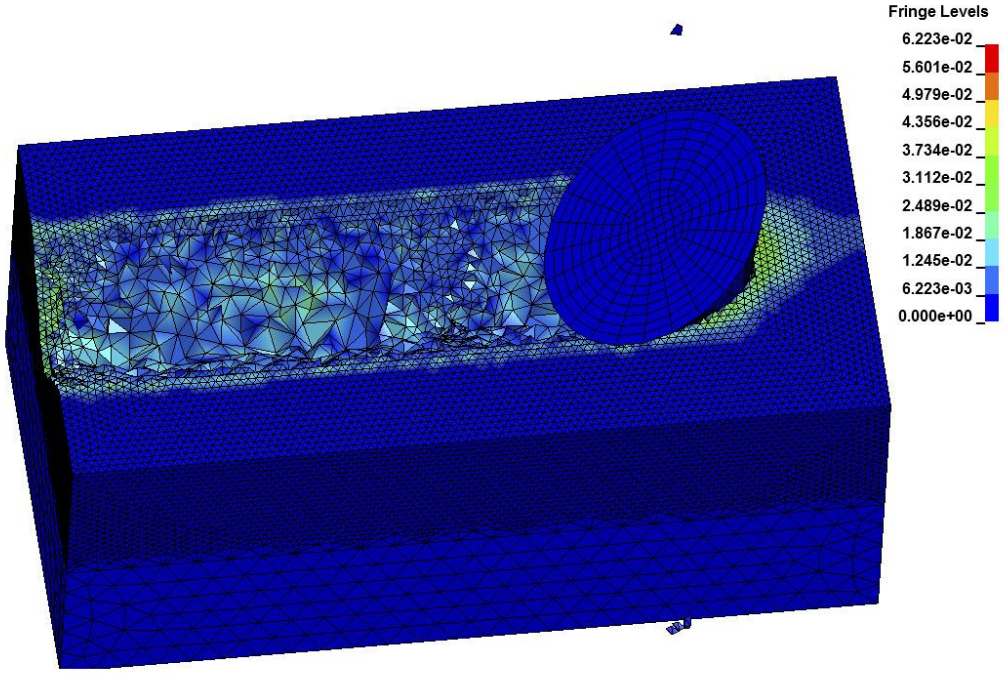

(a)

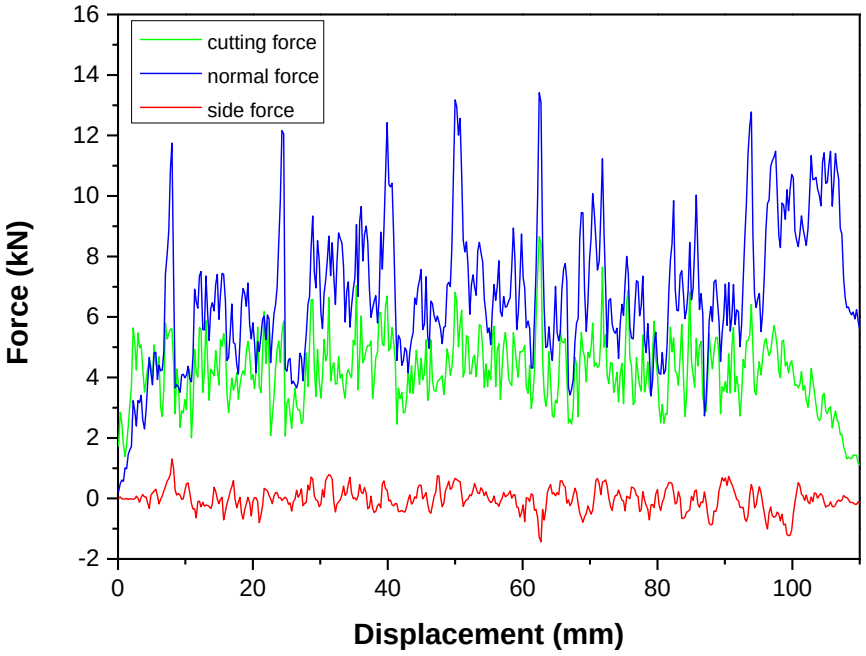

(b)

Figure 7.3 (a) The snapshot of rock cutting; (b) Time histories of the normal, cutting and lateral/side forces with the cutting conditions: d = 10 mm, attack angle = 55^{o} and cutting speed = 1.5 m/s

7.5.1.1 Effect of depth of cut

Numerical rock cutting tests were performed over a wide range of depths of cut from 3 mm to 15 mm. The attack angle and cutting speed were set as 55^{o} and 1.5 m/s respectively. Figure 7.4 shows the cutting forces obtained at various depths of cut. The simulated forces at different depth of cut exhibit similar characteristic, i.e., the forces fluctuate probably due to fictitious phenomena associated with the numerical erosion implementation. The mean values of the simulated cutting forces are compared with the experimental and theoretical cutting forces in Figure 7.5. As shown in Figure 7.5, the simulated, experimental and analytical cutting forces all increase with the increase in depth of cut. The simulated forces agree well with the measured data in both trend and magnitude, although slightly smaller. Linear relationships were found between cutting forces and depth of cut for both simulated and measured data, whereas the cutting force calculated using the Evans's and Goktan's analytical models were proportional to the 2nd power of the depth of cut, which inevitably overestimated the forces especially when the depth of cut was large. Therefore, it should be extremely careful

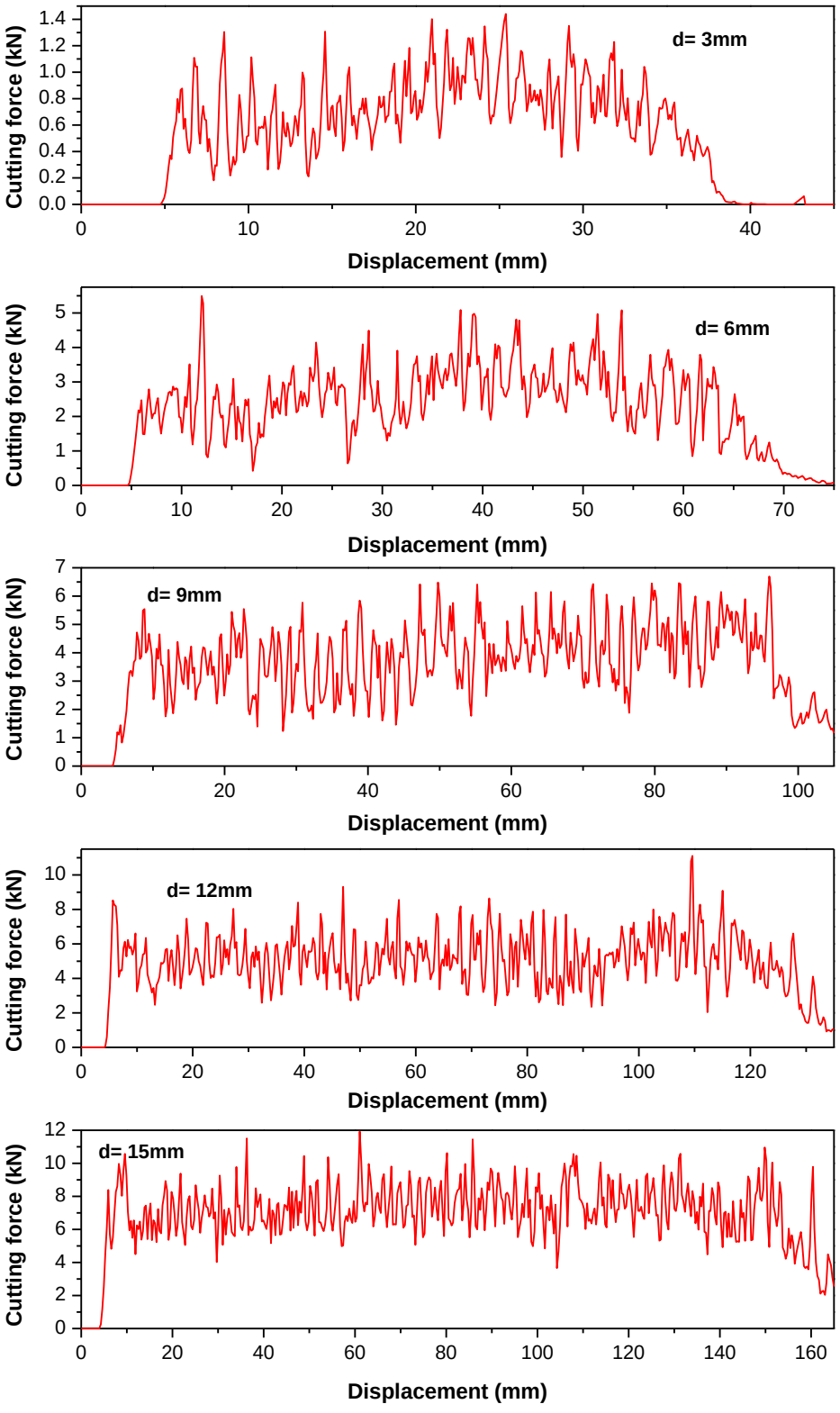

Figure 7.4 The simulated cutting forces under different depths of cut

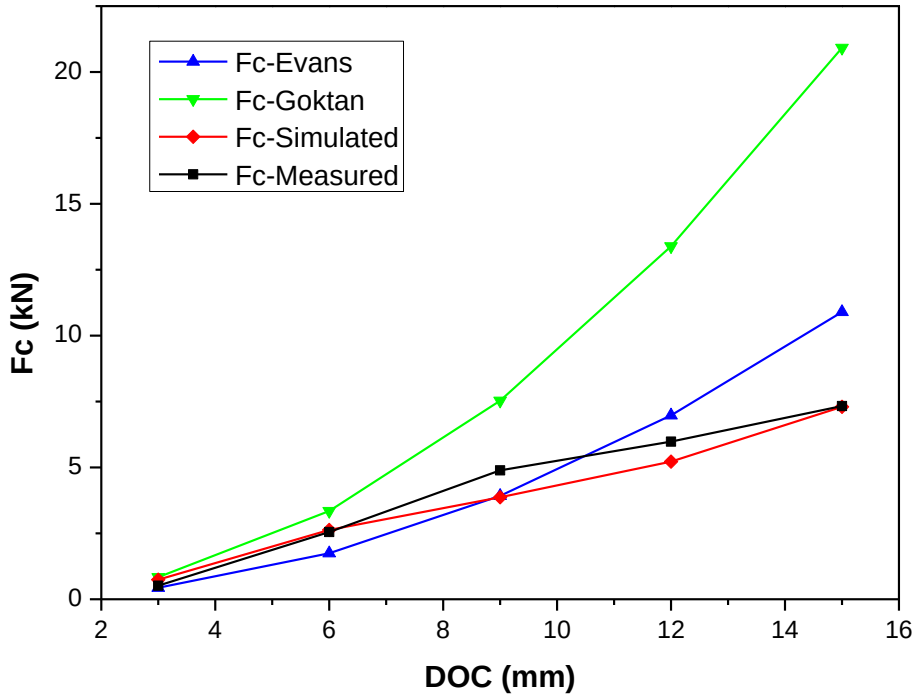

Figure 7.5 Effect of depth of cut on simulated, measured and analytical cutting forces

7.5.1.2 Effect of attack angle

Cutting simulations were also performed at attack angles of 45°, 50°, 55°, 60°, and 65°, while the depth of cut and cutting speed were fixed at 10 mm and 1.5 m/s respectively. As shown in Figure 7.6, the influence of attack angle on the simulated cutting force was not as significant as that of depth of cut. The average values of these force signals were also computed and compared with the experimental and theoretical/analytical cutting forces in Figure 7.7. In general, both the simulated and the measured cutting forces decreased slightly when the attack angle increased. An optimal attack angle was achieved at an angle of 60°, beyond which any increase of attack angle will cause an increase of cutting force. The trend and magnitude of the simulated forces agreed well with the measured. The Evans's model was independent of attack angle because the rock breakage in his model was assumed to be under symmetrical attack, while rake angle was included in Goktan's model. It can be seen from Figure 7.7 that the cutting force calculated using Goktan's model increased with the increase of attack angle, which doesn't agree with the experimental result.

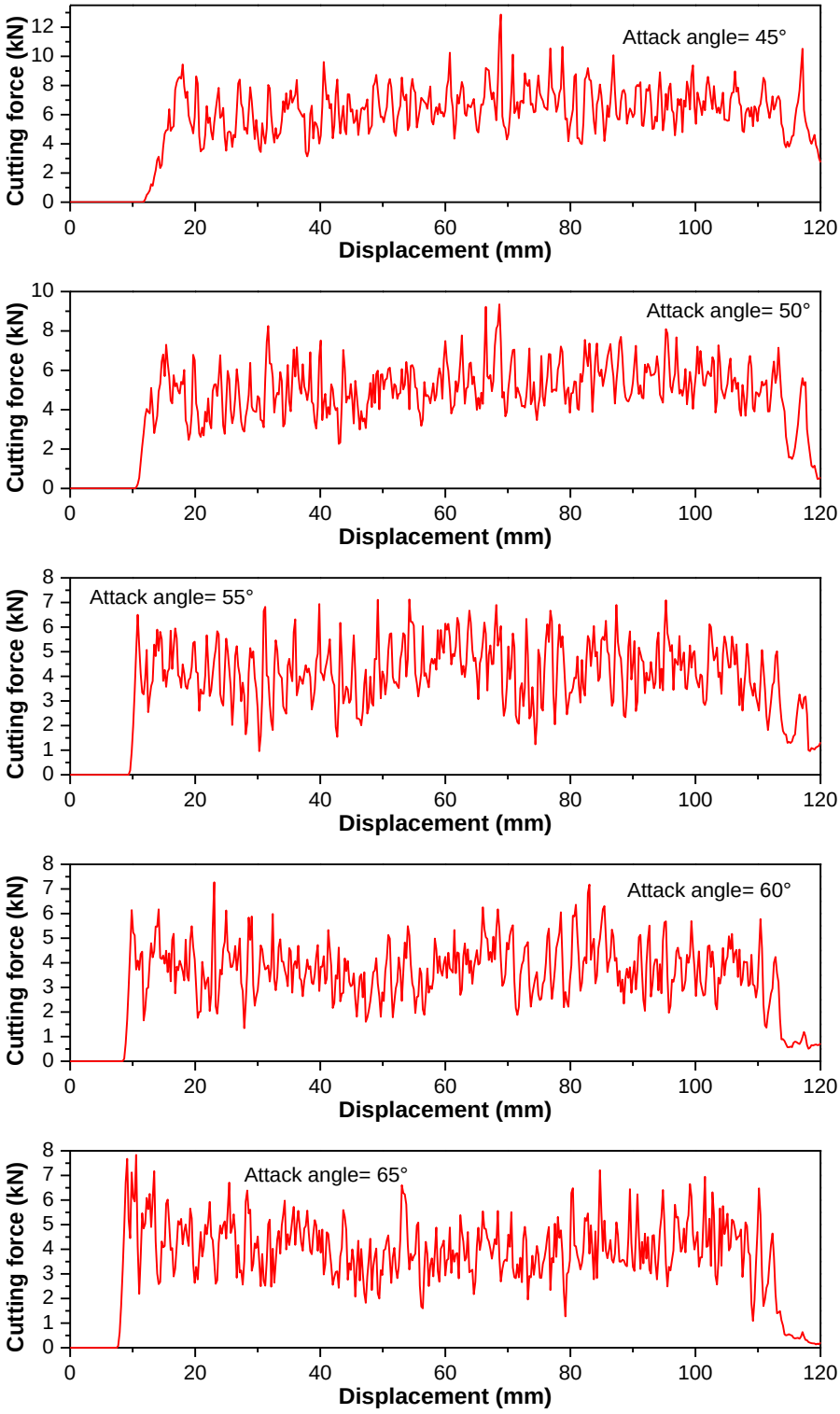

Figure 7.6 The simulated cutting forces under different attack angles

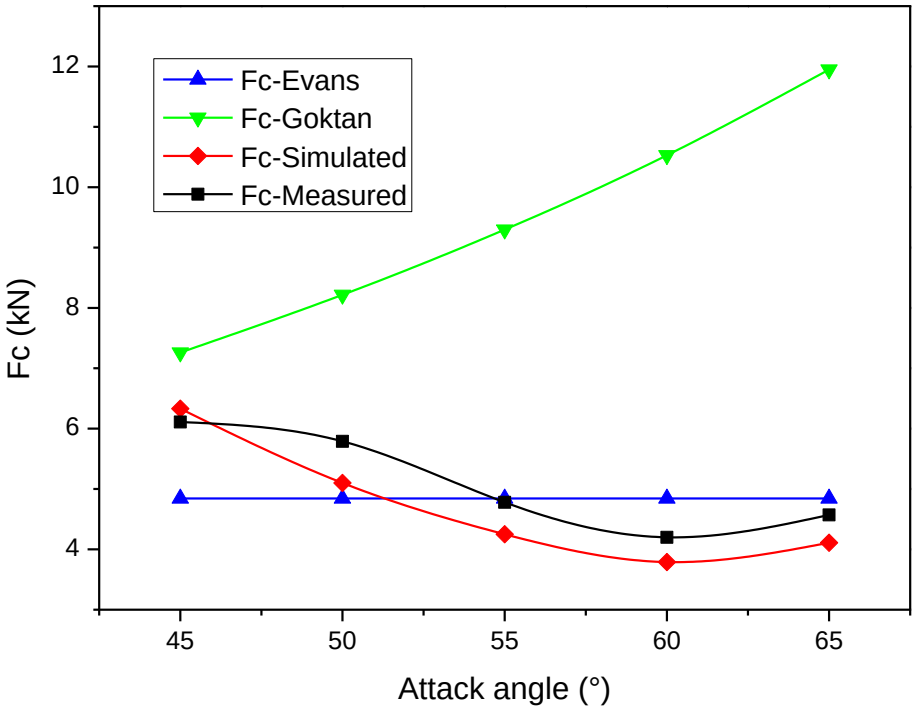

Figure 7.7 Effect of attack angle on simulated, measured and theoretical cutting forces

7.5.1.3 Effect of cutting speed

Rock cutting simulations were conducted at various cutting speeds when the depth of cut and attack angle were 10 mm and 55 ^{o} respectively. As shown in Figure 7.8, the simulated cutting force show similar fluctuations for all the speeds used. Figure 7.9 shows the comparison of simulated, experimental and theoretical/analytical cutting forces. It can be seen that the simulated and measured cutting force increased slightly with the increase in cutting speed, with the higher speed exhibiting greater difference in rate. Simulated values of the cutting force follow the same trend as the measured data, but the magnitudes also differ. Both the cutting forces calculated using Evan's and Goktan's models were unaffected by the cutting speed because of the static nature of their analytical solutions.

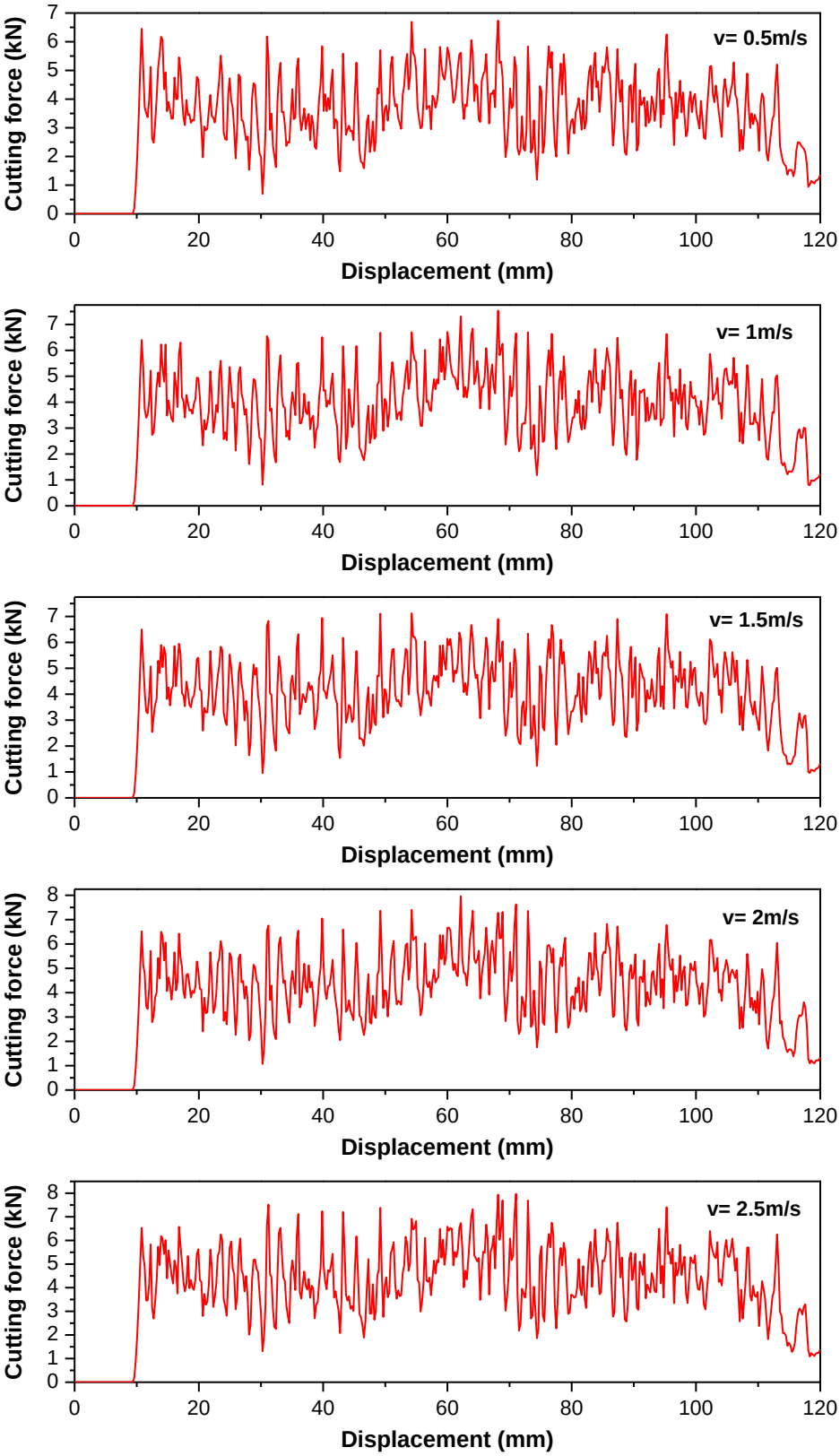

Figure 7.8 The simulated cutting forces under different cutting speeds

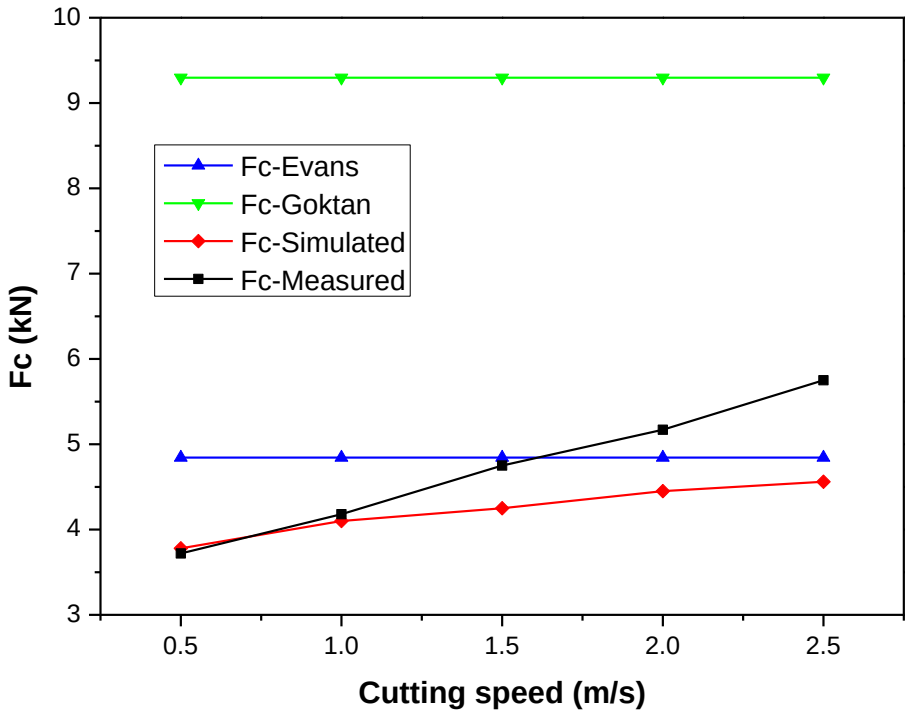

Figure 7.9 Effect of cutting speed on simulated, measured and theoretical cutting forces

All the simulated cutting forces in Figures 7.5, 7.7 and 7.9 are plotted against the measured ones in Figure 7.10. It is seen that there is a strong correlation between them. The coefficient of determination (R^2) of the predicted forces from the numerical models is 0.90, which indicates that the simulation model is quite accurate. The corresponding standard errors of estimate which show the standard deviation of the residuals are 0.42. The analysis of variance of the simulated results gave p-values of 4.2×10^{-8} . This means the relationship was statistically significant. A comparison between simulated and measured values of the cutting forces for all the 15 tests was also shown in Figure 7.11. It is observed that the modelling forces fitted reasonable well with the experimental data. Most of the force values predicted by the numerical model were slightly smaller than that of the measured forces. The reason for this might be that the picks used in the simulations had an exact conical tip and were assumed to be absolutely sharp and rigid during the simulation tests while the commercially manufactured picks in the laboratory tests had a certain rounding of the tip or were subjected to abrasive wear on the tips resulting from the cutting tests.

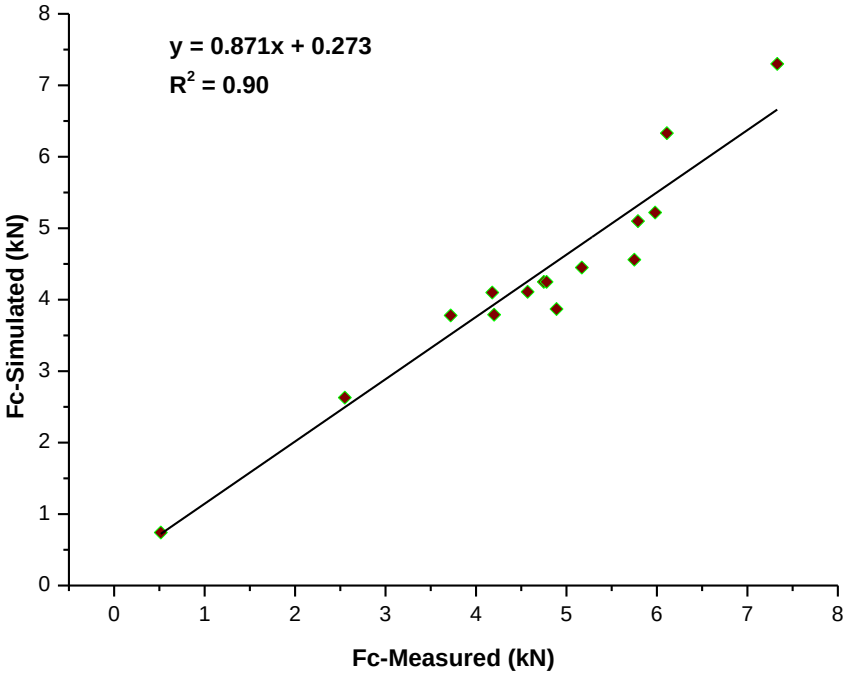

Figure 7.10 Relationship between the simulated and measured cutting forces

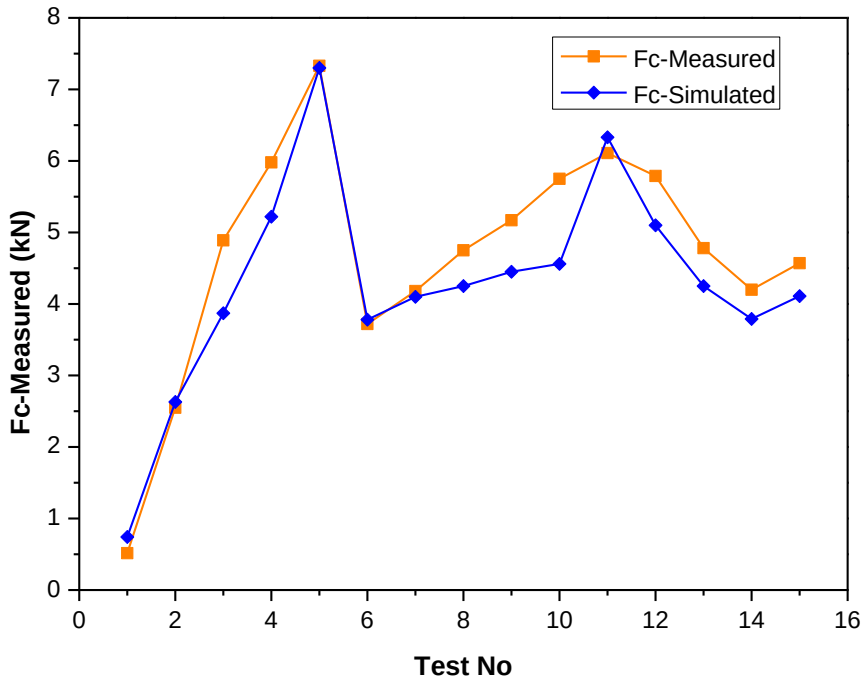

Figure 7.11 Comparison of the simulated and measured cutting forces

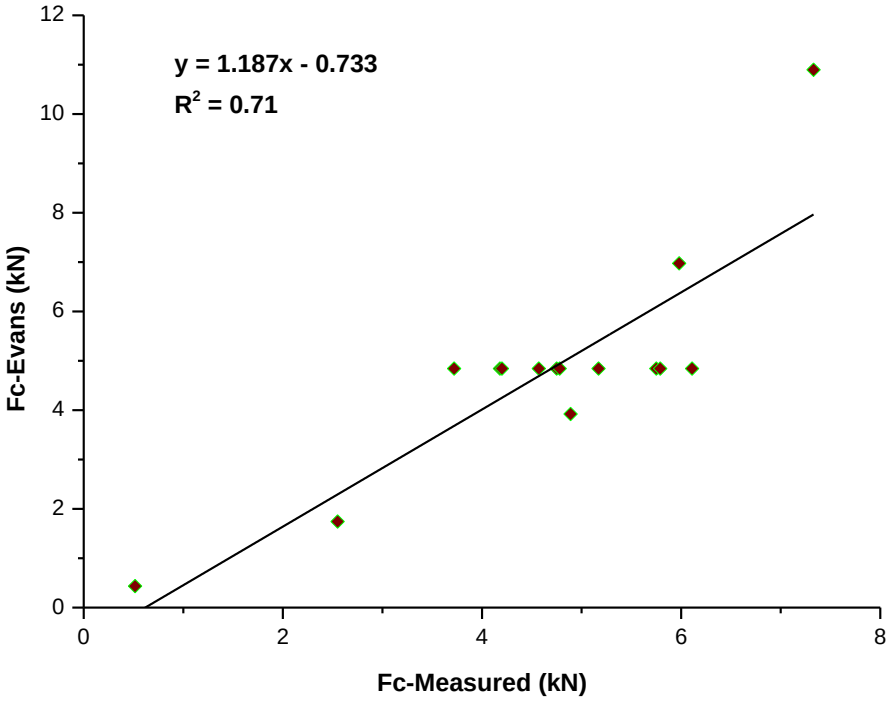

Figure 7.12 Relationship between the Evans's model and measured cutting force

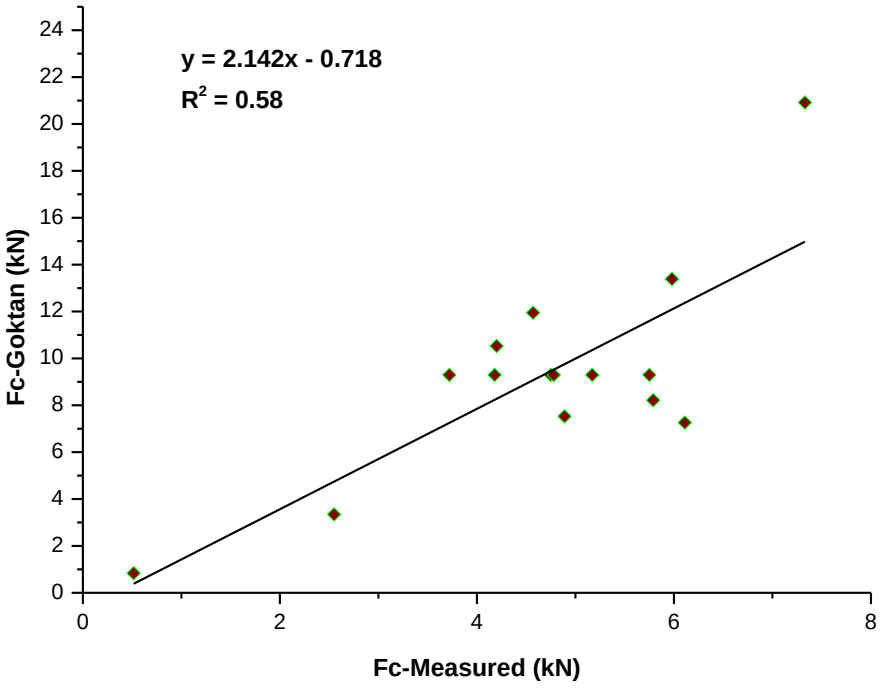

Figure 7.13 Relationship between the Goktan's model and measured cutting force

The relationships between the Evan's and Goktan's analytical models and the experimental data are shown in Figures 7.12 and 7.13. The R^2 values for the correlation of these two models are 0.71 and 0.58 respectively, which is much lower than that of the simulation results. These results further confirm that the cutting force predicted by the analytical solutions must inevitably suffer from the weakness of making major simplifications and inappropriate stress assumption and equilibrium, which may result in errors in cutting force estimations [5]. These results indicate that numerical simulation might serve as an efficient and effective method to predict the cutting forces in rock cutting process, given its strong correlation and good accuracy.

7.5.2 Specific energy (SE)

The specific energy could be determined if the volume of each cut was obtained. Actually, the history of the rock volume fraction that has been eroded during each cutting run can be achieved from one of LS-DYNA's useful outputs. Figure 7.14 shows the effect of depth of cut on the numerical and experimental specific energy, in which the cutting speed and attack angle were 1.5 m/s and 55^o respectively. It can be seen that both the trend and magnitude of the specific energy obtained from numerical tests agree well with the results of the full-scale linear rock cutting tests. The numerical specific energy values were greater at lower depths of cut (i.e. 6 mm and 9 mm) than the measured. The difference between the simulated and the measured energies was small at greater depths of cut. As expected both the numerical and the experimental specific energies decreased with the increase of depth of cut.

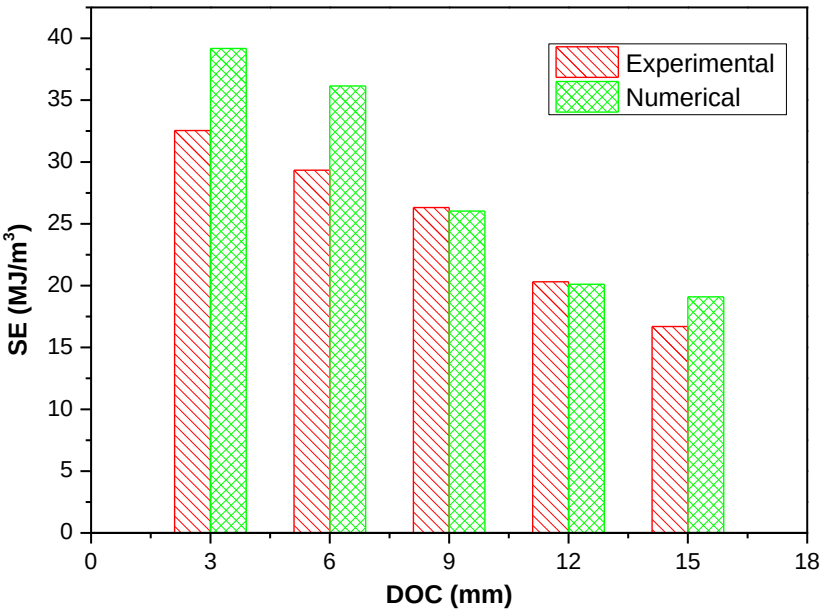

Figure 7.14 Effect of depth of cut on the specific energies

The effect of cutting speed on the specific energy is shown in Figure 7.15 for the fixed depth of cut of 10 mm and attack angle of 55^{o}. Both the numerical and the experimental specific energies increased with the increase in cutting speed, although the increase in the numerical specific energy was not as obvious as that of the experimental one. The numerical specific energy agrees well with the experimental one in both trend and magnitude, although the experimental specific energy was slightly larger than the numerical data. This difference may be attributed to the slightly smaller simulated cutting force. Additionally, the rock debris after each experimental cutting run may not be fully collected.

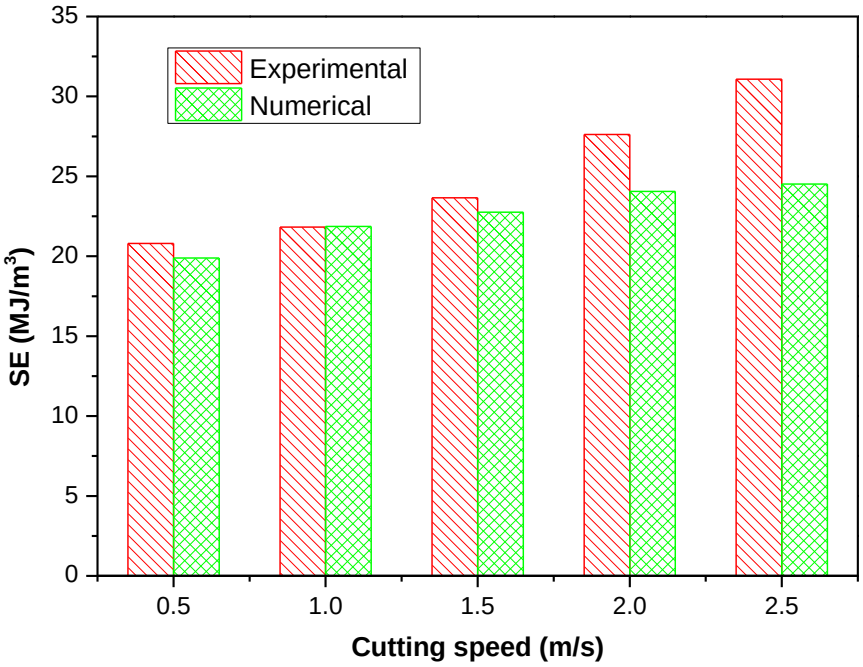

Figure 7.15 Effect of cutting speed on the specific energies

7.6 Concluding remarks

An explicit finite element code, LS-DYNA, was employed to simulate the rock cutting with a point attack pick. In the cutting simulation, a Continuous Surface Cap Model was used to characterize the behaviour of the rock block during the rock cutting process. The numerical models was validated by systematically comparing, the simulated cutting forces the specific energy with the respective experimental results.

The simulated cutting forces were in good agreement with the measured forces, but slightly smaller than the experimental forces. The simulated cutting forces were, in general, consistent with those predicted by the analytical models of Evans and Goktan. However, discrepancy existed because the Evan's model is independent of attack angle and cutting speed and Goktan's model does not include the effect of cutting speed.

Our regression analyses showed that the numerical simulated cutting forces had a strong correlation and better accuracy. The numerical and experimental specific energies also showed good agreement, further confirming the validation of the numerical model.

8

Conclusions and future work

In this work, systematic experimental and numerical studies have been conducted to improve the understanding of rock cutting mechanisms, in particular to get a better insight into the interaction between point attack picks and rock. The point attack picks used in this study included those picks with cemented tungsten carbide (WC) and thermal stable diamond composite (TSDC) tips. The rock cutting process was comprehensively investigated in terms of cutting force, specific energy, pick tip temperature and cutting chips using both experimental and numerical approaches.

8.1 Conclusions

Extensive full scale linear rock cutting tests were undertaken to systematically investigate the cutting forces of the TSDC tipped SMART*CUT picks. Experimental techniques have been developed to measure and analyse the pick cutting temperature at the interface between a pick tip and a rock. The main cutting parameters which have relatively greater contribution to the coarseness index were chosen to analyse rock fragmentation and the specific energy. Three dimensional numerical models were established to compare with the experimental and analytical results and to gain the insights of rock cutting mechanisms. The major contributions and conclusions from these studies are summarised below:

(1) The effects of attack angle, depth of cut, spacing and cutting speed on the cutting performance of TSDC tipped picks was systematically investigated. The tests were performed on the basics of Taguchi's L25 orthogonal array. The optimised rock cutting parameters for minimising the mean cutting, normal bending forces were obtained based on the mean S/N ratio. The optimal parametric combination include the attack angle of 60^{o}, DOC of 6 mm, spacing of 24 mm, and cutting speed of 0.5 m/s, which was achieved based on the minimum cutting and normal forces produced. In terms of the minimisation of the bending force, the optimal parameters included the attack angle of 55^{o}, DOC of 6 mm, spacing of 24 mm, and cutting speed of 1.0 m/s. The ANOVA analysis revealed that attack angle, DOC and spacing were the statistically significant factors influencing the mean cutting force. The most influential factor was DOC, followed by attack angle and spacing. The cutting speed had the least effect. However, for the normal force, all four factors had statistical significance with a significance order of attack angle > DOC > cutting speed > spacing. Although the bending

force is a function of the cutting and normal forces, the influences of the cutting parameters on it were different. Only attack angle and DOC had statistical significance, with an order of attack angle > DOC > spacing > cutting speed.

(2) Empirical models for predicting the mean cutting and normal forces on TSDC tipped picks have been developed based on multiple linear regression (MLR) and artificial neural network (ANN) techniques. The established empirical force models showed good predictive capabilities with acceptable accuracy. The ANN models offered better accuracy and less deviation than the MLR models.

(3) The pick cutting temperature during rock cutting process was measured using infrared imaging and thermocouple techniques. The temperature distribution in the cutting area was initially acquired by using a thermal infrared camera with high capture rates. It was found that the TSDC tipped SMART*CUT picks caused lower pick tip temperature than the conventional WC tipped picks. The maximum temperature around the cutting area of the TSDC tipped SMART*CUT pick was about 511 ^{o}C, which is more than 40% lower than that of the conventional WC tipped picks. The residual temperature of the TSDC tipped SMART*CUT picks after the rock cutting were also lower than that of the WC tipped picks. The average residual temperatures were approximately 104 ^{o}C and 388 ^{o}C for the TSDC tipped SMART*CUT and WC tipped picks, respectively. The sparks produced by the SMART*CUT picks during cutting was much fewer than those produced by the WC tipped pick, strongly suggesting that the TSDC tipped SMART*CUT picks have very good potential to reduce the risk of frictional ignition.

(4) Although the modern infrared photographic technology provides a high capture speed, fast response time and non-intrusive way to determine the temperature distribution in the cutting area, the measurement might not be accurate enough as the flying chips and dust strongly affected the measurement and it was hardly to capture the temperature at the hot spot. Therefore, a special thermocouple configuration was further developed to measure the temperature upon the contact surface. The transient temperature at the hot spot was measured when the rock advanced against the pick. The effects of the cutting parameters including depth of cut, spacing and cutting speed on the pick temperature were obtained. It was found that the pick tip temperature increased significantly with the increased depth of cut and cutting speed. The effect of spacing on the pick tip temperature was smaller than that of the depth of cut and cutting speed, particularly when the spacing was greater than that required to

change from unrelieved to relieved cutting. For all the cutting conditions used, the pick tip temperature varied from 313 ^{o}C to 1100 ^{o}C. The highest temperature was about 1100 ^{o}C with the cutting speed of 2.5 m/s, the DOC of 10 mm and the spacing of 50 mm, at which reddish and black discontinuous banding chips were formed in the cutting groove.

(5) A series of rock cutting tests was also conducted to investigate the effects of cutting parameters on the coarseness index for the TSDC tipped picks. It was found that depth of cut, cutting speed and spacing had relatively great contributions on the coarseness index. Those key parameters were then chosen to examine their effect on the rock chip size distribution and specific energy.

(6) The key conclusions from the analysis of the morphology and the size distribution of the rock chips are summarised below:

- The dust proportion decreased with the increased depth of cut, while the chips distributing on large size increased with the depth of cut. Chips at small depths of cut were almost distributed on small sizes; on the contrary, chips at larger depth of cut distributed more on the larger sizes. Moreover the size of chips also increased significantly with the increase of depth of cut.
- The dust proportion slightly decreased when the spacing increased from 20 mm to 30 mm, then increased slightly with a further increase of spacing. Chips mostly distributed on size large than 8 mm for all the spacing.
- The fraction of fine grains increased gradually with the increased cutting speed. For cutting speed of 0.5 m/s, the proportion of large chips was dominant. It decreased rapidly when the cutting speed increased to 2.5 m/s. However, no major difference was found between the chip sizes at different cutting speeds.

The cutting specific energy under these various cutting conditions was also investigated by using “chip weigh method”. The specific cutting energy increased with the increased cutting speed and spacing, while it decreased and then approached a saturated value with increasing depth of cut.

(7) Three dimensional numerical models were constructed by using an explicit finite element code LS-DYNA to further study the rock cutting process. Using these numerical models, the cutting forces and specific energy under different cutting conditions were

obtained and compared with the results obtained experimentally and analytically. The conclusions drawn from these analysis and comparisons were summarised below:

- The simulated cutting forces agreed well with the measured data in both trend and magnitude, but the simulated cutting forces were slightly smaller than the measured data in general.
- Compared with the experimentally measured and simulated forces, Evan's and Goktan's models overestimated the forces especially when the depth of cut is large. In addition, Evans's model did not take into account for the attack angle and cutting speed and Goktan's model neglected the effect of cutting speed, which was inconsistent with the experimental and numerical force values.
- The regression analyses demonstrated that the numerical simulated cutting forces had a strong correlation with the experimental forces, indicating that the simulation was quite accurate.
- The numerical and experimental specific energies also showed good agreement, further confirming the validation of the numerical model.

8.2 Recommendations for future work

Although a systematic investigation was conducted to understand the rock cutting performance of the TSDC tipped SMART*CUT and WC tipped picks, some research issues apparently require further investigation, in particular for better and more economic use of the new picks, which are summarised below.

(1) To ensure successful application of TSDC tipped SMART*CUT picks for efficient and economical cutting of hard and abrasive rocks, a cutterhead performance prediction model should be developed based on the understanding of the cutting performance and the cutting forces obtained from this study. The model should be able to accurately predict the force, torque, and moment acting on individual picks, as well as their overall values, so cutting specific energy of the machine can be determined. It is expected in this model the effects of rock properties, cutterhead design, and operational conditions of the machine should be taken into account. Field tests need to be carried out to validate and refine the model.

(2) In this study, a special configuration of thermocouple was developed for measuring the tip temperature for the WC tipped pick and accurate transient temperature at the hot spot was successfully measured when the pick was passing through the rock. However, for the SMART*CUT pick with TSDC tip, it is too hard to drill a hole in the tip of the pick. Measurement by use of the infrared photographic technique was insufficiently accurate for further optimisation the cutting process due to the obstruction of flying chips and dust. So a new measurement technique has to be developed for measuring the temperature at the hot spot of the thermal stable diamond composite (TSDC) picks.

(3) Although the "weigh method" can be used to determine the cutting volume and subsequently calculate the specific energy. It is time-consuming to collect all the debris after each cutting test. In the future study, an accurate image system should be developed so the volume of the removed rock could be easily obtained. The development of such an imaging system is also important for studying the morphology of the rock surface and the cross section of the groove.

(4) The numerical simulation of the rock cutting process in this study was based on the unrelieved cutting mode. Whereas in a practical rock cutting process, a certain proportion of picks on the cutting drum are engaged in the rock stratum at the same time. Interaction is created between the adjacent picks. Thus, the numerical models could be extended to include the relieved cutting mode, so the modelling accuracy could be further improved. The multi-mode numerical model might be further expanded for rotary cutting.

Reference

[1] M. Cigla and L. Ozdemir, "Computer modeling for improved production of mechanical excavators," in Society for Mining, Metallurgy and Exploration (SME) annual metting, Salt Lake City, Preprint No. 00-65, pp. 1-12, 2000.

[2] M. Hood and H. Alehossein, "A development in rock cutting technology," International Journal of Rock Mechanics and Mining Sciences, vol. 37, pp. 297-305, 2000.

[3] H. Copur, et al., "A set of indices based on indentation tests for assessment of rock cutting performance and rock properties," Journal of South African Institute of Mining and Metallurgy, vol. 103(9), pp. 589-599, 2003.

[4] N. Bilgin, et al., "Dominant rock properties affecting the performance of conical picks and the comparison of some experimental and theoretical results," International Journal of Rock Mechanics and Mining Sciences, vol. 43, pp. 139-156, 2006.

[5] R.H. Bao, et al., "Estimating the Peak Indentation Force of the Edge Chipping of Rocks Using Single Point-Attack Pick," Rock Mechanics and Rock Engineering, vol. 44, pp. 339-347, 2011.

[6] K. Hurt and I. Evans, "Point attack tools: an evaluation of function and use for rock cutting," Mining Engineer, vol. 140, pp. 673-679, 1981.

[7] N.G. Yilmaz, et al., "Prediction of radial bit cutting force in high-strength rocks using multiple linear regression analysis," International Journal of Rock Mechanics and Mining Sciences, vol. 44, pp. 962-970, 2007.

[8] J.A. Martin and R.J. Fowell, "Factors governing the onset of severe drag tool wear in rock cutting," International Journal of Rock Mechanics and Mining Sciences & Geomechanics Abstracts, vol. 34, pp. 59-69, 1997.

[9] Wirtgen Group (2010), Wirtgen Surface Mining Manual: Applications and Planning Guide.

[10] R.J. Fowell, et al., "Drag tools employed on shearer drums and roadheaders," in Proceedings of the 10th Turkish Mining Congress, Ankara, pp. 529-550, 1987.

[11] P.J.A Borm, "Toxicity and occupational health hazards of coal fly ash (CFA). A review of data and comparison to coal mine dust," Annals of Occupational Hygiene, vol. 41, pp. 659-676, 1997.

[12] H. Alehossein, et al., "Towards Improving Rock Cutting Tools Using Thermally Stable Diamond Composites," Advanced Materials Research, vol. 76-78, pp. 585-590, 2009.

[13] X.S. Li, et al., "Hard Rock Cutting With Smart* Cut Technology," in Proceedings of the 22nd World Mining Congress and Expo, Istanbul, Turkey, pp. 726-732, 2011.

[14] X.S. Li, "Development of Hard Rock Cutting Tool with Advanced Diamond Composites," Advanced Materials Research, vol. 690-693, pp. 1831-1835, 2013.

[15] J. N. Boland, et al., "Diamond composite rock cutting tools," in the European Conference on Hard Materials and Diamond Tooling, Lausanne, Switzerland, pp. 103-108, 2002.

[16] X.S. Li and J.N. Boland, "The wear characteristics of superhard composite materials in abrasive cutting operations," Wear, vol. 259, pp. 1128-1136, 2005.

[17] J.N. Boland and X.S. Li, "Microstructural characterisation and wear behaviour of diamond composite materials," Materials, vol. 3, pp. 1390-1419, 2010.

[18] P. Graham, "Rock exploration for machine manufacturers," Exploration for Rock Engineering, pp. 173-80, 1976.

[19] C. Balci and N. Bilgin, "Correlative study of linear small and full-scale rock cutting tests to select mechanized excavation machines," International Journal of Rock Mechanics and Mining Sciences, vol. 44, pp. 468-476, 2007.

[20] Q. YAO, "An investigation of rock cutting: towards a novel design of cutting bits," Ph.D. Thesis, The University of New South Wales, 2012.

[21] R.J. Fowell and N. Ochei, "A comparison of dust make and energy requirements for rock cutting tools," Geotechnical and Geological Engineering, vol. 2, pp. 73-83, 1984.

[22] K. Hurt and K. MacAndrew, "Cutting efficiency and life of rock-cutting picks," Mining Science and Technology, vol. 2, pp. 139-151, 1985.

[23] A.W. Khair, "The effect of bit geometry on rock cutting efficiency," Applied Occupational and Environmental Hygiene, vol. 11, pp. 695-700, 1996.

[24] A. Wahab Khair, et al., "Mechanisms of coal fragmentation by a continuous miner," Mining Science and Technology, vol. 8, pp. 189-214, 1989.

[25] R.A. Qayyum, "Effects of bit geometry in multiple bit-rock interaction," Ph.D. Thesis, West Virginia University, 2003.

[26] S. Addala, "Relationship between cutting parameters and bit geometry in rotary cutting," Ph.D. Thesis, West Virginia University, 2000.

[27] F.F. Roxborough, "A review of research progress in coal and rock cutting," Coal J (No. 13), pp. 37-48, 1986.

[28] B. Tiryaki, et al., "Laboratory Comparison of Mini-discs with Point-attack Picks," Advanced Materials Research, vol. 126, pp. 189-194, 2010.

[29] B.R. Fish and J.S. Barker, "Study in rotary drilling," National Coal Board MRE Report No. 209, 1956.

[30] C. Fairhurst, "Some principles and development in Hard Rock drilling techniques," in Proceedings of 6th Annual Drilling and Blassing Symposium, Univeristy of Minnesota, pp. 15-27, 1956.

[31] R. Goodrich, "High pressure rotary drilling machines," in Proceedings of the 2nd Annual Symposium on Mining Research, University of Missouri, pp. 212-221, 1956.

[32] C. Fairhurst, "Hard rock drilling techniques," Mine and Quarry Engineer, vol. 23, pp. 157-161, 1957.

[33] H.L. Hartman, "Basic studies of percussion drilling," Mining Engineering, vol. 11, pp. 68-75, 1959.

[34] Y. Nishimatsu, "The mechanics of rock cutting," International Journal of Rock Mechanics and Mining Sciences & Geomechanics Abstracts, vol. 9, pp. 261-270, 1972.

[35] M. Friedman and L.M. Ford, "Analysis of rock deformation and fractures induced by rock cutting tools used in coal mining," in Proceedings of the 24th U.S. Symposium on Rock Mechanics, Texas, pp. 713-723, 1983.

[36] C.K. Ip, et al., "Water Jet Rock Cutting and Its Application to Tunnel Machine Performance," in Proceedings of the 27th U.S. Symposium on Rock Mechanics, Alabama, pp. 883-890, 1986.

[37] H.I. Inyang, "Drag bit cutting: A conception of rock deformation processes that correspond to observed force-distance plots," in Proceedings of the 2nd International Symposium on Mine Planning and Equipment Selection, Calgary, pp. 373-378, 1990.

[38] F.F. Roxborough and H. Phillips, "Applied rock and coal cutting mechanics," Workshop Course, Australian Mineral Foundation Inc, pp.11-15, 1981.

[39] R. Goktan and N. Gunes, "A semi-empirical approach to cutting force prediction for point-attack picks," Journal of South African Institute of Mining and Metallurgy, vol. 105, pp. 257-263, 2005.

[40] H. Çopur, et al., "Specific energy as a criterion for the use of rapid excavation systems in Turkish mines," Mining Technology, vol. 110, pp. 149-157, 2001.

[41] C. Balci, et al., "Estimation of optimum specific energy based on rock properties for assessment of roadheader performance," Journal of The South African Institute of Mining and Metallurgy, vol. 104, pp. 633-641, 2004.

[42] O. Su and N. Ali Akcin, "Numerical simulation of rock cutting using the discrete element method," International Journal of Rock Mechanics and Mining Sciences, vol. 48, pp. 434-442, 2011.

[43] J. Rostami, et al., "Performance prediction: a key issue in mechanical hard rock mining," Mining Engineering, vol. 46, pp. 1263-1267, 1994.

[44] M.E. Merchant, "Basic mechanics of the metal-cutting process," Journal of Applied Mechanics, vol. 11, pp. 168-175, 1944.

[45] M.E. Merchant, "Mechanics of the metal cutting process. I. Orthogonal cutting and a type 2 chip," Journal of Applied Physics, vol. 16, pp. 267-275, 1945.

[46] M.E. Merchant, "Mechanics of the metal cutting process. II. Plasticity conditions in orthogonal cutting," Journal of Applied Physics, vol. 16, pp. 318-324, 1945.

[47] E. Potts and P. Shuttleworth, "A study of ploughability of coal, with special reference to the effects of blade shape, direction of planning to the cleat, planning speed and the influence of water infusion," Transactions of the Institution of Mining Engineers, vol. 117, pp. 520-548, 1958.

[48] F.F. Roxborough and A. Rispin, "Mechanical cutting characteristics of lower Chalk," Tunnels & Tunnelling International, vol. 5, pp. 45-67, 1973.

[49] I. Evans, "A theory of the basic mechanics of coal ploughing," in Proceedings of the International Symposium on Mining Research, University of Missouri, London, pp. 761-798, 1962.

[50] I. Evans, "The force required to cut coal with blunt wedges," International Journal of Rock Mechanics and Mining Sciences & Geomechanics Abstracts, vol. 2, pp. 1-12, 1965.

[51] F.F. Roxborough, "Cutting rock with picks," The Mining Engineer, vol. 132, pp. 445-455, 1973.

[52] I. Evans, "A theory of the cutting force for point-attack picks," International Journal of Mining Engineering, vol. 2, pp. 63-71, 1984.

[53] H.I. Inyang, "Developments in drag bit cutting of rocks for energy infrastructure," International Journal of Surface Mining, Reclamation and Environment, vol. 16, pp. 248-260, 2002.

[54] F.F. Roxborough and Z. Liu, "Theoretical considerations on pick shape in rock and coal cutting," in Proceedings of the 6th Underground Operator's Conference, Kalgoorlie, pp. 189–193, 1995.

[55] R. Goktan, "A suggested improvement on Evans' cutting theory for conical bits," in Proceedings of the 4th International Symposium on Mine Mechanication and Automation, pp. 57-61, 1997.

[56] R. Goktan, "Prediction of drag bit cutting force in hard rocks," in Proceedings of the 3rd International Symposium on Mine Mechanization and Automation, Golden, Colorado, pp. 10-31, 1995.

[57] K.G. Hurt, "Laboratory study of rock cutting using point attack tools," U.S. Symposium on Rock Mechanics, pp. 112-122, 1980.

[58] E. Almond and N. McCormick, "Constant-geometry edge-flaking of brittle materials," Nature 321(6065):53-55, 1986.

[59] J. Quinn, et al., "“Edge toughness” and material properties related to the machining of dental ceramics," Machining Science and Technology, vol. 4, pp. 291-304, 2000.

[60] H. Chai and B.R. Lawn, "Edge chipping of brittle materials: effect of side-wall inclination and loading angle," International Journal of Fracture, vol. 145, pp. 159-165, 2007.

[61] G. Gogotsi, et al., "Evaluation of fracture resistance of ceramics: Edge fracture tests," Ceramics International, vol. 33, pp. 315-320, 2007.

[62] Q.Y. Yao, et al., "Edge Chipping of Rock: An Experimental Study," Key Engineering Materials, vol. 443, pp. 456-461, 2010.

[63] K.E. Rånman, "A model describing rock cutting with conical picks," Rock Mechanics and Rock Engineering, vol. 18, pp. 131-140, 1985.

[64] G.P. Cherepanov, "Mechanics of brittle fracture," Chapter 9, McGraw-Hill, New York, 1979.

[65] G. Cherepanov, "Theory of rock cutting," Strength of Materials, vol. 18, pp. 1103-1114, 1986.

[66] H. Guo, et al., "Rock cutting study using linear elastic fracture mechanics," Engineering Fracture Mechanics, vol. 41, pp. 771-778, 1992.

[67] G.W. Ellis, et al., "Neural network modeling of the mechanical behavior of sand," in Proceedings of 9th Conference of American Society of Civil Engineers, pp. 421-424, 1992.

[68] H. Alehossein and M. Hood, "An application of linearised dimensional analysis to rock cutting," International Journal of Rock Mechanics and Mining Sciences, vol. 36, pp. 701-709, 1999.

[69] M. Alvarez Grima and R. Babuška, "Fuzzy model for the prediction of unconfined compressive strength of rock samples," International Journal of Rock Mechanics and Mining Sciences, vol. 36, pp. 339-349, 1999.

[70] M. Alvarez Grima, et al., "Modeling tunnel boring machine performance by neuro-fuzzy methods," Tunnelling and Underground Space Technology, vol. 15, pp. 259-269, 2000.

[71] J. Finol, et al., "A rule based fuzzy model for the prediction of petrophysical rock parameters," Journal of Petroleum Science and Engineering, vol. 29, pp. 97-113, 2001.

[72] V. Singh, et al., "Prediction of strength properties of some schistose rocks from petrographic properties using artificial neural networks," International Journal of Rock Mechanics and Mining Sciences, vol. 38, pp. 269-284, 2001.

[73] C. Gokceoglu, "A fuzzy triangular chart to predict the uniaxial compressive strength of the Ankara agglomerates from their petrographic composition," Engineering Geology, vol. 66, pp. 39-51, 2002.

[74] A. Benardos and D. Kaliampakos, "Modelling TBM performance with artificial neural networks," Tunnelling and Underground Space Technology, vol. 19, pp. 597-605, 2004.

[75] H. Sonmez, et al., "Models to predict the uniaxial compressive strength and the modulus of elasticity for Ankara Agglomerate," International Journal of Rock Mechanics and Mining Sciences, vol. 41, pp. 717-729, 2004.

[76] S. Kahraman, et al., "Sawability prediction of carbonate rocks from shear strength parameters using artificial neural networks," International Journal of Rock Mechanics and Mining Sciences, vol. 43, pp. 157-164, 2006.

[77] B. Tiryaki, "Predicting intact rock strength for mechanical excavation using multivariate statistics, artificial neural networks, and regression trees," Engineering Geology, vol. 99, pp. 51-60, 2008.

[78] B. Tiryaki, "Application of artificial neural networks for predicting the cuttability of rocks by drag tools," Tunnelling and Underground Space Technology, vol. 23, pp. 273-280, 2008.

[79] B. Tiryaki, et al., "Empirical models to predict mean cutting forces on point-attack pick cutters," International Journal of Rock Mechanics and Mining Sciences, vol. 47, pp. 858-864, 2010.

[80] H.M. Hughes, "Some aspects of rock machining," International Journal of Rock Mechanics and Mining Sciences & Geomechanics Abstracts, vol. 9, pp. 205-211, 1972.

[81] M. Mellor, "Normalization of specific energy values," International Journal of Rock Mechanics and Mining Sciences & Geomechanics Abstracts, vol. 9, pp. 661-663, 1972.

[82] R. Fowell and I. McFeat-Smith, "Factors influencing the cutting performance of a selective tunnelling machine," in Proceedings of Tunnelling Symposium, pp. 301-309, 1976.

[83] I. McFeat-Smith and R. Fowell, "Correlation of rock properties and the cutting performance of tunnelling machines," in Proceedings of the Conference on Rock Engineering, pp. 581-602, 1977.

[84] R.M. Göktan, "Brittleness and micro-scale rock cutting efficiency," Mining Science and Technology, vol. 13, pp. 237-241, 1991.

[85] H. Copur, et al., "Specific energy as a criterion for the use of rapid excavation systems in Turkish mines," Mining Technology, vol. 110, pp. 149-157, 2001.

[86] B. Asbury, et al., "Design methodology, testing and evaluation of a continuous miner cutterhead for dust reduction in underground coal mining," in SME Annual Meeting, Phoenix, Arizona, pp. 1-8, 2002.

[87] F.F. Roxborough and A. Rispin, "A laboratory investigation into the application of picks for mechanized tunnel boring in the lower chalk," The Mining Engineer, vol. 133, pp. 1-13, 1973.

[88] F.F. Roxborough, "Rock excavation by disc cutter," International Journal of Rock Mechanics and Mining Sciences & Geomechanics Abstracts, vol. 12, p. 361, 1975.

[89] F.F. Roxborough, "Research in mechanical rock excavation: progress and prospects," in Proceedings of the Rapid Excavation Tunn Congress, Las Vegas, pp. 225-244, 1985.

[90] D.A. Glowka, "The thermal response of rock to friction in the drag cutting process," Journal of Structural Geology, vol. 11, pp. 919-931, 1989.

[91] J. Marshall, "Quantifying the Potential for a Frictional Ignition," in Queensland Mining Industry Health & Safety Conference, pp. 459-461, 2000.

[92] C.R. Ward, et al., "Identification of potential for methane ignition by rock friction in Australian coal mines," International Journal of Coal Geology, vol. 45, pp. 91-103, 2001.

[93] K. Hurt and I. Evans, "Point attack tools: an evaluation of function and use for rock cutting," Mining Engineer, vol. 140, pp.673-679, 1981.

[94] K.E. Gray, et al., "Two-dimensional study of rock breakage in drag-bit drilling at atmospheric pressure," Journal of Petroleum Technology, vol. 14, pp. 93-98, 1962.

[95] M.F. DeVries, "Investigation of drill temperature as a drilling performance criterion," Ph.D. Thesis, University of Wisconsin, USA, 1966.

[96] A. Barbish and G. Gardner, "The effect of heat on some mechanical properties of igneous rocks," Society of Petroleum Engineers Journal, vol. 9, pp. 395-402, 1969.

[97] J.C. Estes, "Techniques of Pilot-Scale Drilling Research," Journal of Pressure Vessel Technology, vol. 100, pp. 188-193, 1978.

[98] E. Detournay and P. Defourny, "A phenomenological model for the drilling action of drag bits," International Journal of Rock Mechanics and Mining Sciences & Geomechanics Abstracts, vol. 29, pp. 13-23, 1992.

[99] P.M.C.B.M. Cools, "Temperature measurements upon the chisel surface during rock cutting," International Journal of Rock Mechanics and Mining Sciences & Geomechanics Abstracts, vol. 30, pp. 25-35, 1993.

[100] P. Loui and K. Rao, "Experimental investigations of pick-rock interface temperature in drag-pick cutting," Indian Journal of Engineering & Materials Sciences, vol. 4, pp. 63-66, 1997.

[101] I. Korkut, et al., "Investigation of chip-back temperature during machining depending on cutting parameters," Materials & Design, vol. 28, pp. 2329-2335, 2007.

[102] K.-M. Li, et al., "An improved remote sensing technique for estimating tool–chip interface temperatures in turning," Journal of Materials Processing Technology, vol. 213, pp. 1772-1781, 2013.

[103] A. Batako, et al., "Temperature measurement in high efficiency deep grinding," International Journal of Machine Tools and Manufacture, vol. 45, pp. 1231-1245, 2005.

[104] J. Chen, et al., "An experimental study on the grinding of alumina with a monolayer brazed diamond wheel," The International Journal of Advanced Manufacturing Technology, vol. 41, pp. 16-23, 2009.

[105] T. Yashiro, et al., "Temperature measurement of cutting tool and machined surface layer in milling of CFRP," International Journal of Machine Tools and Manufacture, vol. 70, pp. 63-69, 2013.

[106] R.P. Zeilmann and W. L. Weingaertner, "Analysis of temperature during drilling of Ti6Al4V with minimal quantity of lubricant," Journal of Materials Processing Technology, vol. 179, pp. 124-127, 2006.

[107] F. Schmidt, et al., "Modelling of infrared heating of thermoplastic sheet used in thermoforming process," Journal of Materials Processing Technology, vol. 143, pp. 225-231, 2003.

[108] R.-S. Huang, et al., "Infrared temperature measurement and interference analysis of magnesium alloys in hybrid laser-TIG welding process," Materials Science and Engineering: A, vol. 447, pp. 239-243, 2007.

[109] G. Sutter and N. Ranc, "Temperature fields in a chip during high-speed orthogonal cutting—an experimental investigation," International Journal of Machine Tools and Manufacture, vol. 47, pp. 1507-1517, 2007.

[110] M. Doubenskaia, et al., "Definition of brightness temperature and restoration of true temperature in laser cladding using infrared camera," Surface and Coatings Technology, vol. 220, pp. 244-247, 2013.

[111] P. Dearnley, "New technique for determining temperature distribution in cemented carbide cutting tools," Metals Technology, vol. 10, pp. 205-214, 1983.

[112] H. Choi and X. Li, "Fabrication and application of micro thin film thermocouples for transient temperature measurement in nanosecond pulsed laser micromachining of nickel," Sensors and Actuators A: Physical, vol. 136, pp. 118-124, 2007.

[113] F.C. Appl, et al., "Measurement of forces, temperatures and wear of PDC cutters in rock cutting," Wear, vol. 169, pp. 9-24, 1993.

[114] D. Che, et al., "Issues in Polycrystalline Diamond Compact Cutter–Rock Interaction From a Metal Machining Point of View—Part I: Temperature, Stresses, and Forces," Journal of Manufacturing Science and Engineering, vol. 134, p. 064001, 2012.

[115] N. Abukhshim, et al., "Heat generation and temperature prediction in metal cutting: A review and implications for high speed machining," International Journal of Machine Tools and Manufacture, vol. 46, pp. 782-800, 2006.

[116] M. Vaz Jr, et al., "Modelling and simulation of machining processes," Archives of Computational Methods in Engineering, vol. 14, pp. 173-204, 2007.

[117] S. Crouch, "Solution of plane elasticity problems by the displacement discontinuity method. I. Infinite body solution," International Journal for Numerical Methods in Engineering, vol. 10, pp. 301-343, 1976.

[118] H. Guo, "Rock cutting studies using fracture mechanics principles," Ph.D. Thesis, University of Wollongong, 1990.

[119] C. Shih, et al., "Crack extension modeling with singular quadratic isoparametric elements," International Journal of Fracture, vol. 12, pp. 647-651, 1976.

[120] F. Erdogan and G. Sih, "On the crack extension in plates under plane loading and transverse shear," Journal of Fluids Engineering, vol. 85, pp. 519-525, 1963.

[121] X.C. Tan, et al., "Application of the DDM and fracture mechanics model on the simulation of rock breakage by mechanical tools," Engineering Geology, vol. 49, pp. 277-284, 1998.

[122] H. Huang, et al., "Normal Wedge Indentation in Rocks with Lateral Confinement," Rock Mechanics and Rock Engineering, vol. 31, pp. 81-94, 1998.

[123] Z. Fang and J.P. Harrison, "Development of a local degradation approach to the modelling of brittle fracture in heterogeneous rocks," International Journal of Rock Mechanics and Mining Sciences, vol. 39, pp. 443-457, 2002.

[124] I. Bilgesu, et al., "Modeling rock and drill cutter behavior," in Proceedings of the 42nd US Rock Mechanics Symposium (USRMS), San Francisco, California, Paper 08-342, 2008.

[125] I. Tulu, et al., "Modeling rock and drill cutter behavior," in Proceedings of the 42nd US Rock Mechanics Symposium (USRMS), San Francisco, California, Paper 08-342, 2008.

[126] O. Sunal, "Parametric study of a single PDC cutter with a numerical model," Master Thesis, West Virgenia University, 2009.

[127] I. Tulu and K. Heasley, "Calibration of 3D cutter-rock model with single cutter tests," in Proceedings of the 43rd US Rock Mechanics Symposium, Asheville, North Carolina, Paper 09-160, 2009.

[128] I.B. Tulu, "Modeling PDC cutter rock interaction" Master Thesis, West Virgenia University, 2009.

[129] H. Huang, et al., "Discrete element modelling of rock cutting," Rock Mechanics for Industry, vol. 1-2, pp. 123-130, 1999.

[130] G. Block and H. Jin, "Role of failure mode on rock cutting dynamics," in SPE Annual Technical Conference and Exhibition, New Orieans, Louisiana, pp. 1-9, 2009.

[131] J. Rojek, et al., "Discrete element simulation of rock cutting," International Journal of Rock Mechanics and Mining Sciences, vol. 48, pp. 996-1010, 2011.

[132] C. Tang, "Numerical simulation of progressive rock failure and associated seismicity," International Journal of Rock Mechanics and Mining Sciences, vol. 34, pp. 249-261, 1997.

[133] S. Kou, et al., "Numerical simulation of the cutting of inhomogeneous rocks," International Journal of Rock Mechanics and Mining Sciences, vol. 36, pp. 711-717, 1999.

[134] H. Liu, "Numerical simulation of the rock fragmentation process induced by indenters," International Journal of Rock Mechanics and Mining Sciences, vol. 39, pp. 491-505, 2002.

[135] H. Liu, "Numerical modeling of the rock fragmentation process by mechanical tools," Ph.D. Thesis, Luleå University of Technology, Luleå, Sweden, 2004.

[136] W. Zhu and C. Tang, "Micromechanical model for simulating the fracture process of rock," Rock Mechanics and Rock Engineering, vol. 37, pp. 25-56, 2004.

[137] H. Liu, et al., "Numerical studies on Bit-Rock fragmentation mechanisms," International Journal of Geomechanics, vol. 8, pp. 45-67, 2008.

[138] S. Wang, et al., "Numerical simulation of the rock fragmentation process induced by two drill bits subjected to static and dynamic (impact) loading," Rock Mechanics and Rock Engineering, vol. 44, pp. 317-332, 2011.

[139] B. Yu, "Numerical simulation of continuous miner rock cutting process," Ph.D. Thesis, West Virginia University, 2005.

[140] M. Jaime, et al., "Finite element modeling of rock cutting," in Proceedings of the 44th US Rock Mechanics Symposium and 5th US-Canada Rock Mechanics Symposium, American Rock Mechanics Association, Salt Lake City, UT, Paper 10-231, 2010.

[141] S.A.B.Da Fontoura, et al., "Rock Mechanics Aspects of Drill Bit Rock Interaction," in Proceedings of the 12th ISRM Congress, Bejing, China, pp. 2041-2046, 2011.

[142] W. Shao, et al., "Linear Rock Cutting with SMART* CUT Picks," Applied Mechanics and Materials, vol. 477, pp. 1378-1384, 2014.

[143] W. Shao, et al., "Laboratory Comparison of SMART* CUT Picks With WC Picks," Advanced Materials Research, vol. 1017, pp. 323-328, 2014.

[144] J.N. Boland, "Characterisation of diamond composites for tooling," Materials Forum, vol. 34, pp. 17-28, 2008.

[145] H.-L. Lin and C.-P. Chou, "Modeling and optimization of Nd: YAG laser micro-weld process using Taguchi Method and a neural network," The International Journal of Advanced Manufacturing Technology, vol. 37, pp. 513-522, 2008.

[146] S. Datta, et al., "Application of PCA-based hybrid Taguchi method for correlated multicriteria optimization of submerged arc weld: a case study," The International Journal of Advanced Manufacturing Technology, vol. 45, pp. 276-286, 2009.

[147] G. Taguchi, et al., Taguchi's quality engineering handbook. Hoboken, N.J; Livonia, Mich: John Wiley, 2005.

[148] S. Datta, et al., "Grey-based taguchi method for optimization of bead geometry in submerged arc bead-on-plate welding," The International Journal of Advanced Manufacturing Technology, vol. 39, pp. 1136-1143, 2008.

[149] F.F Roxborough, et al., "Tests on the cutting performance of continuous miner," Journal of South African Institute of Mining and Metallurgy, vol. 81, pp. 9-26, 1981.

[150] A. Giacomino, et al., "The role of chemometrics in single and sequential extraction assays: a review. Part II. Cluster analysis, multiple linear regression, mixture resolution, experimental design and other techniques," Analytica Chimica Acta, vol. 688, pp. 122-139, 2011.

[151] E. Avunduk, et al., "Prediction of roadheader performance by artificial neural network," Tunnelling and Underground Space Technology, vol. 44, pp. 3-9, 2014.

[152] R. Trueman, "A literature review of the ignition of methane-air mixtures by coal-cutting picks," Journal of South African Institute of Mining and Metallurgy, vol. 85, pp. 209-215, 1985.

[153] B.D. Hanson, "Cutting Parameters Affecting the Ignition Potential of Conical Bits,", US Department of the Interior, Bureau of Mines, Report of Investigation 8820, 1983.

[154] D.A. Larson, "Preliminary Evaluation of Bit Impact Ignitions of Methane Using a Drum-type Cutting Head," US Department of the Interior, Bureau of Mines, Report of Investigation 8755, 1983.

[155] A. Ortega and D. A. Glowka, "Frictional heating and convective cooling of polycrystalline diamond drag tools during rock cutting," Society of Petroleum Engineers, vol. 24(2), pp. 121-128, 1982.

[156] J.P. Loui and U. Karanam, "Heat transfer simulation in drag–pick cutting of rocks," Tunnelling and Underground Space Technology, vol. 20, pp. 263-270, 2005.

[157] G. Sutter, et al., "An experimental technique for the measurement of temperature fields for the orthogonal cutting in high speed machining," International Journal of Machine Tools and Manufacture, vol. 43, pp. 671-678, 2003.

[158] C. Leshock and Y. Shin, "Investigation on cutting temperature in turning by a tool-work thermocouple technique," Journal of Manufacturing Science and Engineering, vol. 119, pp. 502-508, 1997.

[159] W. Grzesik, "The role of coatings in controlling the cutting process when turning with coated indexable inserts," Journal of Materials Processing Technology, vol. 79, pp. 133-143, 1998.

[160] W. Grzesik, "The influence of thin hard coatings on frictional behaviour in the orthogonal cutting process," Tribology International, vol. 33, pp. 131-140, 2000.

[161] W. Grzesik, "An integrated approach to evaluating the tribo-contact for coated cutting inserts," Wear, vol. 240, pp. 9-18, 2000.

[162] W. Grzesik and P. Nieslony, "A computational approach to evaluate temperature and heat partition in machining with multilayer coated tools," International Journal of Machine Tools and Manufacture, vol. 43, pp. 1311-1317, 2003.

[163] E. Brinksmeier, et al., "Drilling of composites and resulting surface integrity," CIRP Annals - Manufacturing Technology, vol. 60, pp. 57-60, 2011.

[164] W.B. Rowe, et al., "Experimental Investigation of Heat Transfer in Grinding," CIRP Annals - Manufacturing Technology, vol. 44, pp. 329-332, 1995.

[165] J. Lin, et al., "Estimation of cutting temperature in high speed machining," Journal of Engineering Materials and Technology, vol. 114, pp. 289-296, 1992.

[166] T. Ueda, et al., "Temperature Measurement of CBN Tool in Turning of High Hardness Steel," CIRP Annals - Manufacturing Technology, vol. 48, pp. 63-66, 1999.

[167] G. Boothroyd, "Photographic technique for the determination of metal cutting temperatures," British Journal of Applied Physics, vol. 12, p. 238, 1961.

[168] S. Jeelani, "Measurement of temperature distribution in machining using IR photography," Wear, vol. 68, pp. 191-202, 1981.

[169] V. Narayanan, et al., "Measurement of the temperature field at the tool-chip interface in machining," in Proceedings of 2001 ASME International Mechanical Engineering Congress and Exposition. New York, pp. 1-8, 2001.

[170] D. O'sullivan and M. Cotterell, "Temperature measurement in single point turning," Journal of Materials Processing Technology, vol. 118, pp. 301-308, 2001.

[171] M. Davies, et al., "On the measurement of temperature in material removal processes," CIRP Annals-Manufacturing Technology, vol. 56, pp. 581-604, 2007.

[172] R.R. Rashid, et al., "An investigation of cutting forces and cutting temperatures during laser-assisted machining of the Ti–6Cr–5Mo–5V–4Al beta titanium alloy," International Journal of Machine Tools and Manufacture, vol. 63, pp. 58-69, 2012.

[173] L. Li, et al., "A thermo-mechanical model of dry orthogonal cutting and its experimental validation through embedded micro-scale thin film thermocouple arrays in PCBN tooling," International Journal of Machine Tools and Manufacture, vol. 70, pp. 70-87, 2013.

[174] K. Okushima and R. Shimoda, "The cutting temperature," Bull. JSME, vol. 23, pp. 73-77, 1957.

[175] T. Kato and H. Fujii, "PVD film method for measuring the temperature distribution in cutting tools," Journal of Manufacturing Science and Engineering, vol. 118, pp. 117-122, 1996.

[176] P. Wright and E. Trent, "Metallographic methods of determining temperature gradients in cutting tools," Journal of Iron and Steel Insititute, vol. 211, pp. 364-368, 1973.

[177] H. Tuncdemir, et al., "Control of rock cutting efficiency by muck size," International Journal of Rock Mechanics and Mining Sciences, vol. 45, pp. 278-288, 2008.

[178] M.Z.A. Bakar and L. S. Gertsch, "Evaluation of saturation effects on drag pick cutting of a brittle sandstone from full scale linear cutting tests," Tunnelling and Underground Space Technology, vol. 34, pp. 124-134, 2013.

[179] A. Bruland, "Hard rock performance data and back-mapping," Norwegian Institute of Technology, Department of Building and Construction Engineering, Trondheim, Norway, 2000.

[180] F.F. Roxborough, "Cutting rock with picks," The Mining Engineer, vol. 133, pp. 445-454, 1973.

[181] X. Liu, et al., "Coal fragment size model in cutting process," Powder Technology, vol. 272, pp. 282-289, 2015.

[182] J. Rostami, et al., "Performance prediction: a key issue in mechanical hard rock mining," Mining Engineering, vol. 11, pp. 1263-1267, 1994.

[183] J.-W. Cho, et al., "Evaluation of cutting efficiency during TBM disc cutter excavation within a Korean granitic rock using linear-cutting-machine testing and photogrammetric measurement," Tunnelling and Underground Space Technology, vol. 35, pp. 37-54, 2013.

[184] M.C. Jaime, et al., "Finite element modeling of rock cutting and its fragmentation process," International Journal of Rock Mechanics and Mining Sciences, vol. 80, pp. 137-146, 2015.

[185] E. Papamichos, "Constitutive laws for geomaterials," Oil & Gas Science and Technology, vol. 54, pp. 759-771, 1999.

[186] M. Tao, et al., "Characteristics of the unloading process of rocks under high initial stress," Computers and Geotechnics, vol. 45, pp. 83-92, 2012.

[187] L.E. Schwer and Y. D. Murray, "Continuous surface cap model for geomaterial modeling: a new LS-DYNA material type," in International LS-dyna Users Conference, Detroit p (16), pp. 35-50, 2002.

[188] Y.D. Murray, "Theory and evaluation of concrete material model 159," in 8th International LS-DYNA users conference, Dearborn, Michigan, pp. 25-36, 2004.

[189] Y.D. Murray, "Users manual for LS-DYNA concrete material model 159," U.S. Department of Transportation, Federal Highway Administration, McLean, VA, Report No FHWA-HRT-05-062, 2007.

[190] J.O. Hallquist, "LS-DYNA theory manual," Livermore Software Technology Corporation, vol. 3, 2006.